Delft University of Technology
Faculty of Chemical Technology and Materials Science
Section Thermal Processing Technology
Rotterdamseweg 137, 2628 AL Delft, The Netherlands.

Strength Optimisation of Au-Pt-base alloys

A.W.M. van den Hondel

Delft, April 1994.

Supervision:
prof.dr.ir. S. van der Zwaag
dr.ir. P. van Mourik

Final report of the graduation project which forms a part of the requirements to obtain a Master's degree in Materials Science.

Contents

Summary

The spinning of aramide fibres from a sulphuric-acid-solution proceeds via a spinneret. The spinneret is made of AuPtRh alloys, sometimes with a Pd-addition, that obtain their final strength during a heat treatment after the forming process. In this study the following alloy compositions were investigated:

1. AuPtRh 69/30/1 at. % (69.5/30/0.5 wt. %);
2. AuPtRh 59/40/1 at. % (59.5/40/0.5 wt. %);
3. AuPtPdRh 54/27.5/17/1.5 at. % (59/30/10/1 wt. %); and
4. AuPtPdRh 44.5/37/17/1.5 at. % (49/40/10/1 wt. %).

Applying a theory that relates the composition and microstructure to the mechanical properties, the yield strengths of these alloys were predicted for several conditions after heat treatment. In order to do this, it is necessary to have some insight in the microstructure as a function of the heat treatment, and therefore the constitutions of the alloys were investigated. The results were obtained using light microscopy, hardness measurements, differential thermal analysis, and tensile tests.

At usual temperatures, the alloys studied are in a dual-phase condition: the Au-rich (matrix) phase and the Pt-rich (second) phase. The AuPtRh alloys remain up to the start of melting (at about 1300°C) in a dual-phase condition. The AuPtPdRh alloys are at sufficiently high temperatures (1350-1400°C) monophase. Rh enhances the stability of the Pt-rich phase, whereas Pd reduces this stability.

Decomposition during the heat treatments applied are of paramount importance for the mechanical properties: after complete homogenisation part of the decomposition products appear as discontinuous precipitates at the grain boundaries, resulting in a drastic decrease of the strain at fracture, while the ultimate tensile stress in this condition was the highest. The optimum combination of high yield strength and high strain at fracture was found in the "decomposed" dual-phase condition. Application of the previously indicated theory gave a fairly good prediction of the measured yield strengths.

Samenvatting

Het spinnen van aramide-vezels uit zwavelzuur verloopt via een spindop. Deze spindop wordt vervaardigd uit AuPtRh legeringen, eventueel met een Pd-toevoeging, die hun sterkte na vorming van de dop krijgen door warmtebehandeling. In dit onderzoek zijn vier legeringssamenstellingen onderzocht:

1. AuPtRh 69/30/1 at. % (69.5/30/0.5 wt. %);
2. AuPtRh 59/40/1 at. % (59.5/40/0.5 wt. %);
3. AuPtPdRh 54/27.5/17/1.5 at. % (59/30/10/1 wt. %); en
4. AuPtPdRh 44.5/37/17/1.5 at. % (49/40/10/1 wt. %).

Met een theorie die een verband legt tussen samenstelling, microstructuur en mechanische eigenschappen worden deze laatste voorspeld voor de onderzochte legeringen in verschillende toestanden na warmtebehandeling. Hiervoor is inzicht nodig in de microstructuur als functie van die warmtebehandeling en daarom is ook gekeken naar de constitutie van de betreffende legeringen. De onderzoeksresultaten zijn verkregen met lichtmicroscopie, hardheidsmetingen, differentiële thermische analyse en trekproeven.

De onderzochte legeringen bestaan bij gangbare temperaturen uit twee fasen: de Au-rijke (matrix) fase en de Pt-rijke (secundaire) fase. De AuPtRh-legeringen blijven tot temperaturen van smelten (circa 1300°C) uit twee fasen bestaan. De AuPtPdRh-legeringen bestaan bij voldoend hoge temperatuur (1350-1400°C) uit één fase. Rh verhoogt de stabiliteit van de Pt-rijke fase, maar Pd verlaagt relatief deze stabiliteit. Decompositie tijdens warmtebehandeling bepaalt in sterke mate de mechanische eigenschappen: na een volledige homogenisatie blijken discontinue precipitaten op korrelgrenzen de breukrek drastisch te verlagen, terwijl in deze toestand de gemeten treksterkte het hoogst was. De optimale combinatie van rekgrens en breukrek werd gevonden na decompositie vanuit een toestand met twee fasen. Toepassing van de hiervoor aangegeven theorie leverde een vrij goede voorspelling op van de gemeten rekgrenzen.

1. Introduction

1.1. Aim of the present research

Aramid fibres are produced with so-called spinnerets (see §1.2), presently made of gold-platinum base alloys. Cost reduction in the production of aramid fibres can be accomplished by increasing the spinning speed, requiring a higher applied pressure, or by reducing the material investment by using thinner spinnerets. In both cases the strength of the spinneret alloys should be increased. The goal of this research performed by the Section Thermal Processing Technology of the Delft University of Technology is to optimise the strength of the spinneret alloys by a suitable heat treatment, e.g. ageing, and an optimisation of the chemical composition of the alloy. It is thought that the effects of ageing are maximal if the volume fraction of the supersaturated homogeneous phase at the start of the ageing treatment is maximal, preferentially 100%, yielding a maximal volume fraction of precipitates on ageing (see §2.3). However, due to excessive solid solution hardening, the alloy may suffer from a lack of cold formability.

Therefore, the aim of the present research is to investigate:

1. the state and structure of the alloys in the as received rolled state;
2. the possibilities of ageing in the as received rolled state;
3. the possibilities of homogenising the selected AuPt base alloys;
4. the possibilities of ageing after homogenisation; and
5. to present an outline for further research.

1.2. Spinnerets

Aramid (poly(p-phenyleneterephthalamide)) fibres are made by wet spinning a 99.9% sulphuric acid-polymer solution at a temperature of 80-100°C. In the spinning process the polymer solution is extruded through the capillaries of a spinneret. The spinneret is made of a gold-platinum base alloy which can withstand the highly corrosive solution. The alloy to be used should be easy to deform during the punching of the capillaries and have a high strength during service.

The production of spinnerets involves the following operations. The gold, platinum and the additional alloying elements are melted in vacuum. The alloy is cast into a vertical coquille with dimensions 15x10x1 cm. Compositional variations present after casting are reduced by annealing at T=1100°C for 30 minutes, followed by a water quench. The annealed thick plate is cold-rolled in stages to a thickness suitable for the spinneret. To eliminate strain hardening the plate is annealed halfway the cold rolling at T=900°C

for 30 minutes, followed by a water quench. After final cold rolling, homogenisation takes place at T=1100°C for 30 minutes, followed by a water quench, yielding a supersaturated state. The structure is checked for voids and inclusions. The plate is formed into a saucer shaped spinneret by a sequence of deep drawing steps. The 60μm capillaries are then punched with a sapphire needle and a surface polish is applied. The last step is ageing at T=600°C for 3 hours.

1.3. Compositions of applied alloys

The standard alloy for spinnerets is AuPtRh 69/30/1 at. % (69.5/30/0.5 wt. %). Recently an alloy was developed with composition AuPtPdRh 54/27.5/17/1.5 at. % (59/30/10/1 wt. %), which showed a higher strength and a finer structure, while maintaining the corrosion resistance [1].
Models were developed to predict the alloy's strength on the basis of a relation between strength and composition and precipitate volume fraction (see [2], and chapter 2). It was assumed that Rh serves only as a grain refiner and that Rh and Pd give rise only to solid-solution hardening of both matrix and second-phase structures as far as present. Then, an effective way to increase the strength is increasing the volume fraction of precipitates. This is achieved by increasing the amount of Pt. On the basis of the models presented in chapter 2, two new alloy compositions were chosen: AuPtRh 59/40/1 at. % (59.5/40/0.5 wt. %) and AuPtPdRh 44.5/37/17/1.5 at. % (49/40/10/1 wt. %). The composition of the alloys studied are given in Table 1. These results were obtained by sequential elements analyses with ICAP emission spectrometry. Accuracy of these analyses was about 0.1 at. %. It was observed that the compositions of an alloy in different batches could vary between the limits indicated [1].

Table 1. Composition of alloys investigated.

Name	Alloy composition in atomic %			
	Au	Pt	Pd	Rh
69/30	68.0 ± 1	31.1 ± 1		0.9 ± 0.1
59/40	59.4 ± 1	39.6 ± 1		1.0 ± 0.1
54/27.5/17	53.5 ± 1	27.9 ± 1	16.9 ± 1	1.7 ± 0.1
44.5/37/17	45.0 ± 1	36.4 ± 1	16.9 ± 1	1.7 ± 0.1

The temperatures used in the production (see §1.2) for homogenisation after cold rolling and for ageing are given in Table 2. The ageing temperatures for the 59/40 and 44.5/37/17 alloys are to be determined.

Table 2. Heat treatment temperatures.

Name	Homogenisation temperature (°C)	Ageing temperature (°C)
69/30	1100	550
59/40	1050	-
54/27.5/17	1100	600
44.5/37/17	1100	-

1.4. Constitution of the alloys

The Au-Pt system shows a miscibility gap in principle allowing ageing (see Figure 1). Ageing is essential to improve the mechanical properties of the finished product. This improvement is related to the amount of supersaturation which is present in the alloy prior to ageing. The supersaturation will be maximal if the alloy concerned shows a monophase temperature region. On the basis of the literature data available the range of monophase temperature regions for each of the alloys studied is estimated.

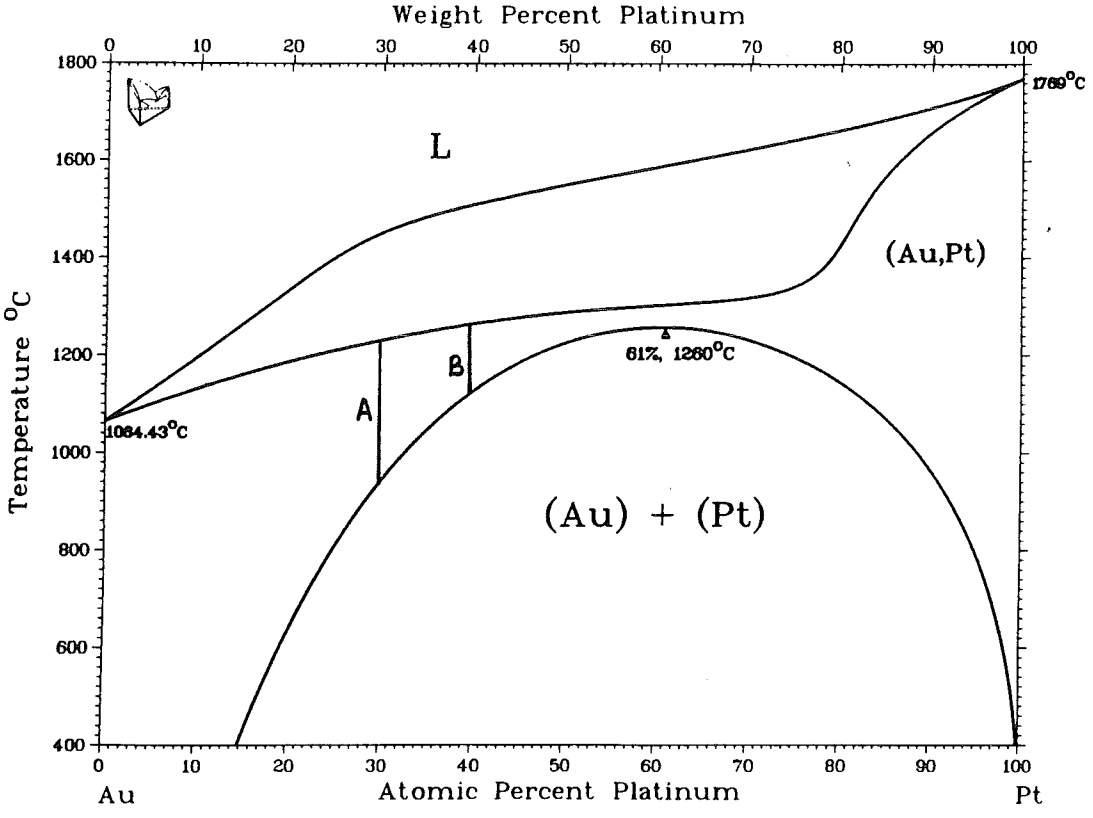

Figure 1. Au-Pt phase diagram [3].

A first estimate for the monophase temperature regions of the AuPtRh alloys can be made on basis of Figure 1, neglecting the contribution of the Rh. Then for a AuPtRh 69/30/1 at. % alloy, with composition of approximately AuPt 70/30 at. %, a monophase temperature region is present between 940 and 1220°C (as indicated in Figure 1 with line A). And for the AuPtRh 59/40/1 at. % alloy, with composition of approximately AuPt 60/40 at. %, a monophase temperature region is present between 1130 and 1260°C (as indicated in Figure 1 with line B). In this first estimate it is assumed that the Rh does not affect the miscibility gap boundaries.
The AuPtPd diagram is shown in Figure 2. A first estimate of the monophase temperature regions of the AuPtPdRh alloys can be made on basis of Figure 2, again neglecting the Rh. Then for a AuPtPdRh 54/27.5/17/1.5 at. % alloy, with composition of approximately AuPtPd 55/28/17 at. % (point A in Figure 2), the monophase temperature region starts at about 1050°C, and for the AuPtPdRh 44.5/37/17/1.5 at. % alloy, with composition of approximately AuPtPd 45/38/17 at. % (point B in Figure 2), the monophase temperature region starts at about 1125°C.

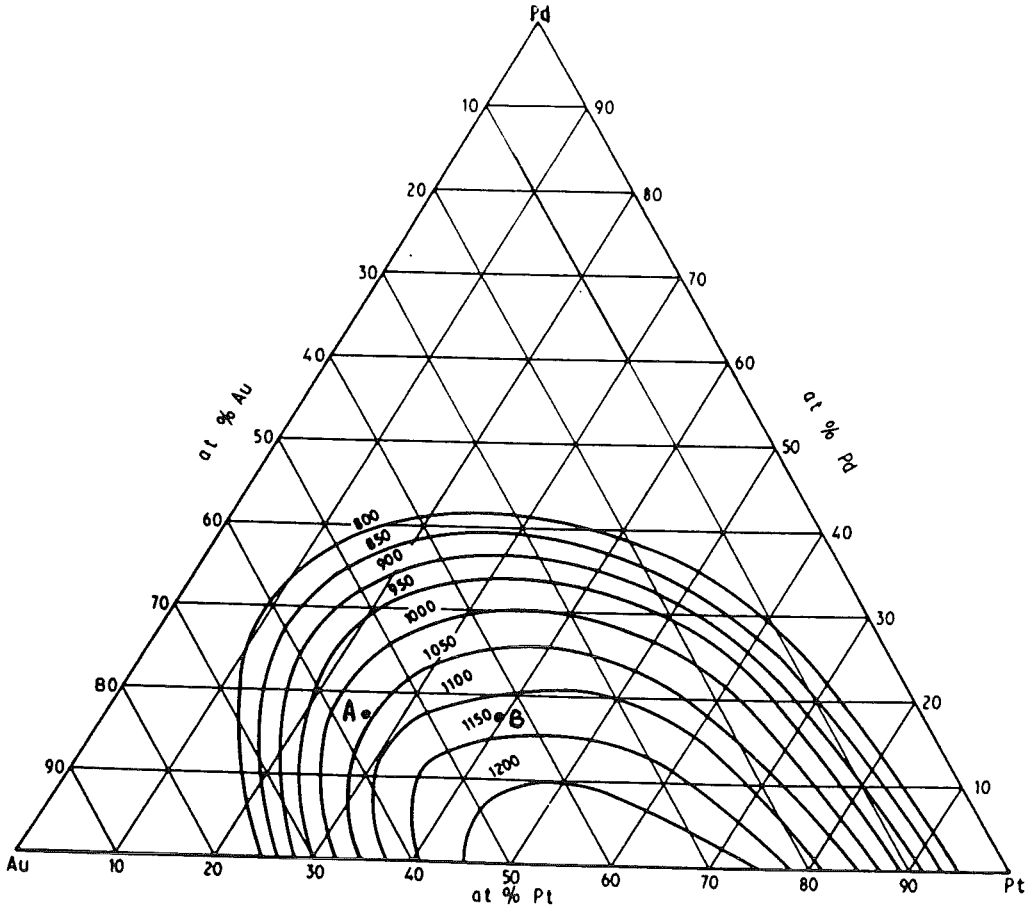

Figure 2. System Au-Pd-Pt: isotherms defining miscibility gap in ternary system [4].

Zhmurko a.o. [5] investigated the Au-Pd-Pt-Rh system. The isothermal section obtained of the AuPtRh system at 1000°C with projections of the phase boundaries for additions of 10 to 60 at. % Pd is given in Figure 3. From Figure 3 it can be seen that Pd-additions enlarge the monophase regions in this section. Alloys containing palladium should therefore be easier to homogenise than a comparable alloy without palladium. It can also be seen that the approximations for the homogenisation temperature of the alloys are not altered significantly by the addition of small amounts of Rh at 1000°C.

From the available evidence the following preliminary conclusions can be drawn:

- the 69/30 alloy should consist of one phase after homogenisation at 1100°C and quenching;
- the 59/40 alloy should contain two phases after homogenisation at 1050°C and quenching; and
- the temperature of solid solution annealing for the 54/27.5/17 alloy should at least be 1050°C and for the 44.5/37/17 alloy at least 1125°C.

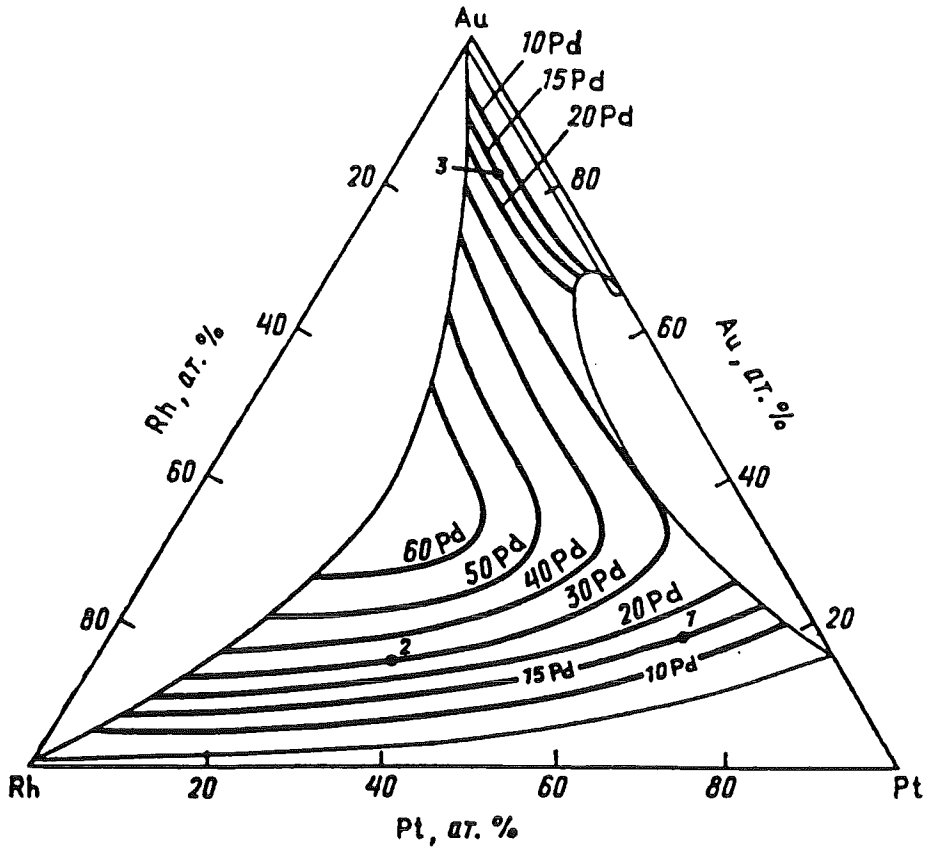

Figure 3. The Au-Pd-Pt-Rh system: isothermal section at 1000°C of the Au-Pt-Rh phase diagram with projections of the phase boundaries for additions of 10-60 at. % Pd [5].

2. Theory of strengthening

2.1. Introduction

"Yield strength" is a measure of an alloy's resistance to plastic flow, i.e. of the stress required to produce some measurable and specific permanent deformation. The Vickers hardness can often be used as a measure of yield strength as there is a constant ratio between hardness and yield stress, with the proportionality constant depending on the strain hardening coefficient [6].
Using theoretical results and experimental data it can be shown that ideal metals would fail under shear [7]: for the FCC ~~spinneret~~ alloys the relation between the theoretical strength τ, and the shear modulus G is [8]

$$\tau_{th} \approx \frac{G}{9} \qquad (1)$$

This theoretical strength is of the order of gigapascals, but the actual strength of metals is orders of magnitude below that. The explanation of this is that the lattice is not perfect: metals deform by movement of dislocations. The actual strength of an alloy can be increased by creating barriers for dislocation motion.
As martensitic reactions can be excluded for the strengthening of the alloys studied, three causes of barriers for dislocation movement remain: alloying elements in solid solution, precipitates, and other dislocations introduced by cold deformation, corresponding respectively to solid solution strengthening, precipitation strengthening and strain hardening.
Strain hardening can be excluded by virtue of the fact that cold-rolling and spinneret forming are followed by a heat treatment at a temperature close to that of recovery and recrystalisation, thereby eliminating excess dislocations. Hence, solid solution strengthening and precipitation strengthening are considered as the important strengthening mechanisms. However, it should be noted that the strain hardening which occurs during the cold formation of the spinneret and during the cold punching of the capillaries may exert an influence on the kinetics of the precipitation and on the size distribution of the precipitates. For example, due to the heterogeneity of the defect concentration, areas around the capillaries can be overaged, while the bulk of the spinneret is at maximum attainable strength [1].
The influence of grain size on the yield strength is given by the Hall-Petch relation [7]. In a first approach it is however assumed, that the grain size influence can be neglected, because of the rather large amounts of grain refiner in the alloys studied.

2.2. Solid solution strengthening

2.2.1. Introduction

Solid solution strengthening is defined as the strength increase due to a homogeneous dissolution of alloying atoms into a metal. In this paragraph the case of solid solution strengthening is discussed for a binary substitutional alloy. As the dimensions and elastic constants of the alloying atoms generally deviates from those of the base metal, a stress field occurs around each alloying atom (see Figure 4). These stress fields interact with stress fields surrounding dislocations which impedes the motion of these dislocations.

For a straight dislocation and random solute distribution, there would be a balance between the positive and negative forces exerted by the alloying atoms giving little effect on the alloy's strength. In practice such a distribution never occurs, and a dislocation line will bend under the influence of attractive and repulsive forces (see Figure 4). The bending will depend on the interaction between the atoms and the dislocation line, i.e. the binding energy. Hence, it can be expected that the strengthening effect of solid solution depends on the binding energy between the alloying atom and the dislocation, the solute concentration, and the solute distribution. It is assumed that presence of the dislocation as such does not alter the distribution of the alloying atoms, i.e. solute diffusion is too slow to allow atomic movement [9].

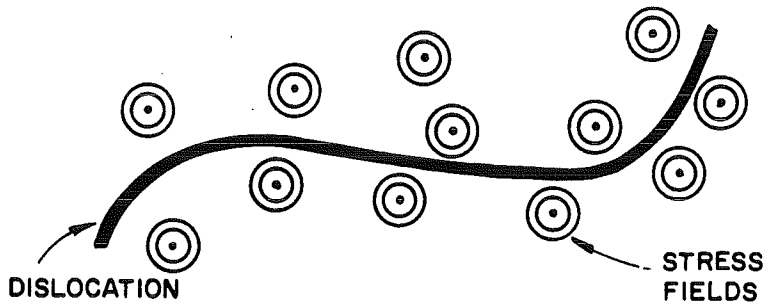

Figure 4. Dislocation bending around stress fields [7].

2.2.2. Interaction force of an alloying atom with a dislocation

The binding energy between an alloying atom and a dislocation line is of course determined by the effective interaction force. The interaction force originates from the following contributions [9]:

- dilatation misfit (or elastic misfit): the size of the alloying atoms deviates from that of the base metal atoms; this term is denoted as the parelastic interaction;
- interaction due to the difference in elastic constants; this term is denoted as the dielastic interaction;

- chemical (or Suzuki) interaction: difference in solubility between matrix and stacking fault region causes solute migration; and
- local order interaction: alloying atoms may show a tendency to occupy preferent lattice sites.

According to Haasen [10], the Suzuki interaction is unimportant if the alloying atoms are immobile, which is assumed for the alloys at the temperatures concerned. Until now, no evidence is available about local ordering in the spinneret alloys studied. Therefore the last two contributions are ignored. The first two contributions will be present in spinneret alloys and are treated briefly. These contributions are assumed to be mutually independent.

The interaction force has two components: the parelastic interaction due to size misfit (permanent 'elastic moment') and dielastic interaction due to modulus misfit (where the distortion field of the dislocation induces an elastic moment). Different interactions exist for edge dislocations and for screw dislocations. These contributions to the interaction energy can be differentiated to the position, x, to give the interaction force.

For the *parelastic* interaction, it is assumed that the alloying atom acts as a dilatation centre of spherical symmetry. Its substitution for a host atom changes the volume of the otherwise unstrained lattice. The change δ in the lattice parameter, a, with solute concentration, c, including second-order parelastic interactions to include the contributions of both screw and edge dislocations (see [9]), can be expressed as [9,11]

$$\delta = \frac{1+\nu}{3(1-\nu)}\frac{d\ln a}{dc} = \frac{1+\nu}{3(1-\nu)}\frac{1}{a}\frac{da}{dc} \qquad (2)$$

where ν is the Poisson's ratio. The maximum interaction force due to parelastic interaction in the FCC lattice can be written as [9]

$$F^{p}_{max} \approx Gb^2\delta \qquad (3)$$

The *dielastic* interaction originating from the fact that the atom will in general change the elastic constants in its environment. Since the elastic energy density of the dislocation is proportional to the shear modulus G, there will be an interaction energy caused by this modulus change. The macroscopic modulus change η is given by [9,11]

$$\eta = \frac{d\ln G}{dc} = \frac{1}{G}\frac{dG}{dc} = \frac{2(G_s - G)}{(1+\alpha)G + (1-\alpha)G_s} \qquad (4)$$

where G is the shear modulus of the matrix, G_S the shear modulus of the solute, and α is given by [11]

$$\alpha = \frac{\nu - \frac{1}{5}}{3(1-\nu)} \tag{5}$$

so for $\nu = 0.4$ (which is the case for gold, see Table 20) α becomes 1/9. The maximum interaction force due to dielastic interaction in the FCC lattice can be written as [9]

$$F^d_{max} \approx Gb^2\beta\eta \tag{6}$$

For FCC metals, β equals [10]

$$\beta = \left[(1-\nu)^2 24\pi \frac{z}{b}\right]^{-1} \tag{7}$$

where z is the distance between the slip plane and the parallel plane through the foreign atom, and $z \approx b$ [10]. With $\nu = 0.4$ β is about $\frac{1}{27}$. Numerically, η is often found to be 20 times larger than δ. Hence, both interactions, the parelastic and the dielastic, are found to be of equal importance.

Under certain conditions the parelastic and dielastic interactions of an alloying atom, for both screw and edge dislocations, can be superposed yielding the effective interaction force F^{eff}_{max} [10]

$$F^{eff}_{max} \approx Gb^2\sqrt{\delta^2 + \eta^2\beta^2} \tag{8}$$

2.2.3. Interaction force of many alloying atoms with a dislocation

In a real solid solution a dislocation will interact with many alloying atoms at the same time. A calculation of the overall effect of forces exerted by all alloying atoms on a dislocation line length was performed by Labusch [12,13,14,15].

Consider an edge dislocation of finite line tension, T, having many alloying atoms on both sides of the slip plane. With no applied stress, the dislocation will occupy a position of zero net force. As the applied shear stress, τ, is increased from zero, the dislocation will experience net forces due to the alloying atoms. For the moment it is assumed that these alloying atoms act as point obstacles and that on the atomic scale all deformations are elastic.

Labusch deals with the statistical aspects of a dislocation moving through a random array of point obstacles. Labusch takes into account the fact that, due to the restraining effects of the dislocation line tension, all point obstacles do not act with their maximum force on the dislocation line at the same time. There will be a distribution function $\rho(F)$ giving the number of interactions of strength F with unit length of dislocation at a given shear stress τ. Therefore $\rho(F).dF$ will give the number of interactions of strength (F,F+dF) with a unit length of dislocation at a given shear stress τ. ρ depends on τ, except for the critical state where it becomes stationary, $\frac{\partial \rho}{\partial \tau}|_c = 0$ (where c denotes the critical state), which just means that at shear stress just above τ_c the dislocation starts moving, i.e. macroscopically plastic deformation begins, thus $\tau_c = \tau_y$.
The condition of force balance for the dislocation is, for any shear stress not exceeding the critical shear stress

$$\tau b = \int \rho(F).F.dF = \int \rho(y).F(y).dy \qquad (9)$$

where the Burgers vector b of the edge dislocation is lying in the x-direction and the y-direction lies also in the slip plane, F(y) is the force-distance profile of the centre obstacle along the y-axis, and $\rho(y).dy$ is the number of interactions at (projected) spacings y between alloying atoms near the slip plane and a dislocation which is almost parallel to the x-direction, and $dy/dx \ll 1$ (see Figure 5).
Labusch's derivation of $\rho_c(y)$ proceeds as follows: one considers a dislocation and a special obstacle at the origin under the average action of neighbouring obstacles with all possible distributions. Moving the line from position 1 to position 2 by dl at infinite x (Figure 5), the displacement at finite x is

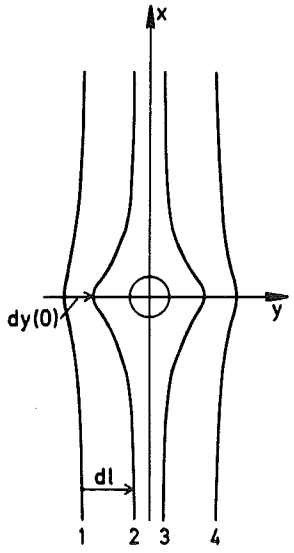

Figure 5. Dislocation in various positions relative to a foreign atom repelling it. [9]

$$dy(x) = dl - G(x).dF = dl - G(x)\frac{dF}{dy}dy(0) \qquad (10)$$

Here F(y) is the force-distance profile of the center obstacle along the y-axis; G(x) is the elastic Green's response function by which the dislocation reacts to the application of a point force at x=0 in the average environment of the other obstacles.
G(x) is shown [13] to obey the differential equation

$$T\frac{d^2G}{dx^2} - \xi G(x) = 0 \qquad (11)$$

where

$$\xi = \int \rho(y).\frac{dF}{dy}.dy \qquad (12)$$

is the average curvature of the obstacle interaction potential. The solution of equation (11) is

$$G(x) = \frac{1}{2\sqrt{\xi T}}\exp(-|x|\sqrt{\frac{\xi}{T}}) \qquad (13)$$

The function G(x) depends on ρ via ξ. It reaches a stationary form for the critical distribution ρ_c which follows from $\frac{\partial \rho}{\partial l} = 0$. With the help of equation (10) Labusch defines

$$g(y) \equiv \frac{dy(0)}{dl} = \frac{1}{1 + G(0)F'(y)} \qquad (14)$$

which enters the continuity equation for $\rho(y)$

$$\frac{\partial \rho(y)}{\partial l} = -\frac{\partial}{\partial y}(\rho(y)g(y)) \qquad (15)$$

For the stationary state, therefore, $(\rho_c.g) = \text{constant} = \frac{c}{a^2}$, the areal density of obstacles, is

$$\rho_c = \frac{c}{a^2}[1 + G(0)F'(y)] \qquad \text{or} \qquad \rho_c = 0 \qquad (16)$$

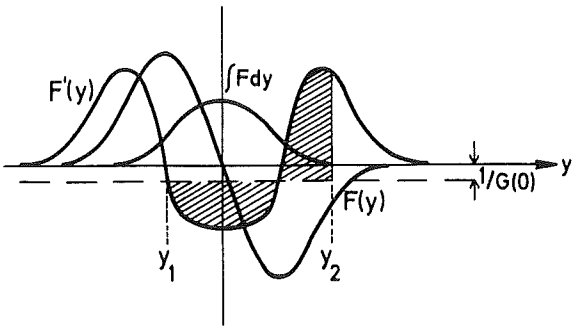

Figure 6. Asymmetric distribution function $\rho \propto (1+G(0)F'(y))$ of Labusch theory [13] relative to force-distance profile F(y) of foreign atom-dislocation interaction. In the gap $y_1 \leq y \leq y_2$, defined by the graphical construction, $\rho = 0$. [9]

It appears very reasonable that the slope of a force-distance profile should determine how many dislocation elements get stuck. Figure 6 shows graphically the relation of ρ_c to the force profile and shape of the potential hill. Since ρ cannot be negative, it must be set zero where $(1+G(0)F'(y)) < 0$. However, $\rho.dy$ must not be changed by this procedure, so, for dislocations to be driven to the right, $\rho_c = 0$ for $y_1 \leq y \leq y_2$ as defined in Figure 6. It is this asymmetry of $\rho_c(y)$ that yields a finite τ_c when integrated with a symmetric force profile F(y).
Neglecting for the moment the first term in equation (16), one obtains from equation (9)

$$\tau_c b = \frac{c}{a^2}\frac{1}{2}\frac{1}{\sqrt{\xi T}}\frac{1}{2}F_{max}^2 \qquad (17)$$

with

$$\xi = \frac{c}{a^2}\frac{1}{2}\frac{1}{\sqrt{\xi T}}\int_0^{F_{max}}\frac{\partial F}{\partial y}dF \qquad (18)$$

Scaling F by F_{max} and y by the range z of the force-distance profile yields Labusch's result

$$\tau_c b = \frac{c^{2/3}F_{max}^{4/3}z^{1/3}}{a^{4/3}T^{1/3}2(4I)^{1/3}} \qquad (19)$$

with I a pure number of the order of 1 [10]:

$$I = \int_0^1 \frac{\partial(F / F_{max})}{\partial(y / z)} dF / F_{max} \qquad (20)$$

The neglect of the first term in equation (16) limits the validity of equation (19) to those combinations of parameters for which

$$\frac{F_{max} a^2}{Tcz^2} >> 4I \qquad (21)$$

This condition is met in case of relatively dilute solutions and not too weak obstacles. When the first term in equation (16) is not neglected, thus for weak obstacles and higher concentrations, the increase in shear stress reduces and even vanishes as the gap in the distribution function ρ reduces, because the maximal value of $F'(y)$ gets smaller, and the asymmetry of the distribution function disappears altogether when $(1+G(0)F'(y)) > 0$ everywhere. In the derivation a single obstacle was used and all other obstacles were assumed to have only a statistical average value in the direct surroundings of the one obstacle. This assumption is not very realistic when weak obstacles (and large concentrations) are concerned. Groups of obstacles will then function as one obstacle, and these groups will vary in size, strength and distribution. When the simplification is made that all groups have the same strength a similair derivation as the previous one follows [9,14]. Alloying atom clusters of i atoms each form type (i) obstacles. Their mean strength is $(i)^{1/2}F_{max}$, their concentration $\frac{c}{i}$. The final result of the Labusch theory, equation (19), is unchanged although the range of applicability of the theory, equation (21), is extended by a factor $i^{3/2}$ to higher c, smaller F_{max}. Of course the dimensions of the cluster must remain small compared to $(T/\xi)^{1/2}$, equation (13). Together with equation (19) this condition just means $c \ll 1$. Labusch's theory enables the calculation of the superposition of the forces of different kinds of obstacles on the same dislocation: one defines two density functions, two solute concentrations and two maximum forces (letting the range of interaction z be the same) resulting in [9]

$$\tau_c b = \frac{z^{1/3}}{a^{4/3} T^{1/3} 2(4I)^{1/3}} (c_1 F_{1,max}^2 + c_2 F_{2,max}^2)^{2/3} \qquad (22)$$

In practice only the alloying atoms next to the slip plane make a significant contribution to solid solution strengthening so that z has a value of atomic dimensions (about one half the seperation of the {111} planes in the FCC latice [11]).

2.2.4. Result for solid solution strengthening

To calculate the solid solution strengthening effect, it is necessary to combine equations (8) and (19). Using $z \approx b \approx a\sqrt{3}/2$ [11], and $T = Gb^2/2$ [8], then the following equation for the contribution to the yield shear stress due to solid solution strengthening, τ_y^{SS}, is obtained

$$\tau_y^{SS} = k^{SS} G c^{2/3} (\delta^2 + \beta^2 \eta^2)^{2/3} \tag{23}$$

where

$$k^{SS} = \left(\frac{3}{16\sqrt{I}} \right)^{2/3} \tag{24}$$

It should be noted that equations (23) and (24), although they were derived for edge dislocations only, also apply to screw dislocations when a second-order parelastic interaction parameter of order unity is introduced [9]. The assumption that the alloying atoms act as point obstacles has also been investigated by Labusch [15], and has been shown to have a negligible effect.

According to equation (23), solid solution strengthening should show a $c^{2/3}$ dependence, where c is the solute concentration. Experimental results confirm this dependence, as seen in Figure 7.

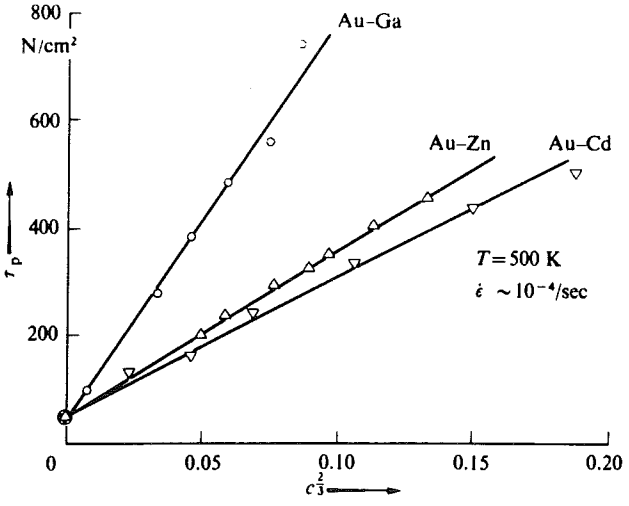

Figure 7. Critical shear stress of gold solid solutions at 500 K [10].

The slope of the concentration dependence of τ, the specific hardening, should be related to the strength of the elastic interaction of an alloying atom with a dislocation, as described by the parameters δ and η. As can be seen from Figure 8, the slopes are satisfactorily explained by the combination of the solute parameters in F_{max}.

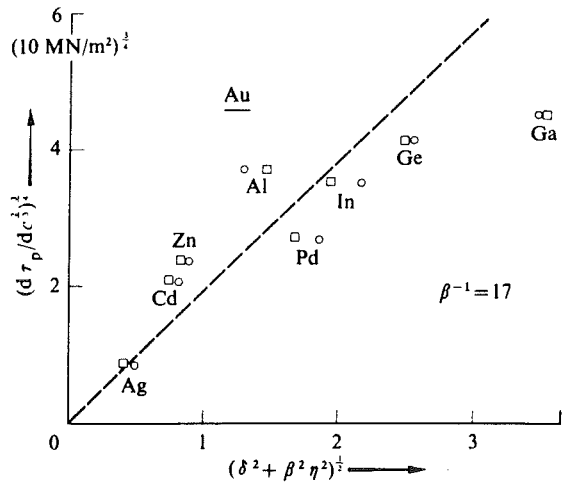

Figure 8. Specific hardening of gold solid solutions (slope of the lines in Figure 7) plotted against the strength of the elastic interaction of an alloying atom with a dislocation. Circles or squares are obtained for a different choice of second-order parelastic interaction between solute atom and screw dislocation [10].

According to equation (23), the solid solution strengthening effect will be large for alloying elements that differ much from the matrix; these elements show little solubility.

2.3. Precipitation strengthening

2.3.1. Introduction

In a precipitation hardened alloy, the small dispersed particles were originally in supersaturated solid solution obtained by rapid cooling from a sufficiently high temperature. The heat treatment that causes precipitation consists of the following steps: dissolution, quenching, and ageing. The precipitates give rise to local distortions and strain fields which restrict the dislocation mobility [7,8,16]. The increase in yield shear stress depends on the strength, structure, spacing, size, shape, and distribution of the precipitate particles as well as on the degree of misfit or coherency with the matrix and on their relative orientation [17].

In the following it is assumed that all precipitates have the same size and a spherical form. The distribution is assumed to be random and due to the assumed spherical shape the relative orientation of the precipitates is no longer an influence factor. The increase in yield shear stress due to precipitates can be separated into two parts

$$\tau_y^p = \tau_{LR} + \tau_{SR} \qquad (25)$$

where τ_{LR} the shear stress necessary to overcome the long-range dislocation interaction, and τ_{SR} the shear stress necessary for overcoming the short-range dislocation interaction.

2.3.2. Long-range particle-dislocation interaction

Mott and Nabarro [see 7 and 16] based their theory on the analysis of internal shear stresses resulting from the difference in average atomic volume of the matrix and of that of the precipitates. By considering a spherical precipitate embedded coherently in an infinite matrix, they derived for the critical yielding shear stress τ_{LR} in the alloy

$$\tau_{LR} = 2G\varepsilon f \qquad (26)$$

where G is the matrix shear modulus, f the precipitate volume fraction, and ε the dilatation misfit between the precipitate and the matrix $\varepsilon \approx \frac{2}{3}\frac{\Delta a}{a}$ [9] where a is the lattice parameter of the matrix and Δa the difference in lattice parameter between particle and matrix. According to equation (26), the critical shear stress is independent of the size and of the spacing between the particles, and depends only on the precipitate volume fraction and the degree of misfit. However, a dislocation is a flexible line with tension T. The radius of curvature, r_c, of such a dislocation line, with Burgers vector b, can be reduced by an applied shear stress, and is approximately given by [7]

$$r_c = \frac{Gb}{2\tau_{LR}} = \frac{b}{4\varepsilon f} \qquad (27)$$

Thus, the dislocation line, being flexible, can avoid the obstacles by bending around the precipitate stress fields (see Figure 4). When the precipitate is dispersed on a scale finer than the radius of curvature of dislocation, the dislocation will not be able to bend sufficiently to be entirely in the low-internal-energy regions and the algebraic sum of all the interactions will be zero. The alloy will be soft and ductile, as there will be little resistance to dislocation movement. Thus, the radius of curvature must be of the same order of magnitude as the interparticle spacing for the Mott-Nabarro model to be valid. The theory predicts a minimal interparticle spacing for a long-range strengthening effect to occur. When the interparticle spacing is larger than this minimal value, the value of τ_{LR} will only depend on f and ε.

2.3.3. Short-range dislocation-particle interactions with and without particle shear
When a dislocation is moved by an applied shear stress on one of the slip planes of the matrix, it will encounter precipitates and interact with them on a short range. Depending on the nature of the precipitate and on the crystallographic relationship between the precipitate and the matrix, one can have two limiting cases [7,9]: the spherical precipitates will or will not be sheared. Both cases are shown in Figure 9.

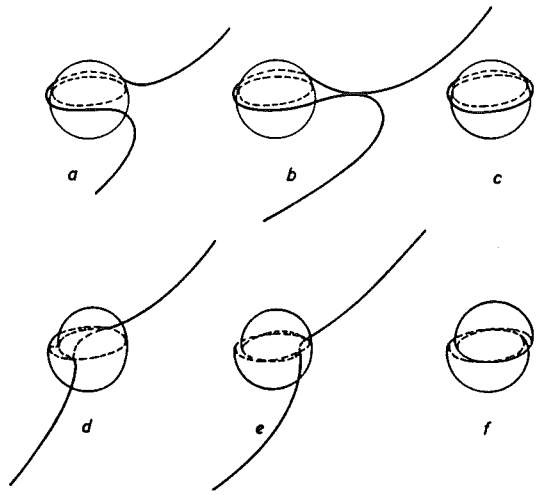

Figure 9. Schematic view in three sequences of the Orowan mechanism (a)-(c) and the shear mechanism (d)-(f). Figures (a) and (d) describe the critical position of an edge dislocation with maximum repelling force acting on the dislocation moving from left to right under an applied shear stress. [9]

The precipitate particles are impenetrable to the dislocations.

Orowan [18] pointed out that an additional shear stress will be necessary to make a dislocation expand between the particles. Should the shear stress be sufficiently high to bend the dislocations in roughly semicircular form between the particles, the dislocations go around the particles, leaving dislocation loops around them.
If Λ is the average interparticle spacing, then the yield shear stress for an alloy strengthened by an impenetrable precipitate is given by [7]

$$\tau_{SR,Orowan} = \frac{Gb}{\Lambda} \qquad (28)$$

More precise formulations of the Orowan stress have been made involving more accurate expressions for the dislocation line tension T and taking into account the effect

of the finite particle size on the average interparticle spacing, but these modifications do not change equation (28) essentially.

The precipitate particles are penetrable to dislocations.

The particles are sheared by dislocations in their slip planes. If the extra shear stress necessary for particle shear is less than the Orowan stress, the dislocation will cut the spherical particles (radius r_p). The passage of a matrix dislocation, which generally will not be a slip dislocation for the precipitate, will result in a faulted plane or an interface of specific energy γ. Then, in the absence of any thermally activated process, the shear stress necessary to move a dislocation, with a length x, by particle shear is given by [7]

$$\tau_{SR,Shear} = \frac{\pi\gamma r_p}{2xb} \qquad (29)$$

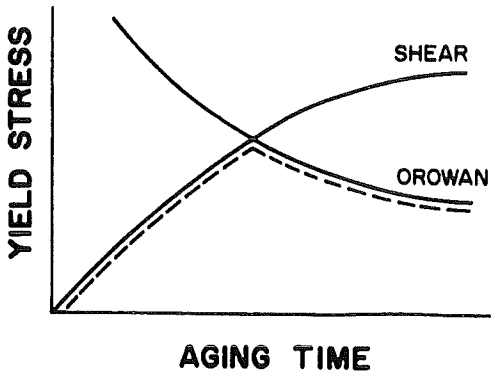

Figure 10. Variation of yield stress with ageing time [7].

Whether or not the particles will be sheared depends on the particle size and on the specific interface energy.
With ageing, the second-phase particles grow in size so that the average spacing between them also increases (for a given precipitate volume fraction) and $\tau_{SR,Orowan}$ for expanding the dislocation between particles decreases monotonically. But the stress necessary to cut the particles, $\tau_{SR,Shear}$, increases with the particle's size. The yield stress of the alloy then, will follow the dashed curve as a function of ageing time in Figure 10 and τ_{SR} will be maximal where $\tau_{SR,Orowan} = \tau_{SR,Shear}$.

2.3.4. Combining long- and short-range interaction
Combining the contributions for precipitation strengthening the situation is complex. There is a long range contribution (equation (26)), and two competing types of short range contributions (equations (28) and (29)).

From equation (26) and (27) the maximum long range interaction shear stress is obtained

$$\tau_{LR} = \frac{Gb}{2r_c} = \frac{Gb}{\Lambda} \tag{30}$$

where $\Lambda=2r_c$ is the interparticle spacing, with r_c the radius of curvature of the dislocation line.
The maximum short range interaction shear stress, where $\tau_{SR,Orowan} = \tau_{SR,Shear}$, is according to equation (28)

$$\tau_{SR} = \frac{Gb}{\Lambda} \tag{31}$$

which, combined with equation (29), gives for the precipitate radius at maximum short range interaction

$$r_p = \frac{2Gb^2}{\pi\gamma}\frac{x}{\Lambda} \tag{32}$$

where the interfacial energy γ is in the order of magnitude of antiphase domain boundaries $\gamma \approx 0.1$ J/m^2 [7,9,10].
The volume fraction of spherical precipitate present, f, is given by [7]

$$f = \frac{4}{3}\pi r^3 N \tag{33}$$

where r is the precipitate radius and N the number of precipitates per unit volume.
The interparticle spacing is [7]

$$\Lambda = N^{-1/3} - 2r_p \tag{34}$$

and x in equation (29) is

$$x = N^{-1/3} \tag{35}$$

By substituting from equation (33), (34) and (35) in (32) an expression for r_p can be found, which gives

$$r_p = \frac{2Gb^2}{\pi\gamma}\frac{1}{1-2\left(\frac{3f}{4\pi}\right)^{1/3}} \qquad (36)$$

The maximal strengthening of an alloy by precipitation, τ_y^P, is then

$$\tau_y^P = \tau_{LR} + \tau_{SR} = 2\frac{Gb}{\Lambda} = \frac{\pi\gamma}{b}\left(\frac{3f}{4\pi}\right)^{1/3} \approx 1.949\frac{\gamma f^{1/3}}{b} \qquad (37)$$

It should be noted that when the effect of the particle size, r_p, on the interpartcile spacing, Λ, is neglected in equation (34) Λ=x, but the final equation (37) remains the same. Neglecting the second half of equation (36) will result in a calculated r_p which is too small. This error in calculated r_p increases as the precipitate volume fraction, f, increases.

2.4. Solid solution and precipitation strengthening

In the preceeding sections the effects of solid solution strengthening and precipitation strengthening are given in terms of shear stress. The effects on the yield strength can be obtained by application of the geometrical Taylor factor, m, which is 3.06 for polycrystalline FCC metals without any texture [19]. When two or more different phases are involved, the resulting physical properties of the compound are usually constructed from those of the constituent phases by volume weighted averaging [20]. Equation (23) regards only the effect on the shear stress by solid solution strengthening. The value of the yield strength, σ_y^{SS}, of a solid solution is assumed to be equal to

$$\sigma_{y,Me}^{SS} = \sigma_y^{Me} + m\tau_y^{SS} \qquad (38)$$

where σ_y^{Me} is the yield strength of the base metal of the phase in the annealed condition. Equation (37) regards the effect on the shear stress by precipitation strengthening. The value for the yield strength of an alloy strengthened by precipitation, σ_y^{PS}, is assumed to be given by

$$\sigma_y^{PS} = (1-f)\sigma_{y,m}^{SS} + f\sigma_{y,prec}^{SS} + m\tau_y^P \qquad (39)$$

where $\sigma_{y\ m}^{SS}$, $\sigma_{y\ part}^{SS}$ are the values for the yield strengths for the solid solutions of matrix and second phase particles respectively given by (38).

2.5. Effects of thermal activation

The strengthening effects which were discussed in the previous section are only valid at temperature T=0 K. At finite temperatures there is a decrease in yield shear stress and strengthening effect. This is attributed to thermal fluctuations which help the dislocations to pass over localized obstacles under forces $F < F_{max}$.
In the Labusch theory, for example, the effect of thermal activation can be approximated by [9]

$$\tau_y(T) = \tau_y(T=0).\exp\left(-\frac{2kT}{F_{max}z}\ln\frac{\nu_0 z}{V}\right) \qquad 1 \le \frac{\nu_0 z}{V} \le 100 \qquad (40)$$

where $k=1.3806.10^{-23}$ (J/K) is the boltzmann constant, T is the temperature in Kelvin, V is the dislocation velocity (which is assumed to be constant), and the atomic attempt frequency $\nu_0 \approx 10^{10}$ Hz.
For spinneret alloys under service temperature of T=350 (K), when taking for Au $z=3.5.10^{-10}$ (m), for Pt in Au $F_{max}=1.4.10^{-10}$ (N), and V=0.5 (m/s) (being in the centre of the domain of equation (40) [9]), equation (40) means a change of the proportion between the normal stress σ and the shear stress τ from the Taylor factor 3 to about 2, and this value can be used instead of m in equations (38) and (39).

3. Experimental Procedures

3.1. Heat treatment and specimen preparation

The specimens have typical dimensions of 9x8x0.8 or 0.6 mm and were obtained out of the plate by cutting.
For thermal treatments three furnaces were available: a Degussa Durferrit for all treatments below 1100°C with an accuracy of ±1°C, a Smit furnace at temperatures between 1100-1300°C with an accuracy of ±15°C and a tube furnace of Carbolite Furnaces at all temperatures above 1100°C with an accuracy in the hot zone of ±0.25°C. The Smit furnace was not used for the temperature treatments at 1270°C due to the high fluctuation of the specimen temperature. The specimen containers were Al_2O_3-ceramic pans for temperatures up to 1150°C, a quartz glass tube up to 1270°C and Alsint tubes for all temperatures above 1270°C. After heat treatment all specimens were quenched in water.
After the heat treatment the specimens were prepared for metallographic examination. To handle the specimens two types of specimen holders were used and compared. First stainless steel was used to clasp the AuPt-plate between two thick stainless steel plates. This method should make it possible to use the same specimen several times, but the stainless steel proved to be an effective protection against etching (investigated etching solutions: a. 1:1 mixture of ammoniumperoxi-disulfat ($(NH_4)_2S_2O_8$) 20 % in H_2O and cyanide (KCN) 20 % in H_2O and b. 1:1 mixture of nitric acid 65% and hydrochloric acid 37%) of the AuPt-specimen by means of cathodic polarisation. All specimens were therefore embedded in a diallyphtalate thermosetting (10 minutes at 150°C) resin with glass filler: Struers Resin 4. A Struers Predopress was used for the embedding. The embedded specimens were sanded on Struers Knuth-Rotors using sandpaper with ASTM-normation of 240, 320, 400 and 600 in sequence. After this, the specimens were polished with diamond powder: on a nylon cloth with 7 µm and on rotating cloths with 3 and 1 µm. The specimens were cleaned between the various polishing stages in a Ultramet III Sonic Cleaner filled with ethanol. Etching was performed at room temperature in a 1:1 mixture of nitric acid 65% and hydrochloric acid 37%, both extra pure or pro analysi, for durations of 30 seconds up to 2 minutes depending on the specimen, the temperature treatment and the age of the etchant.

3.2. Light microscopy and microhardness measurements

All microscopical photographs have been taken on either a Neophot 2 or a Neophot 30. The following abbreviations are used with microscopical photographs:

BF : Bright Field; sometimes used for oblique illumination to avoid entanglement with oil immersion (OI);

DIC : Differential Interference Contrast; and

OI : Oil Immersion for high magnifications.

The microhardness measurements were done on a Leitz Durimet. The indentation force was 0.981 N, applied for 30 seconds. Each reported hardness value is the average of at least 6 indentations.

3.3. Quantitative image analysis and analysis of the microcompositions

The homogeneity of the spinneret plates after recrystalisation and homogenisation at 1050-1100°C was investigated by measurement of hardness profiles and CBA-measurements of the volume fraction of second phase particles as a function of the distance from the plate surface. Overall sections were investigated using lightmicroscopical techniques.

The quantitative image analysis was done on a Leitz CBA-8000 with a Jenavert microscope. Volume fraction of the second phase was determined using BF and a magnification of 625x on specimens as polished. The centre of the area analysed was chosen as a function of the distance from the plate surface. The average volume fraction of the second phase for the alloy was calculated by averaging over the surface of the analysed areas.

The compositions of both matrix and second phase were determined for the alloys studied near the plate surface and in the centre of the plate. These measurements were performed on a Microprobe JXA 733. The accelerating voltage was 20 kV, the take-off angle 40.0°, the current 23.00 nA and the counting times for Au, Pt, Pd and Rh were respectively 30, 30, 20 and 40 seconds. These counting times combined with the applied current gave an accuracy within 0.1 at. % for the Rh and an accuracy of about 0.2 at. % for the other elements. The probe was positioned using a SEM-image of the specimen in the centre of a matrix or second phase area. The spot diameter and the penetration depth, both about 0.4 µm, were small compared to the particle dimensions, typical 10x50x50 µm. Therefore, it is reasonable to assume that the measured composition is that of the selected phase.

3.4. Differential thermal analysis

The high temperature DTA measurements were performed with a Perkin-Elmer 7 series Thermal Analysis System which is a heat-flux-DSC. Argon was used as protective gas at 15 ml per minute. The heating rate applied was 20 K per minute in a temperature range of 1150-1350°C. The platinum pans were protected against the AuPt-alloys with

Al_2O_3-powder, to avoid melting of the pans due to formation of low-melting eutectics. The temperature difference with an empty specimen holder was measured. This temperature difference was used to determine the excess heat flow that was necessary to heat up the specimen.

3.5. Tensile tests

Part of the tensile tests were performed during earlier investigations (these results are gathered in Table 7 [1,21]). For the present investigations the tensile tests were performed on a Zwick tensile testing machine (at CRU-department, AKZO Arnhem), with an applied strain of 2 mm/minute. The specimen dimensions and form are as given by Figure 11. Specimen thickness and width were determined prior to the test: values used in calculations were obtained by averaging the results of six measurements at different positions of the specimen. From the strain-stress curve the following mechanical properties were derived: the yield stress, the ultimate tensile stress, the strain at fracture, and the strain hardening coefficient The strain hardening coefficient, n, was calculated in the region of uniform plastic deformation, using the derivative of the logarithm of the true stress to the logarithm of the true strain [16].

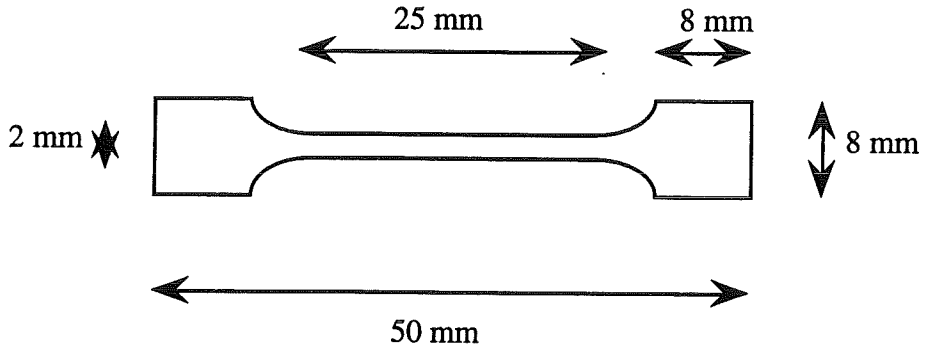

Figure 11. Tensile test specimen dimensions.

4. Results

4.1. Characterisation of the alloys after rolling and homogenisation at 1050-1100°C

The thermal history of the alloys in the as-received state is schematically shown in Figure 12. The temperatures applied are given in §1.2 and Table 2 in §1.3. The aim of this paragraph will be to characterise the microstructure and the present phases of the alloys in the as-received state.

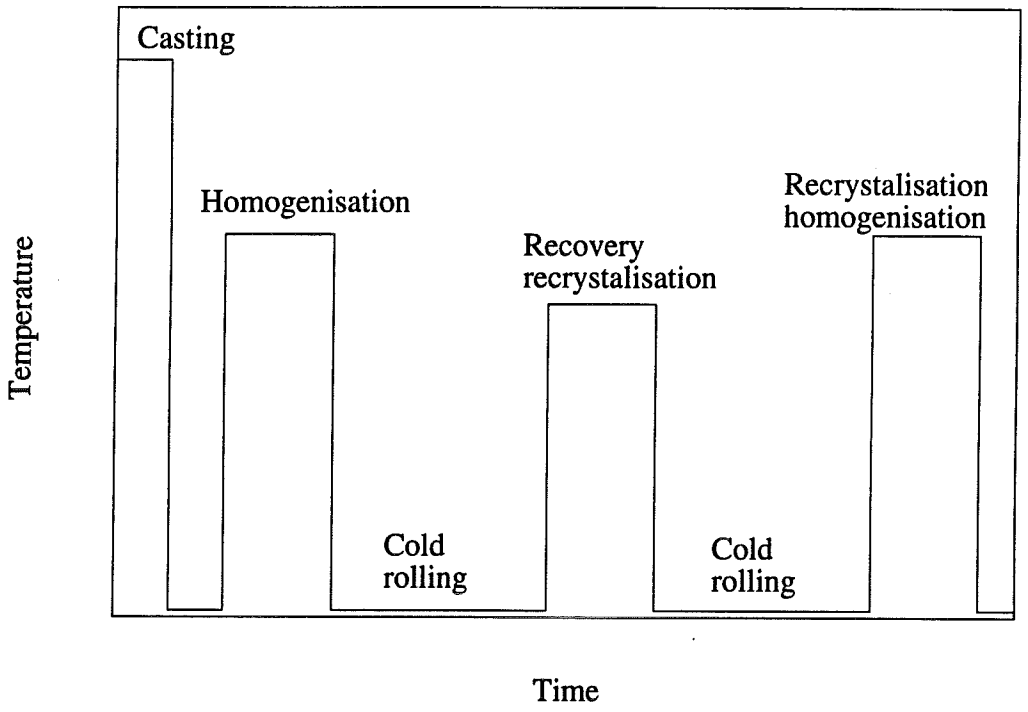

Figure 12. Thermal history of all alloys studied

The homogeneity of the spinneret plates after recrystalisation and homogenisation at 1050-1100°C was investigated.
In Figure 13, the hardness is plotted as a function of the relative distance from the surface: d/d_p where d is the distance from the surface and d_p is the plate thickness. It can be observed that the hardness depends symmetrically on the relative distance for all alloys studied. The highest hardness values are observed for the 44.5/37/17 alloy and the most pronounced hardness profile for the 69/30 alloy.
Figure 14 shows the microstructure of the 69/30 alloy parallel to the surface, whereas Figures 15-18 show sections of the alloys studied perpendicular to the surface.
From Figures 14-18, it becomes apparent that none of the alloys studied are in a monophase condition after rolling and subsequent homogenisation.

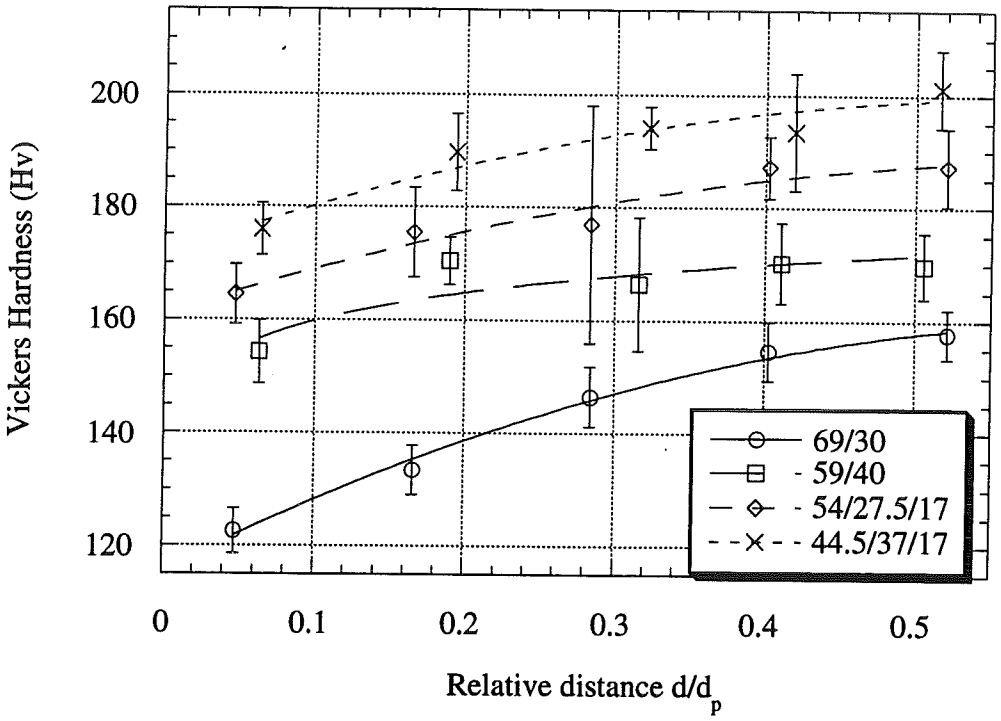

Figure 13. Hardness profile after rolling and homogenisation at 1050-1100°C.

Figure 14. AuPtRh 69/30 after rolling and homogenisation at 1100°C, parallel to surface, 500x BF.

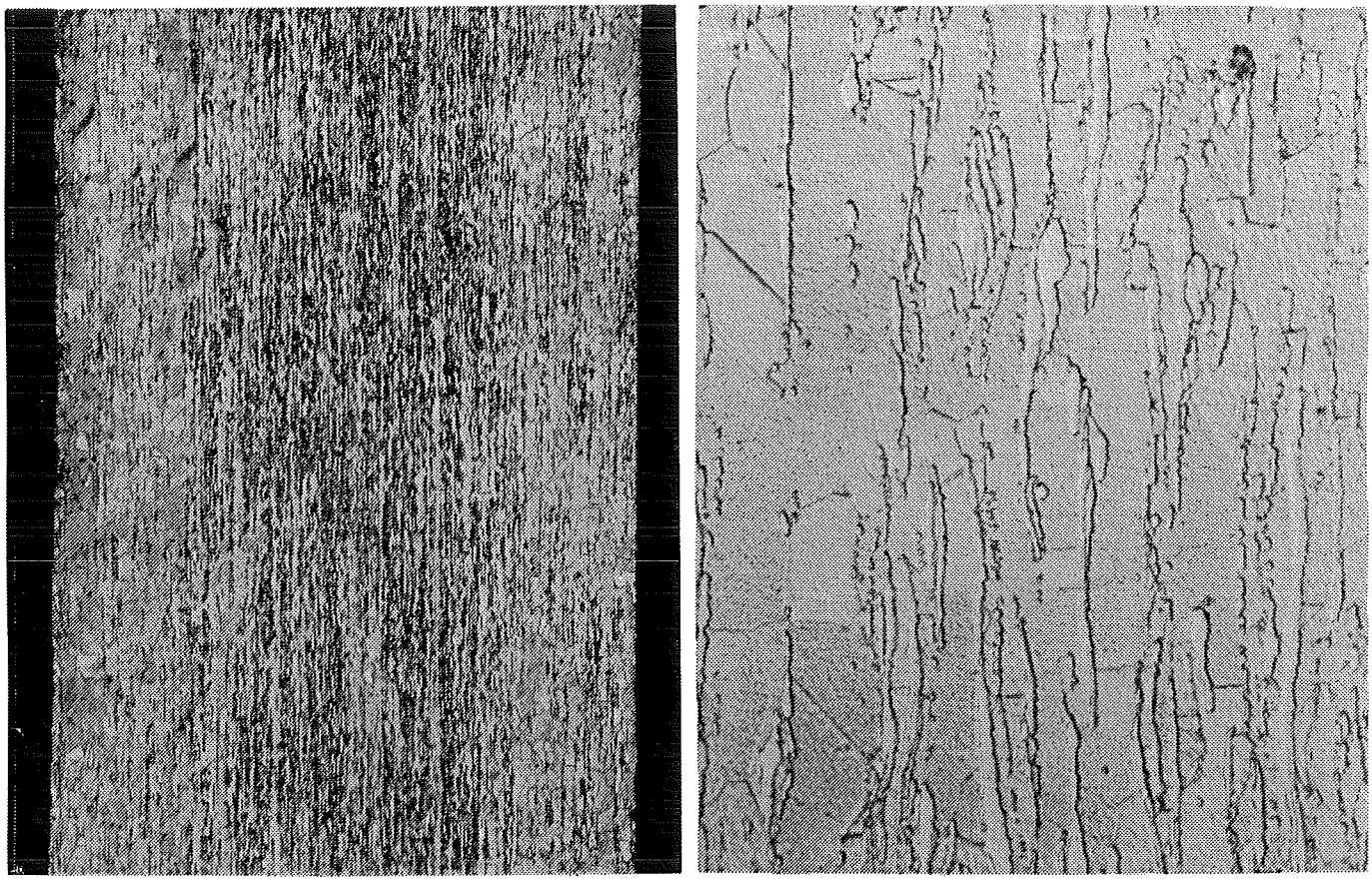

Figure 15. Microstructure photographs of AuPtRh 69/30 after rolling and homogenisation at 1100°C, left 100x BF, right 1000x BF OI.

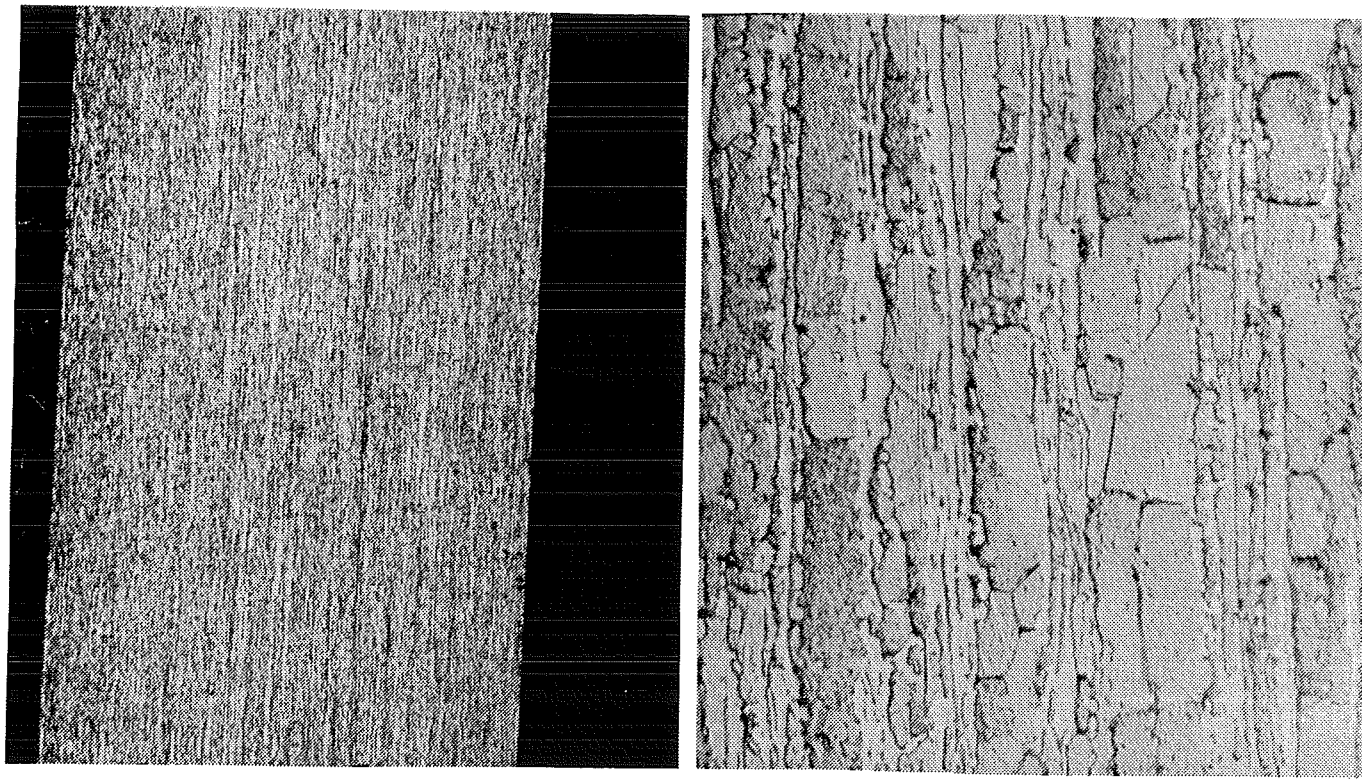

Figure 16. Microstructure photographs of AuPtRh 59/40 after rolling and homogenisation at 1050°C, left 100x BF, right 1000x BF OI.

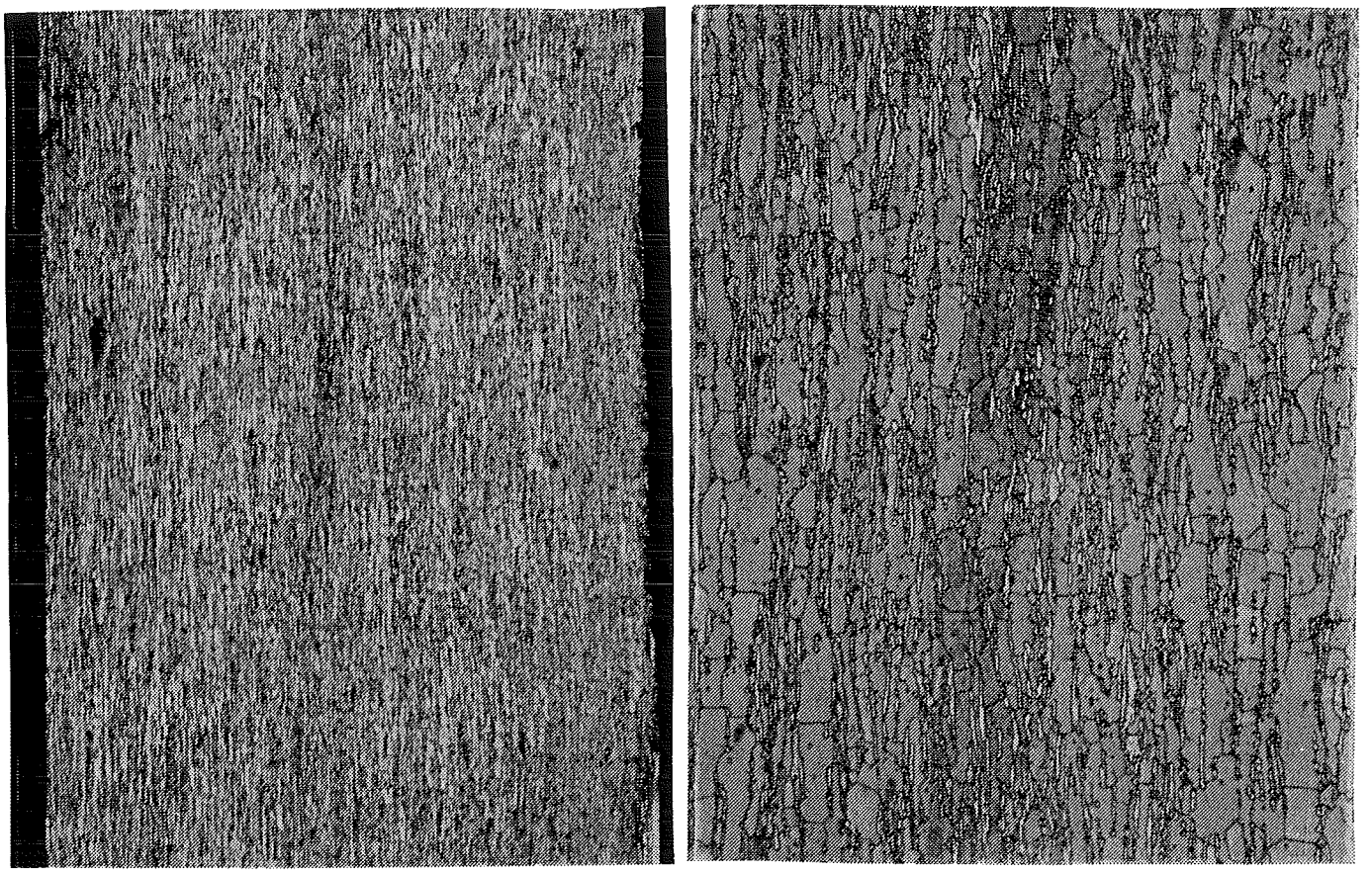

Figure 17. Microstructure photographs of AuPtPdRh 54/27.5/17 after rolling and homogenisation at 1100°C, left 100x BF, right 500x BF.

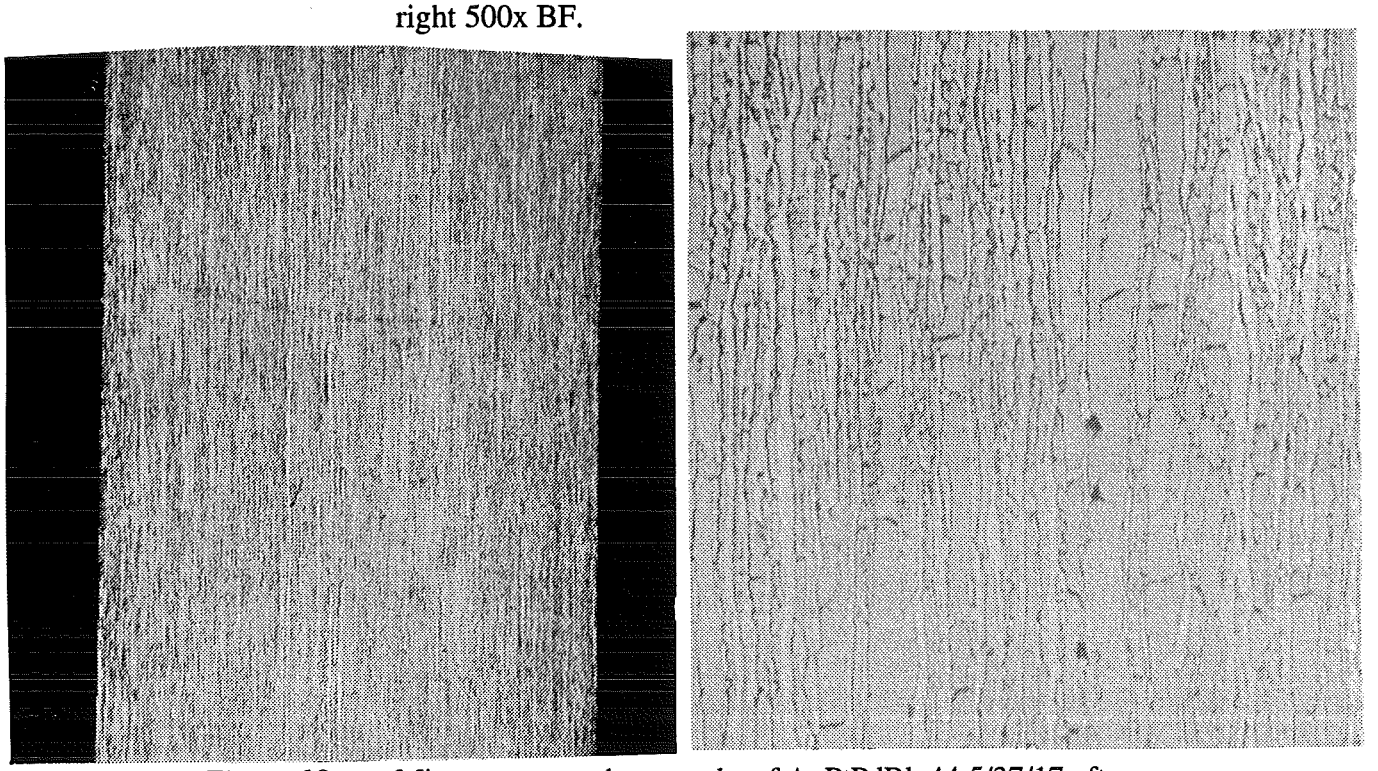

Figure 18. Microstructure photographs of AuPtPdRh 44.5/37/17 after rolling and homogenisation at 1100°C, left 100x BF, right 1000x BF OI.

The volume fraction of second phase was measured for all alloys studied. The results over the cross section of the plate are given in Figure 19. The average volume fraction of second phase particles is given in Table 3. The highest level of volume fraction of the second phase was observed for the 44.5/37/17 alloy. Again the most pronounced profile was found in the 69/30 alloy.

From the phase diagram of the Au-Pt-system (Figure 2) it follows that the second phase particles are Pt-rich particles. Supposing that the Pd addition is uniform distributed among the Au-rich and Pt-rich phases, the amount of second phase Pt-rich particles should be proportional to the ratio of the atomic fractions of Pt and Au present. In Figure 20 the average volume fraction of second phase particles (Table 3) is plotted against the ratio Pt/Au as calculated from the average alloys compositions.

Table 3 The average volume fraction second phase (f) for all alloys studied.

Alloy	f
69/30	0.082
59/40	0.147
54/27.5/17	0.112
44.5/37/17	0.210

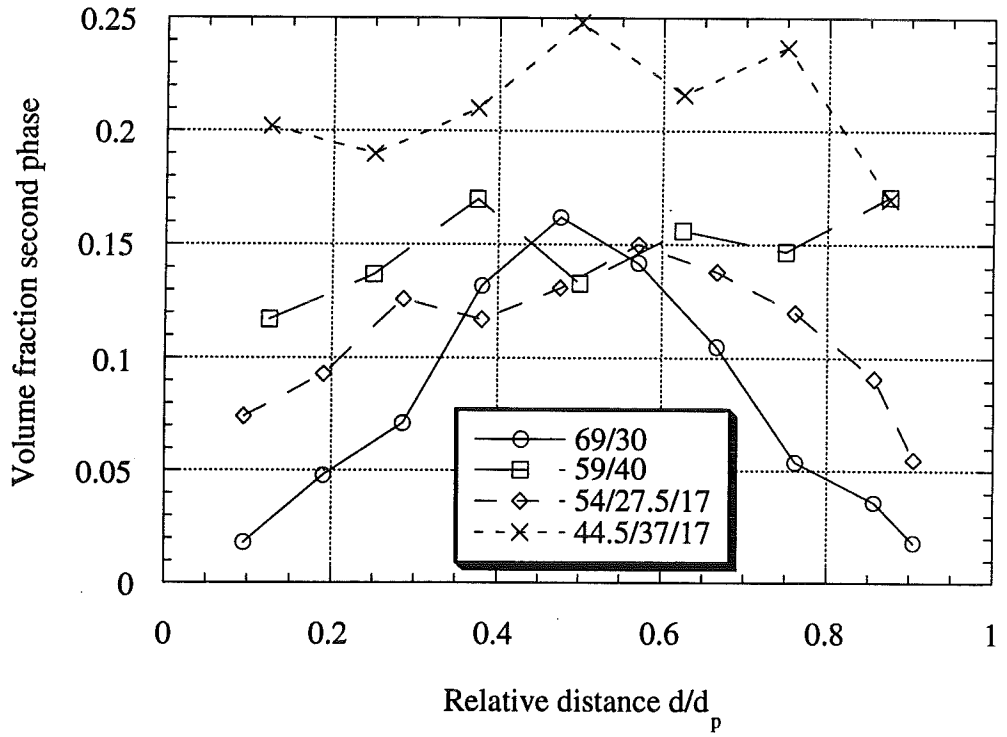

Figure 19. Volume fraction of second phase particles as a function of relative distance.

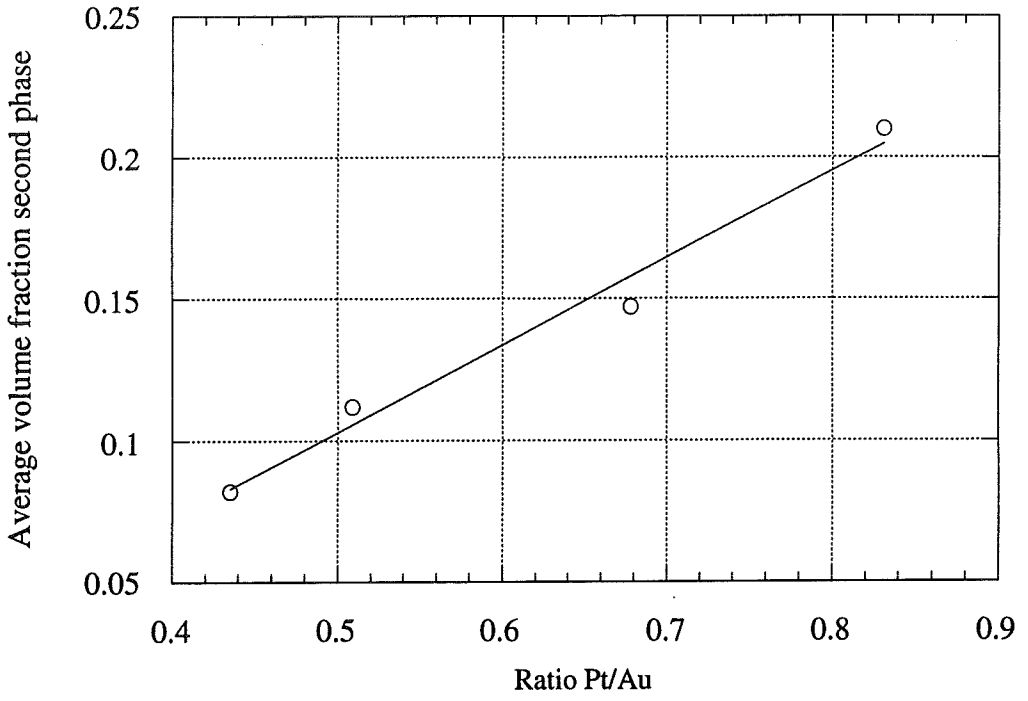

Figure 20. The average volume fraction of second phase as a function of the ratio Pt/Au.

The compositions of both matrix and second phase were determined for the alloys studied as a function of their position: near the surface or in the centre of the plate. The results are given in Table 4. As can be seen from Table 4 the compositions of the phases are very much the same near the surface and in the centre of the plate. Apart from the compositions near the surface and in the centre, the mean composition of the phase is given.

4.2. Hardness on ageing after rolling and homogenisation at 950-1200°C

After homogenisation the alloys were quenched. The hardness in the centre was measured as a function of ageing temperature with the homogenisation temperature as parameter. This preliminary investigation was performed by the alloy supplier. The alloys were heat treated for 30 minutes at a high temperature, typically 950-1200°C, quenched and aged for 3 hours at various low temperatures, typically 400-700°C. The hardnesses of the alloys after quenching from the high temperature are denoted as AQ (After Quenching). The results are shown in Figures 21-24.

Table 4. Composition of the matrix and the second phase after rolling and homogenisation at 1050-1100°C. The composition of both phases was measured near the edge and in the centre of the plate.

Alloy	Phase	Position	Au (at.%)	Pt (at.%)	Pd (at.%)	Rh (at.%)
69 / 30	Matrix	Edge	73.2 ± 0.6	26.5 ± 0.6	0	0.3 ± 0.1
		Centre	71.9 ± 0.3	27.8 ± 0.2	0	0.3 ± 0.1
		Average	72.6	27.1	0	0.3
	Second Phase	Edge	12.6 ± 1.0	80.7 ± 0.9	0	6.7 ± 0.4
		Centre	13.0 ± 1.6	81.0 ± 1.3	0	6.0 ± 0.3
		Average	12.8	80.9	0	6.3
59 / 40	Matrix	Edge	67.7 ± 0.4	32.1 ± 0.3	0	0.2 ± 0.1
		Centre	67.6 ± 0.2	32.2 ± 0.2	0	0.2 ± 0.1
		Average	67.7	32.1	0	0.2
	Second Phase	Edge	15.9 ± 1.3	80.1 ± 1.3	0	4.0 ± 0.1
		Centre	14.0 ± 0.8	82.1 ± 0.7	0	3.8 ± 0.1
		Average	15.0	81.1	0	3.9
54 / 27.5 / 17	Matrix	Edge	61.1 ± 0.3	22.1 ± 0.3	16.3 ± 0.3	0.5 ± 0.1
		Centre	59.9 ± 1.9	23.4 ± 0.6	16.1 ± 1.7	0.6 ± 0.2
		Average	60.5	22.8	16.2	0.5
	Second Phase	Edge	14.0 ± 2.0	68.7 ± 1.4	10.0 ± 1.1	7.3 ± 0.9
		Centre	13.1 ± 1.1	67.3 ± 1.2	11.2 ± 0.2	8.4 ± 0.3
		Average	13.6	68.0	10.6	7.8
44.5 / 37 / 17	Matrix	Edge	55.7 ± 3.7	26.8 ± 3.7	16.9 ± 0.7	0.6 ± 0.5
		Centre	58.1 ± 0.5	24.1 ± 0.1	17.5 ± 0.5	0.3 ± 0.1
		Average	56.9	25.5	17.2	0.4
	Second Phase	Edge	18.1 ± 4.2	65.4 ± 3.5	12.2 ± 0.7	4.3 ± 0.4
		Centre	13.7 ± 0.8	68.9 ± 1.0	12.4 ± 0.4	5.0 ± 0.3
		Average	15.9	67.2	12.3	4.6

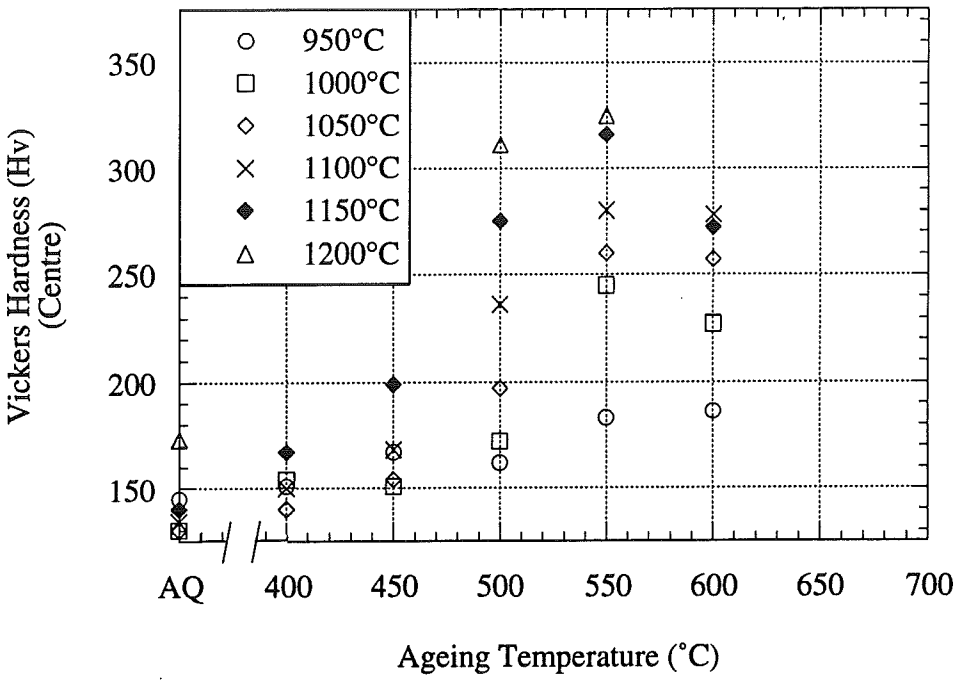

Figure 21. Hardness of the 69/30 alloy as a function of ageing temperature (ageing time 3 hours) for different temperatures of homogenisation (homogenisation time 30 minutes).

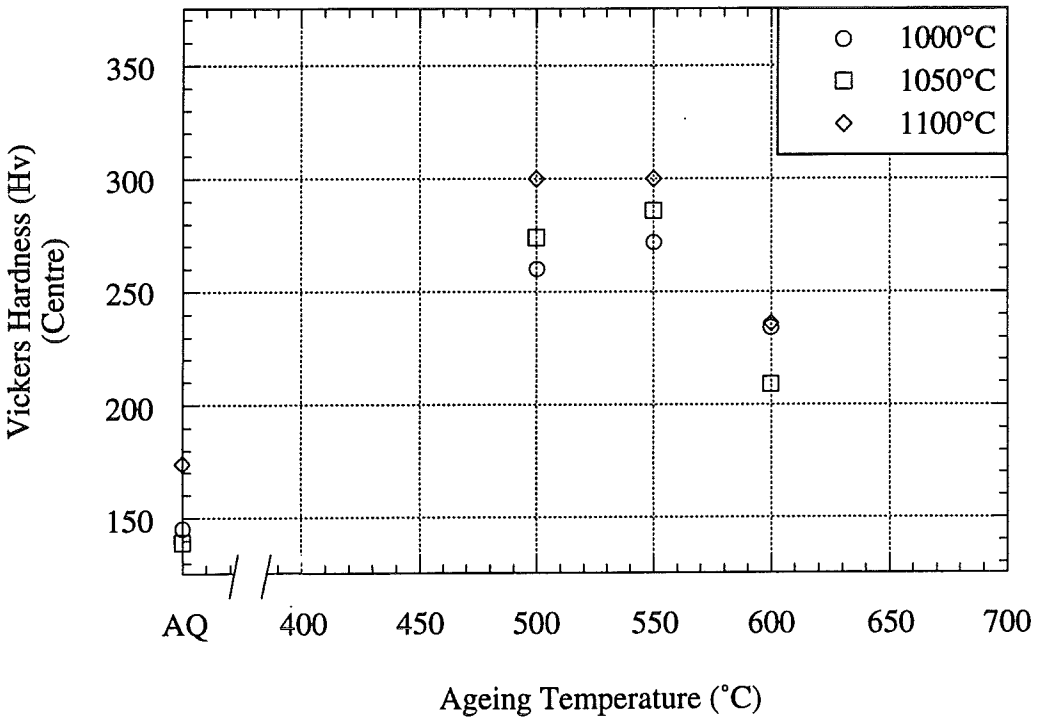

Figure 22. Hardness of the 59/40 alloy as a function of ageing temperature (ageing time 3 hours) for different temperatures of homogenisation (homogenisation time 30 minutes).

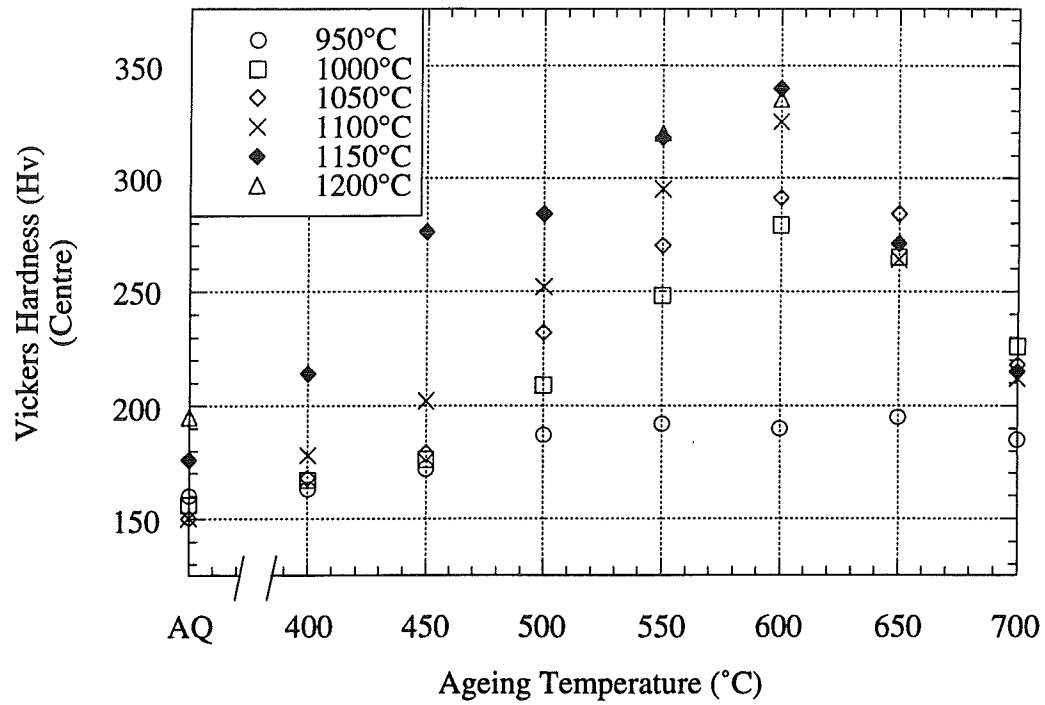

Figure 23. Hardness of the 54/27.5/17 alloy as a function of ageing temperature (ageing time 3 hours) for different temperatures of homogenisation (homogenisation time 30 minutes).

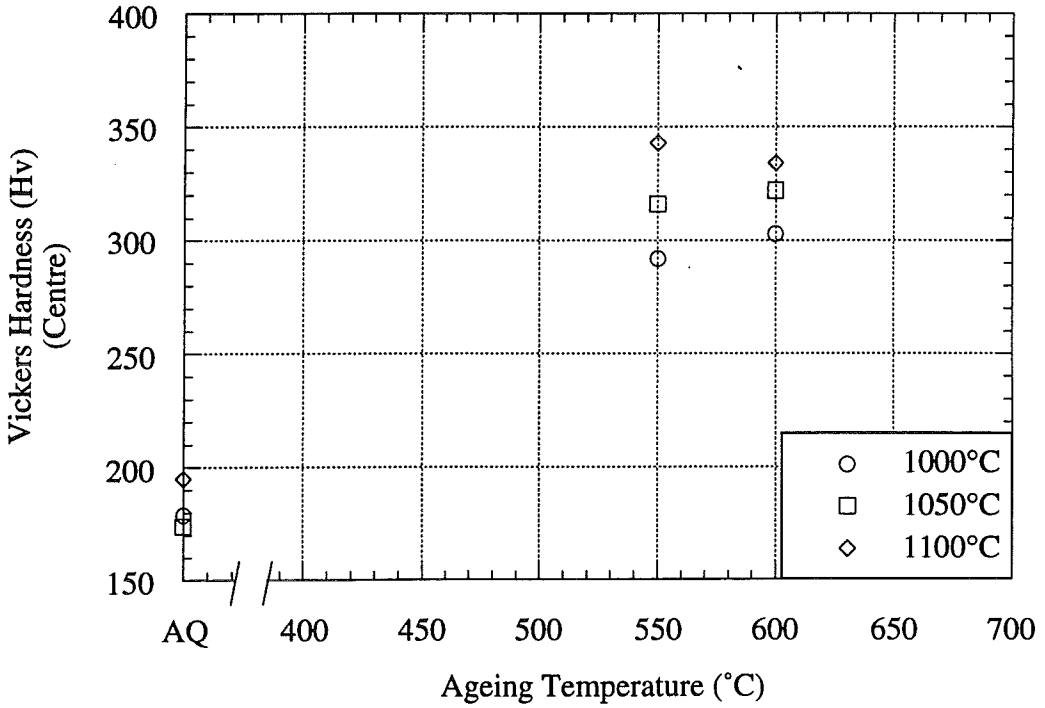

Figure 24. Hardness of the 44.5/37/17 alloy as a function of ageing temperature (ageing time 3 hours) for different temperatures of homogenisation (homogenisation time 30 minutes).

As a first estimate for the optimum combination of homogenisation and ageing treatment, it was chosen to homogenise for 30 minutes at 1100°C and to age for 3 hours at 550°C for the 69/30 alloy and at 600°C for the 54/27.5/17 alloy (see Table 2 and Figures 21 and 23).

The following observations can be made for the measured intervals:

1. For the 69/30 alloy: maximum hardness occurs after ageing at 550°C after homogenisation at 1200°C.
2. For the 59/40 alloy: maximum hardness occurs after ageing at 500°C and 550°C after homogenisation at 1100°C.
3. For the 54/27.5/17 alloy: maximum hardness occurs after ageing at 600°C after homogenisation at 1150°C and 1200°C.
4. For the 44.5/37/17 alloy: maximum hardness occurs after ageing at 550°C after homogenisation at 1100°C.

Further it is observed that the hardness after quenching (AQ) after homogenisation is nearly independent of homogenisation temperature, but the AQ hardness increased significantly after homogenisation at 1200°C for the 69/30 alloy, 1100°C for the 59/40 alloy, 1150°C and 1200°C for the 54/27.5/17 alloy and at 1100°C for the 44.5/37/17 alloy. Homogenisation at 950°C does not yield a significant ageing effect.

The hardness as a function of time of ageing at various ageing temperatures (400-700°C) for a fixed homogenisation temperature (as given in Table 2) is shown by Figures 25-28. In all cases hardnesses were determined in the centre of the specimen.

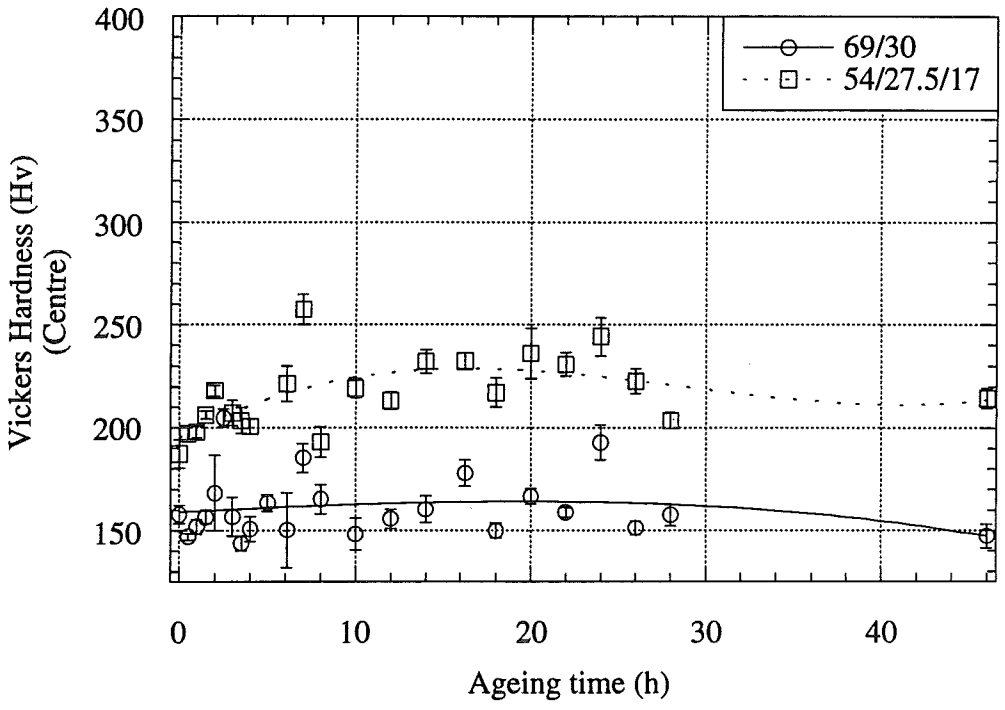

Figure 25. Hardness as a function of time of ageing at T=400°C after 30 minutes homogenisation at 1100°C.

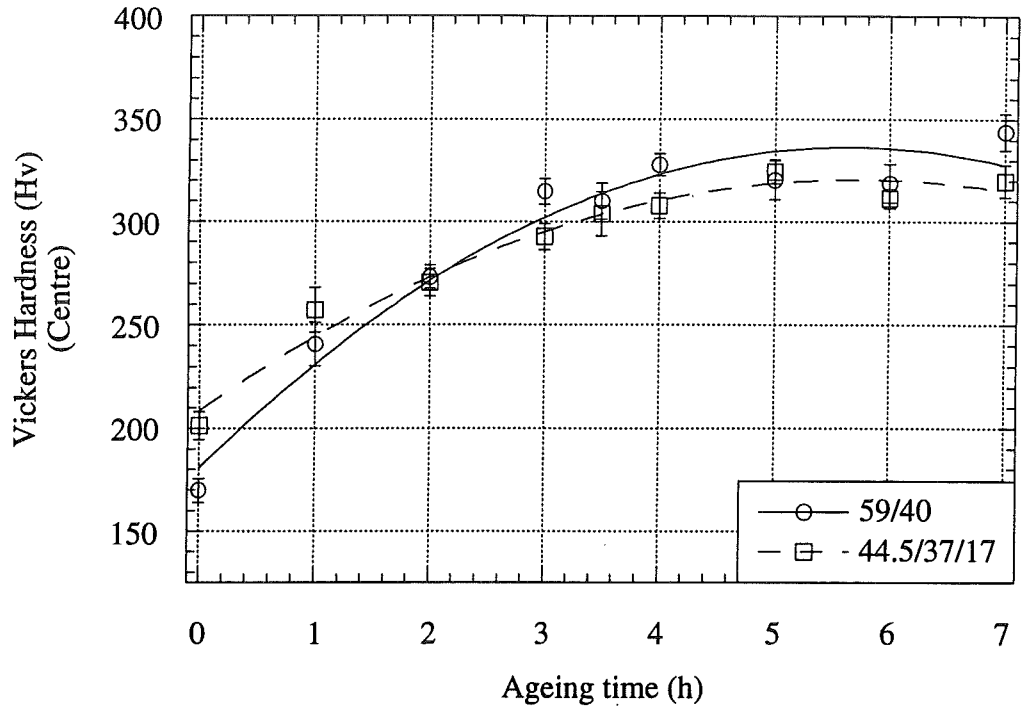

Figure 26. Hardness as a function of time of ageing at T=500°C after 30 minutes homogenisation at 1050°C (59/40) and 1100°C (44.5/37/17).

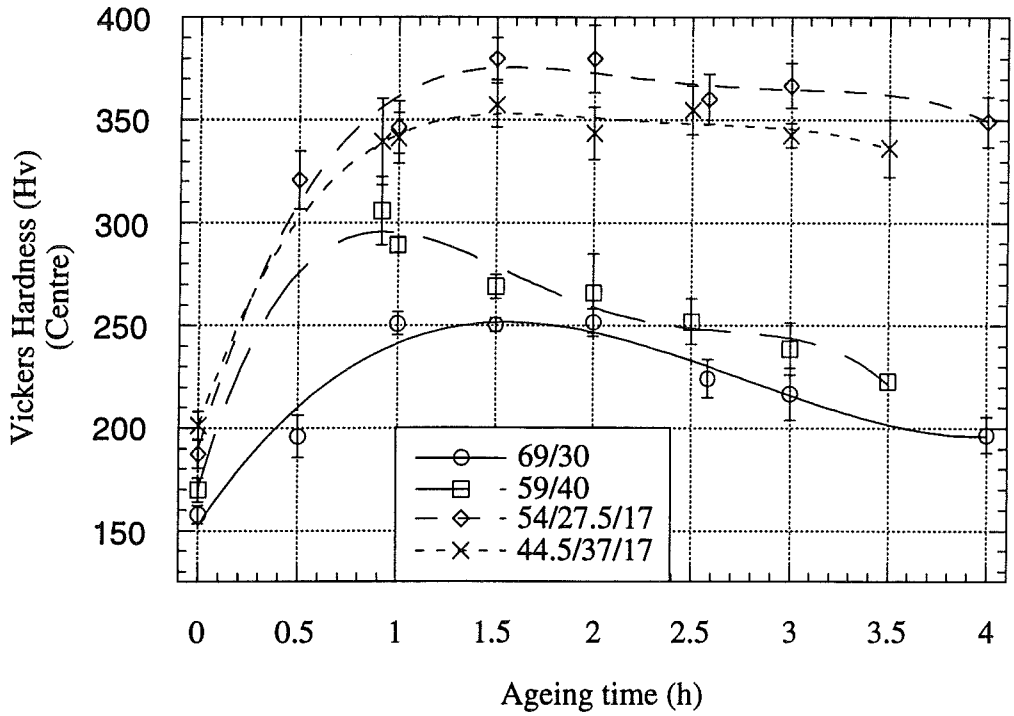

Figure 27. Hardness as a function of time of ageing at T=600°C after 30 minutes homogenisation at 1050°C (59/40) and 1100°C (others).

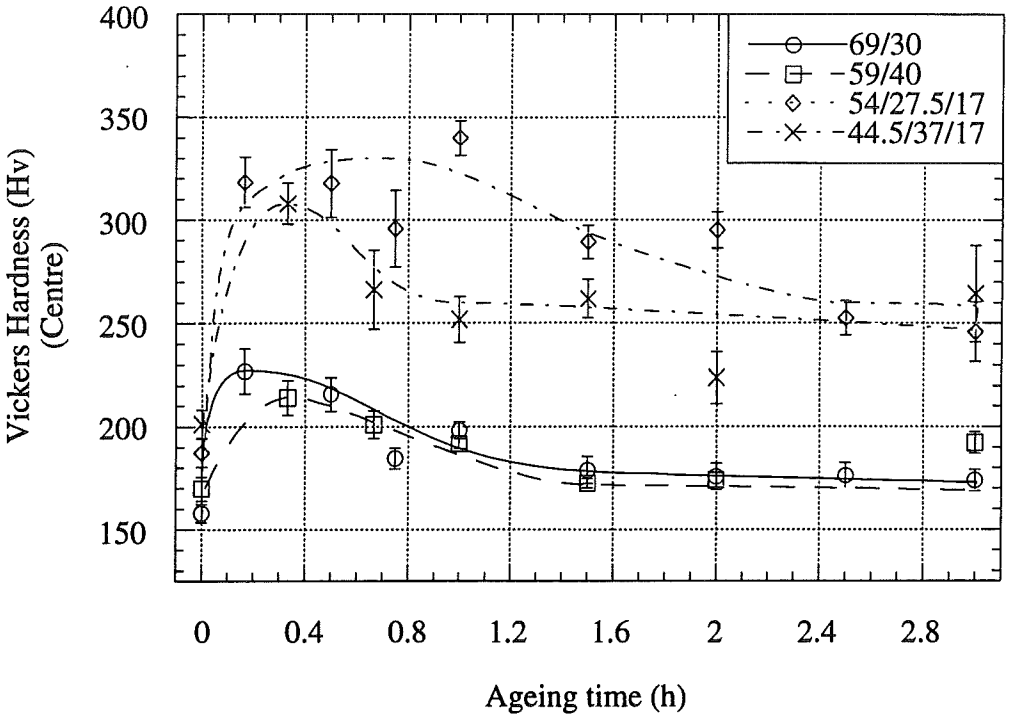

Figure 28. Hardness as a function of time of ageing at T=700°C after 30 minutes homogenisation at 1050°C (59/40) and 1100°C (others).

From Figures 25-28 the following observations can be made:

1. Ageing at 400°C does not yield a significant change of the hardness, but the hardness measured for this ageing temperature do show a large scatter (see Figure 25).
2. Ageing at 500°C results in a significant increase for both alloys measured. It is remarked that the hardness values for these alloys do not differ significantly (see Figure 26).
3. Ageing at 600°C yields drastic hardness changes. The highest level of hardness is reached for the 54/27.5/17 alloy. The hardness for the 54/27.5/17 and for the 44.5/37/17 alloys seem to reach a plateau, whereas (in order of decreasing value) for the 59/40 and for the 69/30 alloy maximum hardness values are observed, which are reached for 1 hour and 1.5 hours of ageing respectively.
4. Ageing at 700°C results again in large hardness changes. On ageing all alloys show distinguished hardness maximums (in order of decreasing value) for the 54/27.5/17, for the 44.5/37/17, for the 69/30 and for the 59/40 alloy. The respective ageing times of maximal hardness were 1 hour, 20 minutes, 20 minutes, and 10 minutes.

Comparing the isochronical ageing with the isothermal ageing for corresponding homogenisation temperatures the following observations can be made:

1. For the isochronical ageing, it holds that the maximum hardness for the 69/30 and 59/40 alloys occur after ageing for 3 hours at 550°C, whereas for the 54/27.5/17 and 44.5/37/17 alloys the maximum hardness after 3 hours ageing occurs respectively at 600°C and a temperature between 550°C and 600°C.
2. For the isothermal ageing it is found that for the 59/40 alloy the maximal hardness is found after about 6 hours of ageing at 500°C, whereas for the other alloys maximal hardness values occur after ageing at 600°C. For the latter temperature the maximal hardness decrease in the order 54/27.5/17, 44.5/37/17, 59/40, and 69/30.
3. For corresponding temperatures of homogenisation the quaternary alloys show higher maximum hardness values than the ternary alloys.

4.3. Homogenisation

The homogenisation heat treatment applied so far did not yield monophase alloys after quenching. As it is conceivable that for homogeneous supersaturated monophase alloys, subsequent ageing yields an advanced level of strength, possibilities of obtaining a homogeneous solid solution for the alloys studied were investigated by DTA in order to determine the temperature at which dissolution of the second phase starts. The dissolution of the second phase should result in an endothermic DTA peak as will do melting reactions. For all alloys the maximal temperature during DTA was 1350°C. The resulting DTA curves are given in Figures 29-32.
After the DTA run the 69/30 and 59/40 specimens used had become spherical, which was not the case with the 54/27.5/17 and 44.5/37/17 alloys. Clearly the endothermic effects observed for the 69/30 and for the 59/40 alloys reflect melting. For the 59/40 alloy two separate endothermic effects are observed. The effect at the higher temperature range is supposed to be related to melting. The lower temperature effect is hence supposed to be related to the dissolution of the second phase.
The endothermic effect observed for the 54/27.5/17 alloy clearly reflects solution of the second phase. For the 44.5/37/17 alloy no endothermic effect was observed at all between 1150 and 1350°C.

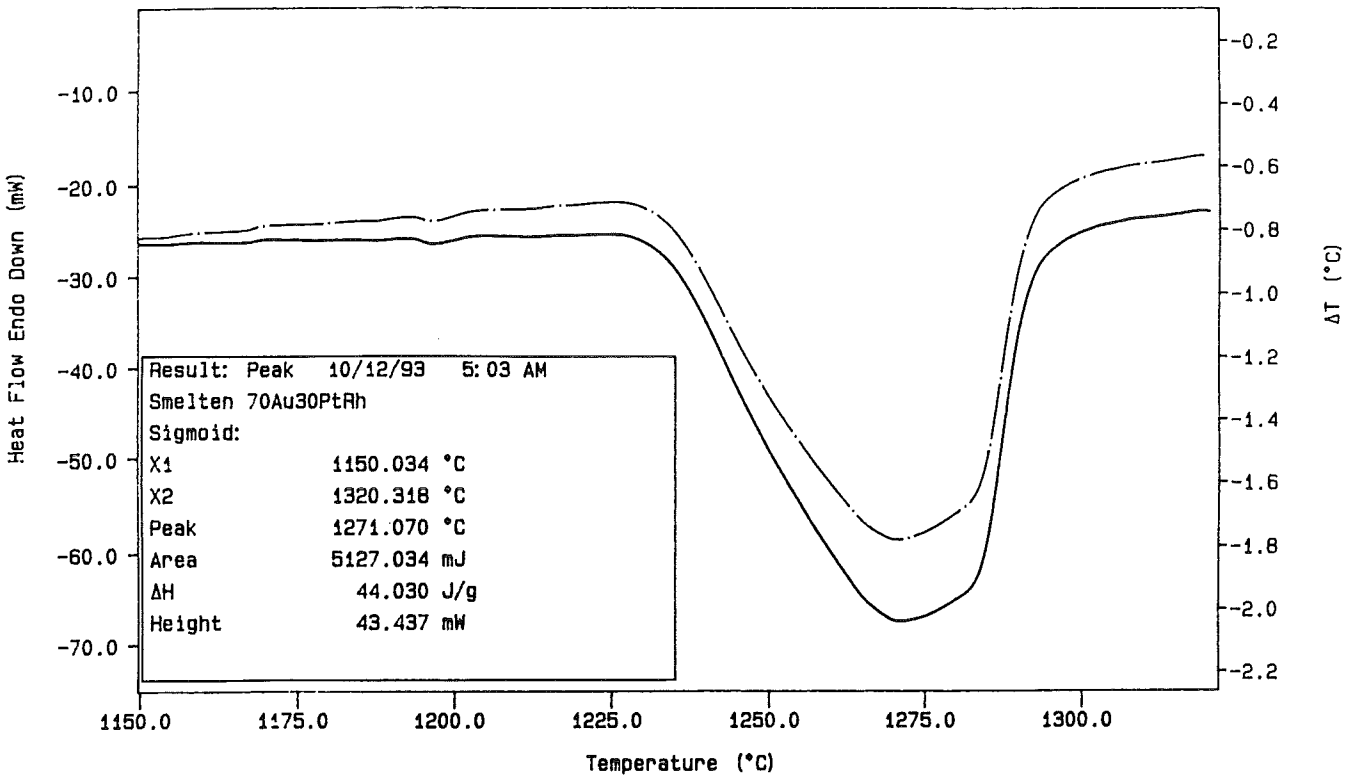

Figure 29. DTA curve of AuPtRh 69/30.

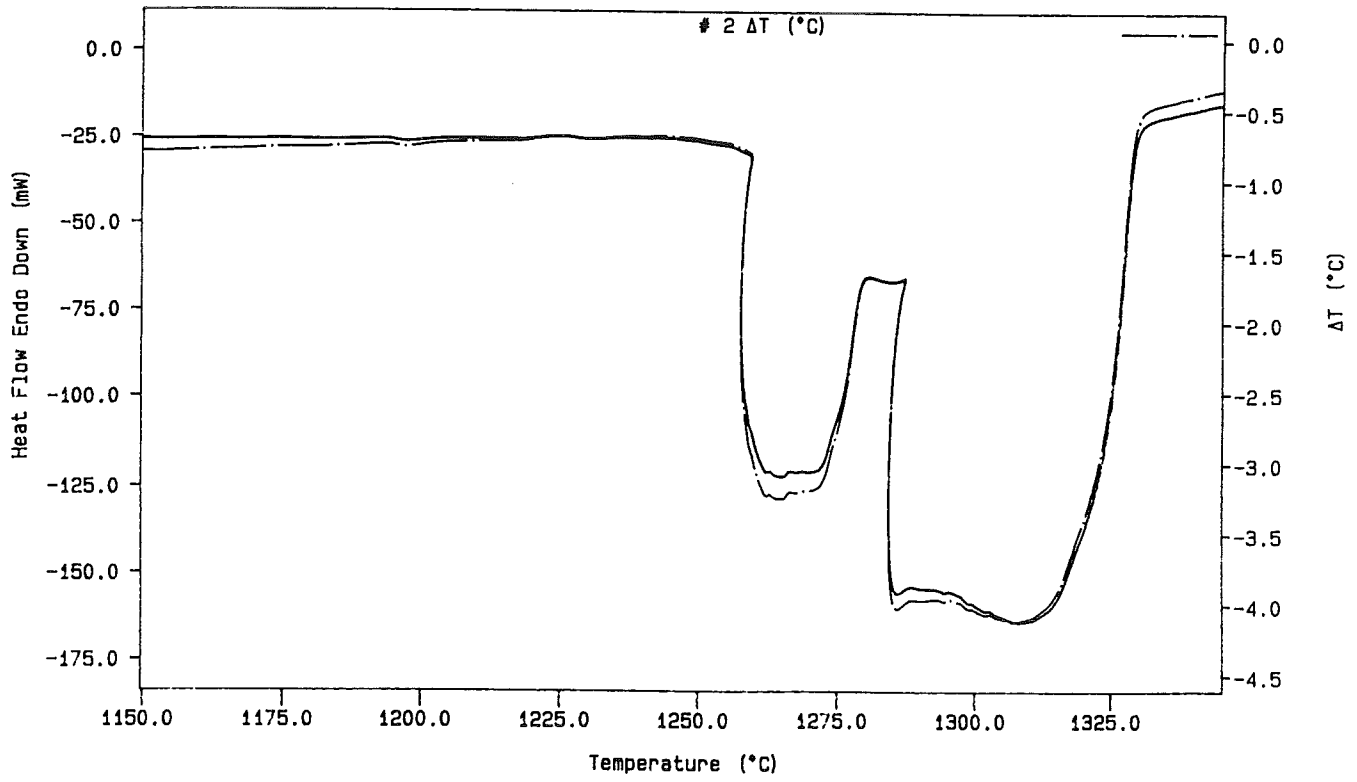

Figure 30. DTA curve of AuPtRh 59/40.

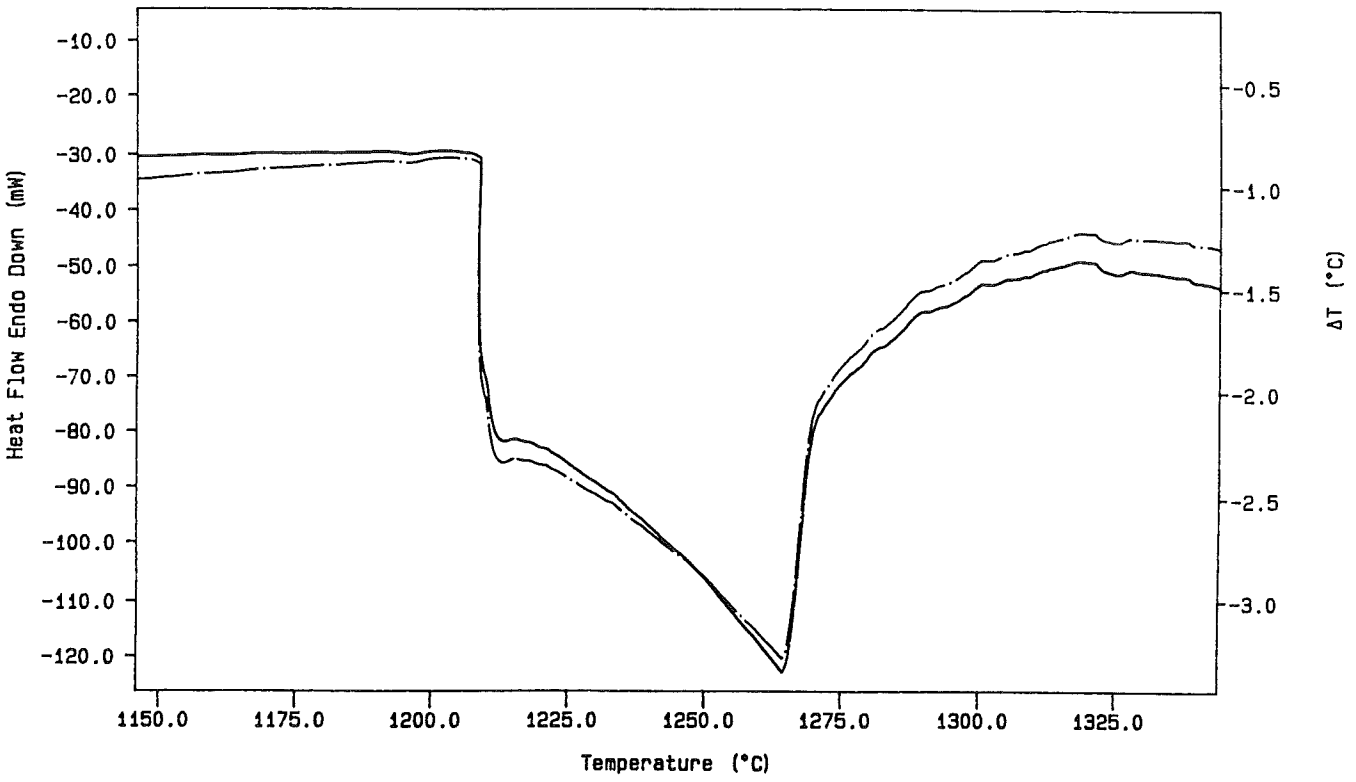

Figure 31. DTA curve of AuPtPdRh 54/27.5/17.

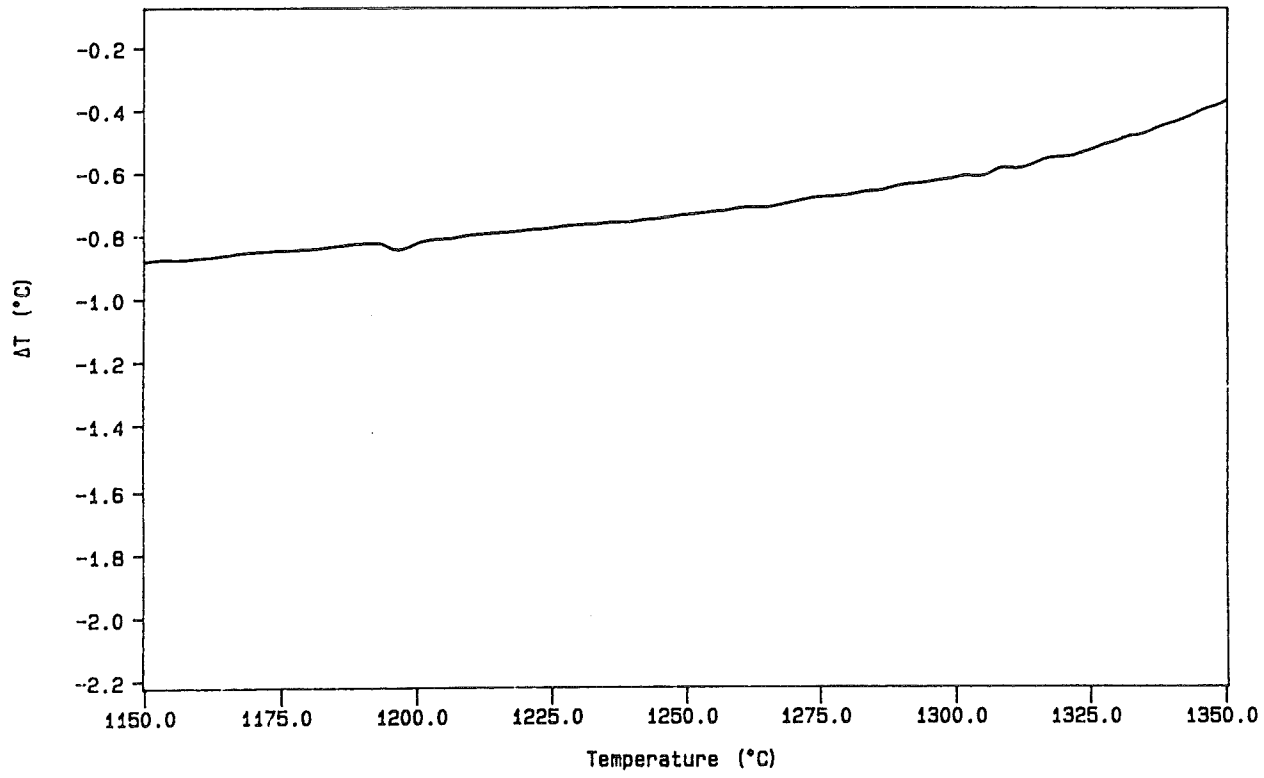

Figure 32. DTA curve of AuPtPdRh 44.5/37/17.

To investigate the possibilities of a solid solution homogenisation it was decided to explore the homogenisation treatments with homogenisation time and temperature as listed in Table 5. After the homogenisation the specimen was quenched in water. The relevant microscopical observations are summarised in Table 6. From Table 6 it can be seen that the 69/30 and the 59/40 alloys do show a second phase even after the highest homogenising temperature investigated. The 54/27.5/17 and the 44.5/37/17 alloys do show a monophase microstructure after homogenising at the highest investigated homogenising temperatures respectively 1350 and 1400°C.

Table 5. Time and temperature of homogenisation.

Alloy	Temperature (°C)	Time (hours)
69/30	1150	1, 2, 4, 8, 16, 30, 48, 90
	1200	1
	1250	1
	1300	1
59/40	1270	2, 4, 21
54/27.5/17	1150	1, 2, 4, 8, 16, 30, 48, 90
	1200	1
	1250	1
	1270	2, 4, 10
	1300	1
	1350	1
44.5/37/17	1400	1
	1400+1425	1+1

Table 6. Microscopical observations after homogenisation and quenching.

Alloy	Temperature (°C)	Time (hours)	Figure	Observation
69/30	1250	1	33	two phases
	1300	1	34	three phases
59/40	1270	21	35	two phases
54/27.5/17	1270	10	36	two phases
	1300	1	37	one phase
	1350	1	38	one phase
44.5/37/17	1400	1	39	one phase

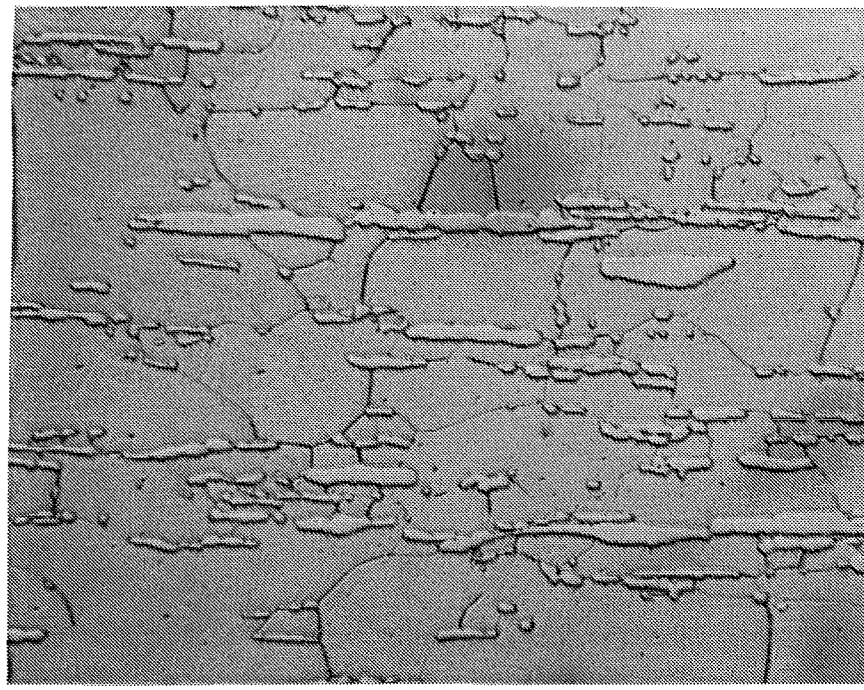

Figure 33. AuPtRh 69/30 after a heat treatment of 1 hour at T=1250°C, 1000x BF.

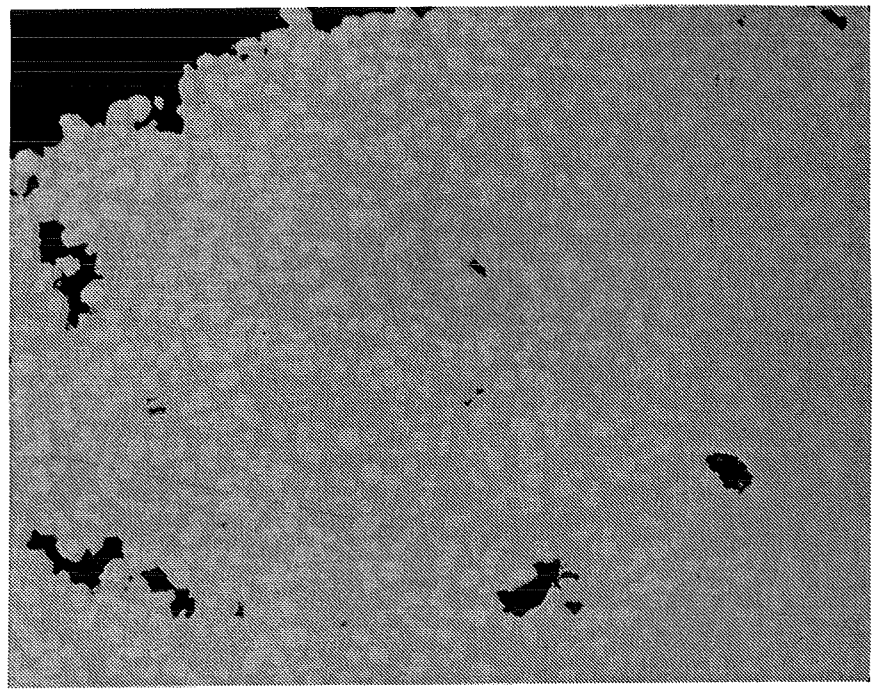

Figure 34. AuPtRh 69/30 after a heat treatment of 1 hour at T=1300°C, 100x BF.

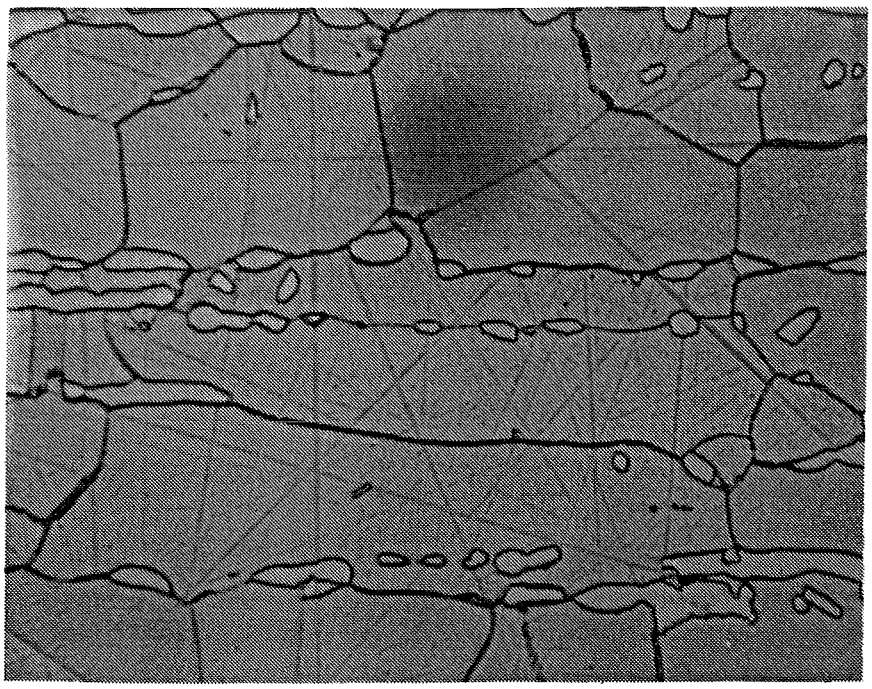

Figure 35. AuPtRh 59/40 after a heat treatment of 21 hours at T=1270°C, 1000x BF.

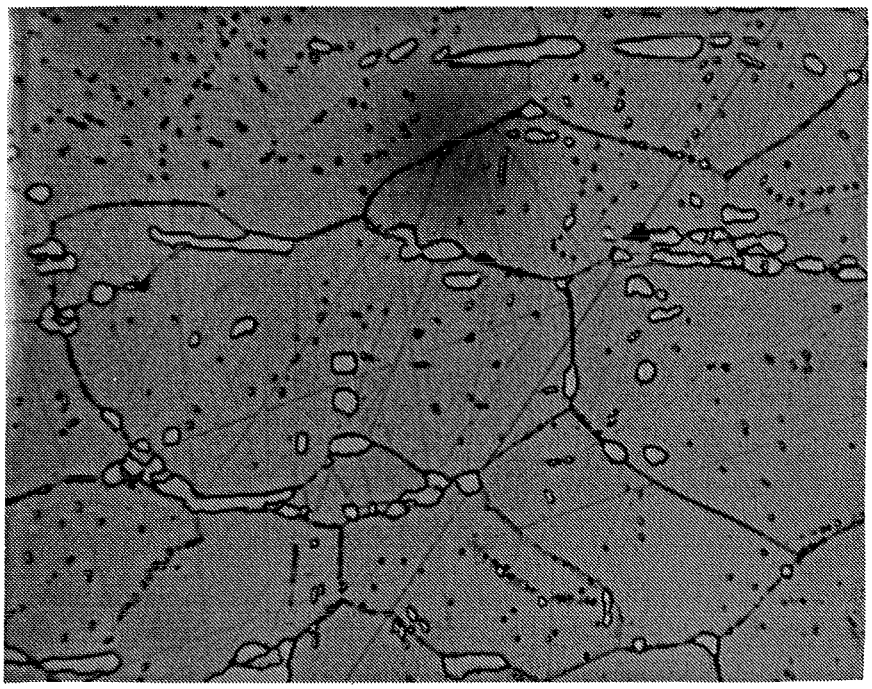

Figure 36. AuPtPdRh 54/27.5/17 after a heat treatment of 10 hours at T=1270°C, 1000x BF.

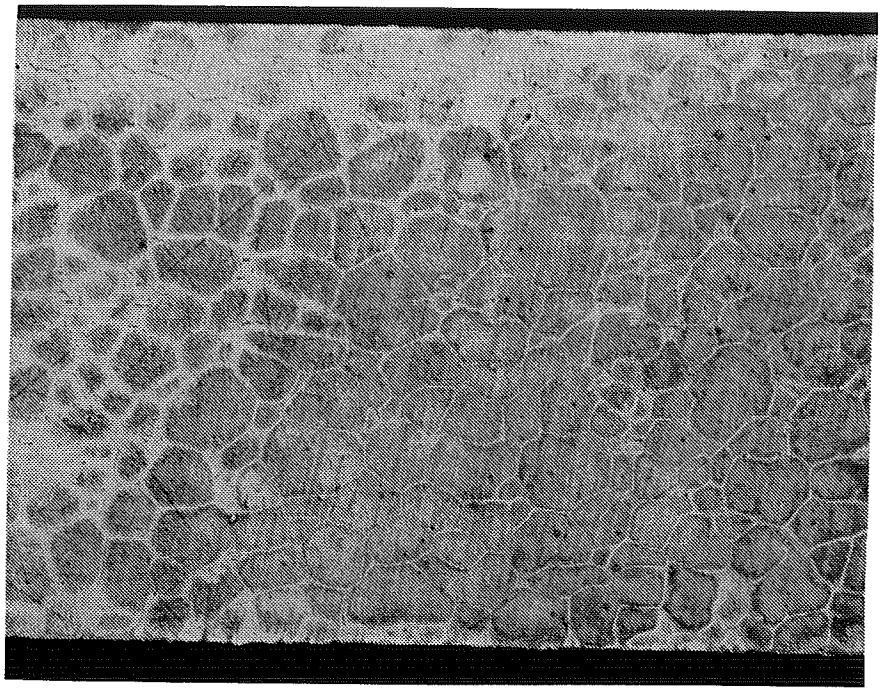

Figure 37. AuPtPdRh 54/27.5/17 after a heat treatment of 1 hour at T=1300°C, 100x BF.

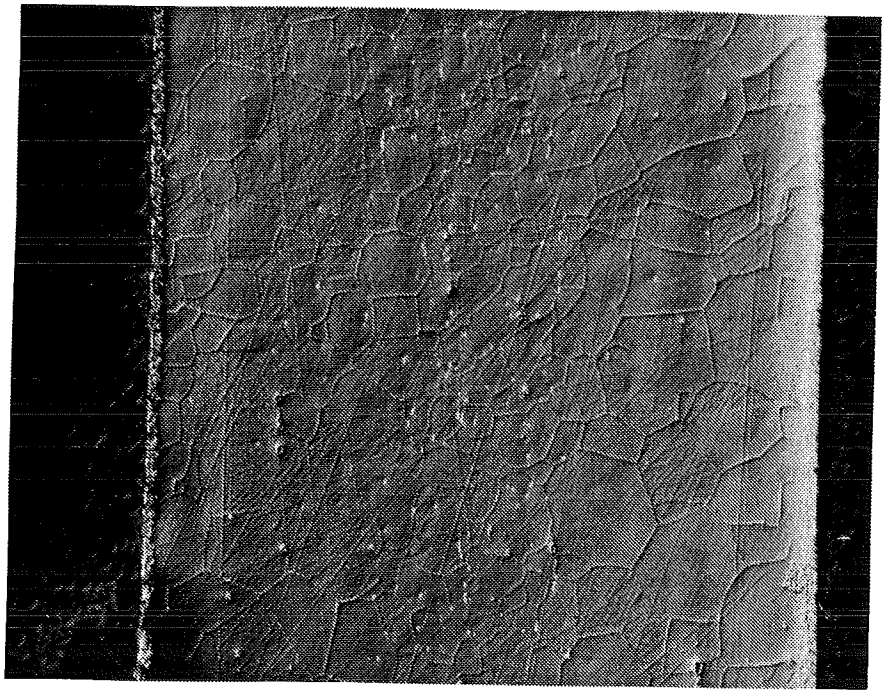

Figure 38. AuPtPdRh 54/27.5/17 after a heat treatment of 1 hour at T=1350°C, 100x DIC.

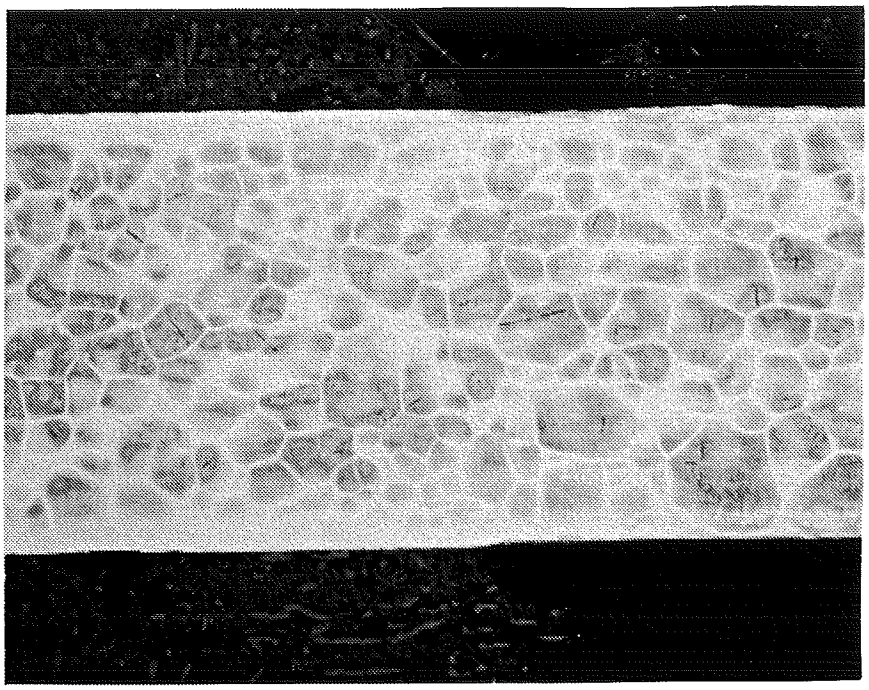

Figure 39. AuPtPdRh 44.5/37/17 after a heat treatment of 1 hour at T=1400°C, 100x BF.

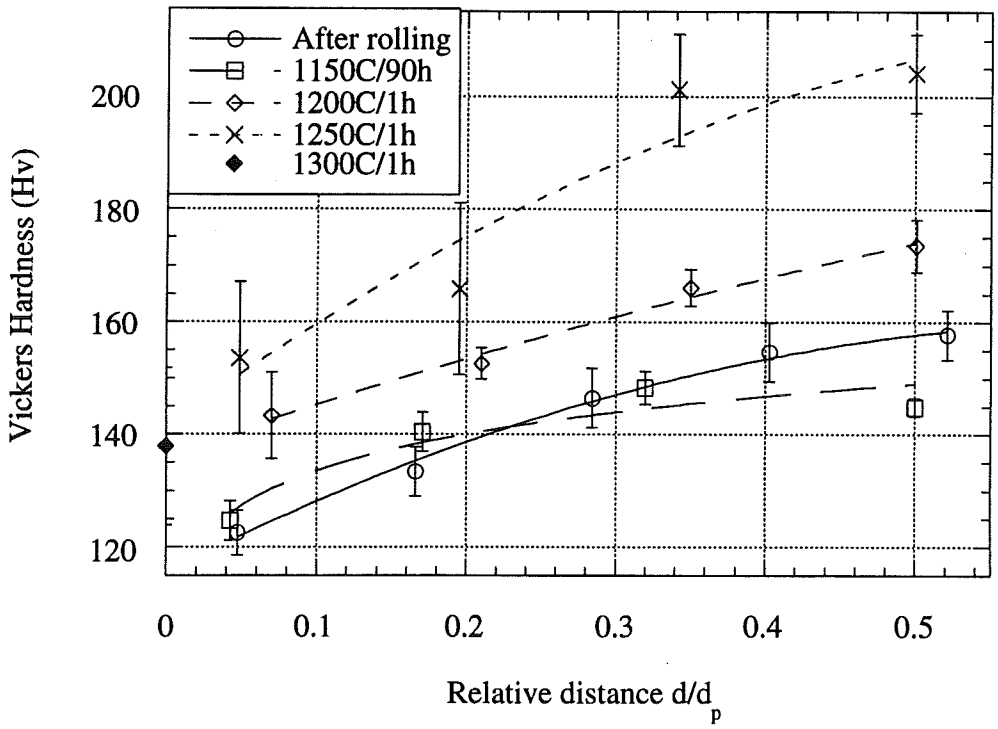

Figure 40. Hardness as a function of relative distance for different heat treatments of AuPtRh 69/30.

The homogenisation investigation was accompanied by hardness measurements as a function of the preceding homogenisation treatment for the 69/30 and 54/27.5/17 alloys. The results are given in Figures 40 and 41. The hardness as a function of the preceding homogenisation treatment for the 69/30 and 54/27.5/17 alloys show a difference. Figure 40 shows a slight increase in hardness for the 69/30 alloy and a sharpening of the profile with increasing temperature. Figure 41 shows for the 54/27.5/17 case an initial hardness loss after a heat treatment of 90 hours at 1150°C and for 1200°C the same slight increase in hardness as was found in the 69/30 case. Above 1200°C the hardness of the 54/27.5/17 increases strongly, the Vickers hardness doubles.

For the AuPtPdRh alloys the hardness in the centre as a function of the preceding homogenisation treatment is given in Figure 42. For the 1 hour homogenisation treatments of the 54/27.5/17 alloy the centre hardness is presented along with the result for the AuPtPdRh 44.5/37/17 alloy for comparison.

As can be seen from Figure 42 the rise in hardness with temperature is sharp from about 1200°C. The maximum hardness attained after homogenisation and quenching of the 54/27.5/17 and 44.5/37/17 alloy is about 400 HV.

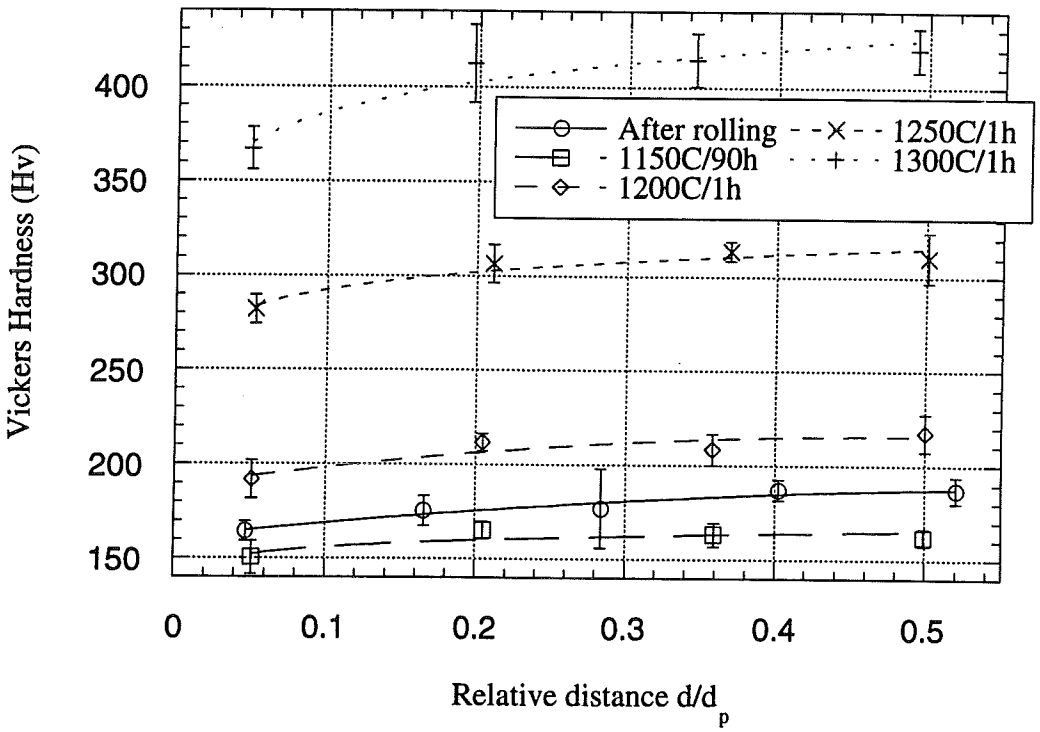

Figure 41. Hardness as a function of relative distance for different heat treatments of AuPtPdRh 54/27.5/17.

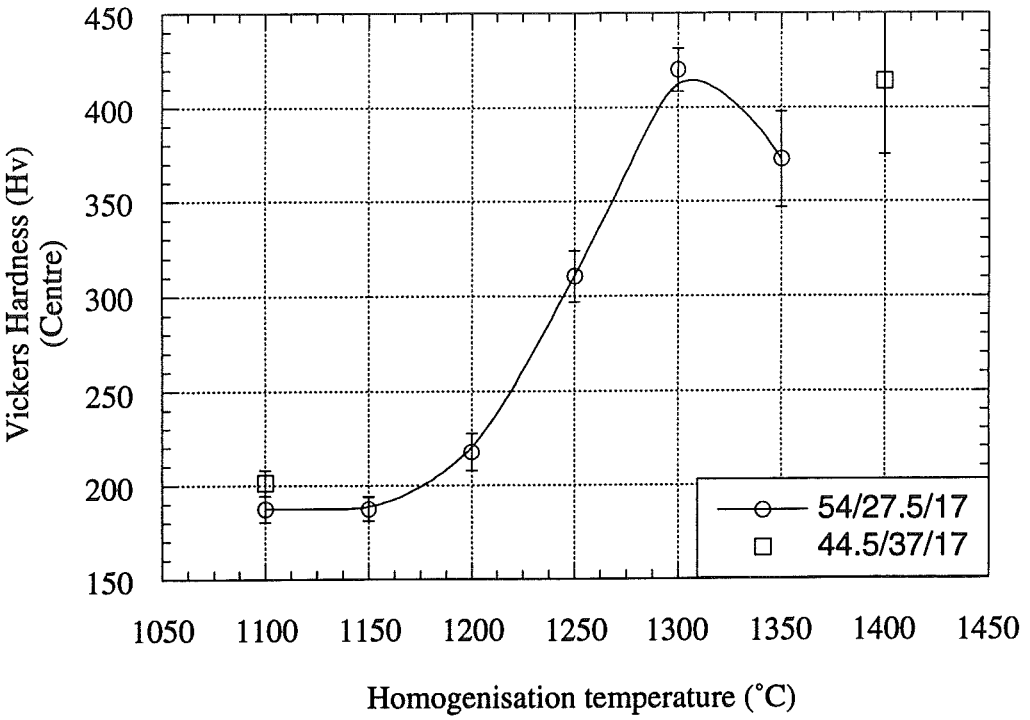

Figure 42. Hardness in the centre after 1 hour of homogenisation at temperatures indicated: AuPtPdRh 54/27.5/17 and 44.5/37/17.

4.4. Hardness on ageing after homogenisation

Ageing from a homogeneous supersaturated monophase alloy can be studied for the AuPtPdRh alloys (see Table 6). After 1 hour homogenisation of the 54/27.5/17 alloy at 1350°C and of the 44.5/37/17 alloy at 1400°C, these alloys were aged for various times and temperatures. The hardness of these alloys as a function of ageing time and temperature are shown in Figures 43-45.

The following observations can be made:

1. On ageing from a supersaturated monophase state the hardness of the 44.5/37/17 alloy is always higher than the 54/27.5/17 alloy.
2. For the 44.5/37/17 alloy the hardness is maximal on ageing at 600°C, whereas for the 54/27.5/17 alloy maximal hardness is reached on ageing at 500°C.

It is observed that the increase of homogenisation temperature implies a large increase of the hardness after homogenisation/quenching and embedding. The embedding as such represents a small heat treatment. The effect of this heat treatment will be larger the more supersaturated the alloy was before embedding. The hardness increase due to embedding was measured for the 54/27.5/17 alloy by measurement of the surface hardness of a homogenised and quenched specimen before and after embedding. The result was that the hardness increased from 331±40 HV to 386±8 HV.

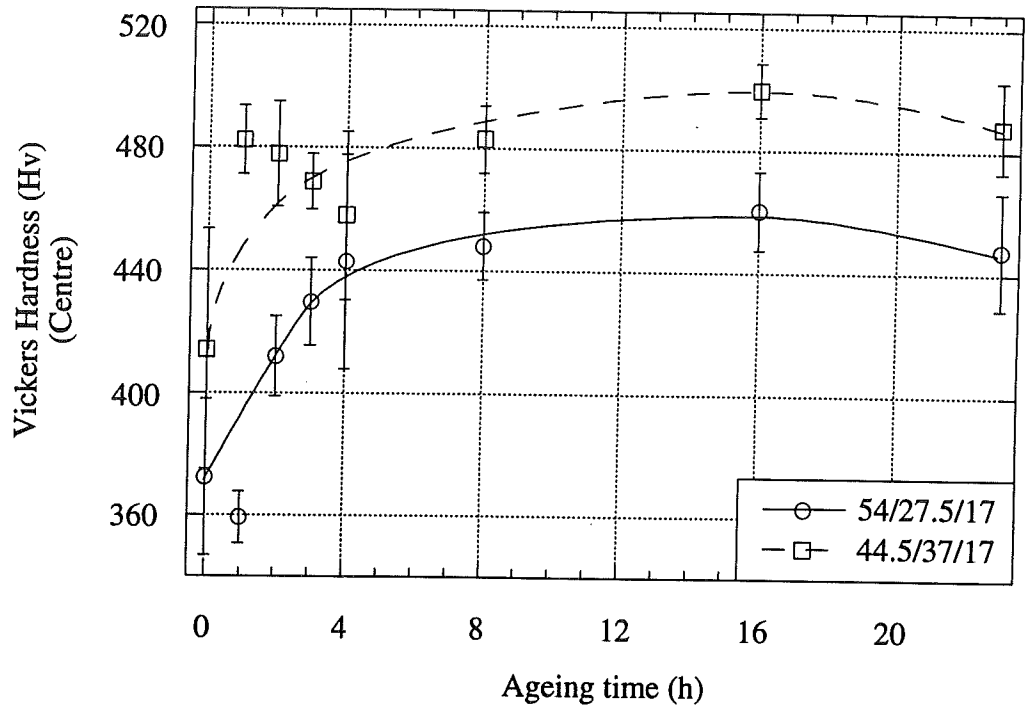

Figure 43. Hardness as a function of time of ageing at T=500°C after homogenisation.

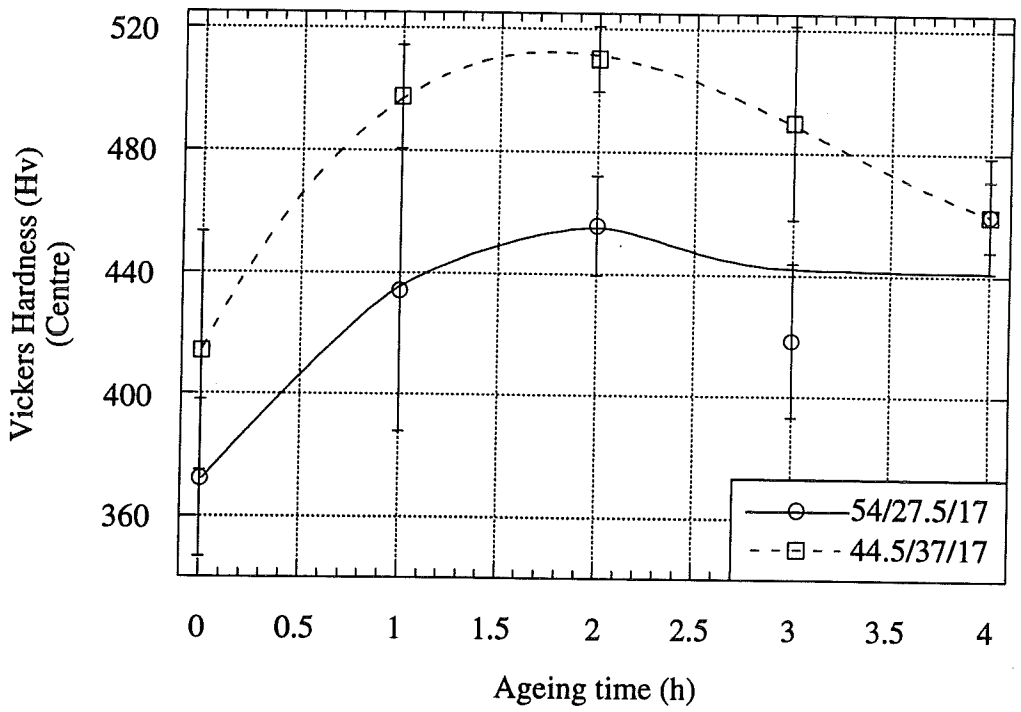

Figure 44. Hardness as a function of time of ageing at T=600°C after homogenisation.

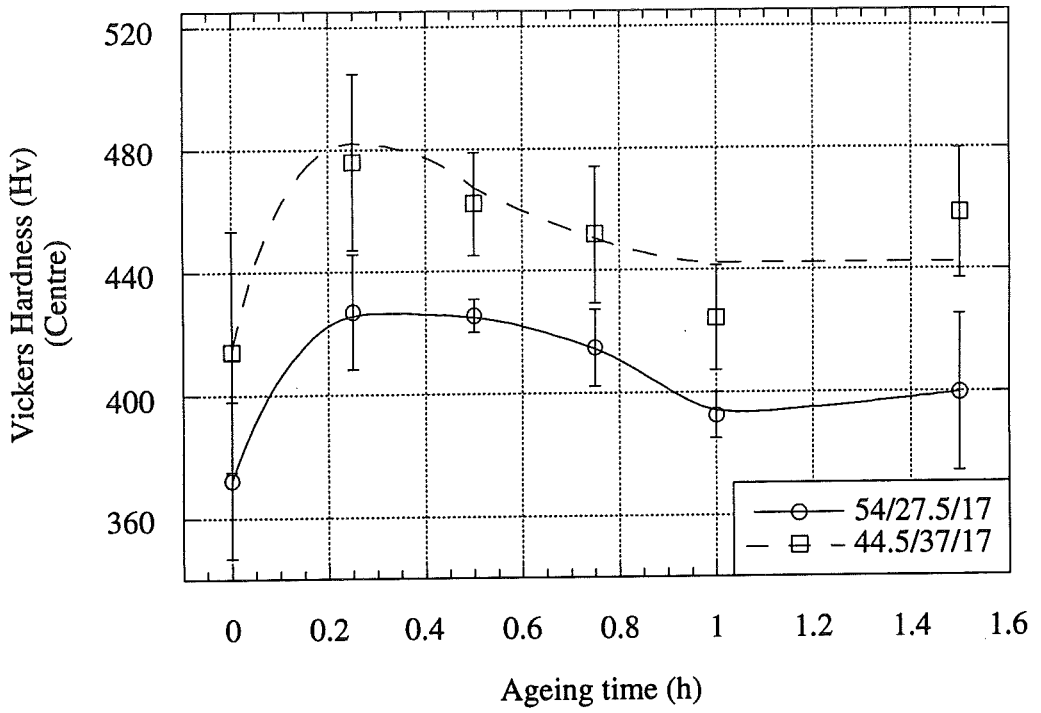

Figure 45. Hardness as a function of time of ageing at T=700°C after homogenisation.

4.5. Tensile testing

From earlier investigations [1,21], some data were available about the mechanical properties of the alloys studied after rolling and homogenisation at 1050-1100°C and after ageing from a two phase condition. The condition after rolling, homogenisation at 1050-1100°C, and quenching is denoted as AQ (After Quenching). The results are given in Table 7.

The foregoing §4.4 showed a way of optimising the hardness of the alloys, by subsequent homogenisation and ageing. These 'optimising' treatments were applied to specimens which were in turn subjected to a tensile test. The treatments applied on the specimens and the results are given in Table 8. The specimens of the 54/27.5/17 alloy were from a different batch than the batch used in the previous sections. Furthermore, the 54/27.5/17 alloy was investigated with two different plate thicknesses: 0.6 and 0.8 mm thickness. This was done to verify the influence of the plate thickness on the mechanical properties.

Table 7. Mechanical properties of the alloys studied after rolling and homogenisation at 1050-1100°C and after ageing [1,21]: yield stress σ_y, ultimate tensile stress σ_{uts}, and strain at fracture ε_f.

Alloy	Condition	σ_y (MPa)	σ_{uts} (MPa)	ε_f (%)
69/30	AQ	235	424	36.7
	AQ, 3h 550°C	818	987	17.8
59/40	AQ, 3h 550°C	928	991	3.5
54/27.5/17	AQ	354	530	22.0
	AQ, 3h 600°C	986	1193	9.5
44.5/37/17	AQ, 3h 600°C	1041	1109	2.1

As examples of the stress-strain curves Figures 46 and 47 are given. These Figures show the four typical stress-strain curves for the 0.6 mm thickness for the 44.5/37/17 alloy and the 54/27.5/17 alloy respectively. The influence of the plate thickness is, as can be seen, not significant. It is seen from Table 8 that for the 44.5/37/17 alloy the duplications after homogenisation at 1400°C are significantly different with a difference in σ_{uts} of 220 MPa, and the same applies after subsequent ageing with a difference in σ_{uts} of 260 MPa.

Table 8. Applied treatments for the tensile test specimens and results, with yield stress σ_y, ultimate tensile stress σ_{uts}, strain at fracture ε_f, and strain hardening coefficient n.

Alloy	Condition	σ_y (MPa)	σ_{uts} (MPa)	ε_f (%)	n
44.5/37/17 (0.6 mm thickness)	AQ	470	625	23.7	0.18
	AQ, 3h 550°C	940	1033	18.9	0.11
		949	1045	20.7	0.12
	AQ, 1h 1400°C		512	0.1	
			734	0.1	
	AQ, 1h 1400°C, 2h 600°C	1014	1014	0.0	
			747	0.3	
54/27.5/17 (0.8 mm thickness)	AQ	387	545	23.1	0.23
	AQ, 3h 600°C	870	1000	13.1	0.12
		863	986	13.7	0.12
	AQ, 1h 1350°C	680	884	7.4	0.11
		682	864	7.6	0.12
	AQ, 1h 1350°C, 1h 600°C	1050	1074	1.1	
	AQ, 1h 1350°C, 2h 600°C		978	0.3	
		1066	1103	1.2	
	AQ, 1h 1350°C, 3h 600°C	1070	1121	1.1	
	AQ, 1h 1350°C, 4h 600°C	1035	1145	1.4	0.14
54/27.5/17 (0.6 mm thickness)	AQ	397	542	21.1	0.22
	AQ, 3h 600°C	789	933	14.3	0.12
		806	918	12.5	0.12
	AQ, 1h 1350°C	614	778	7.2	0.13
		621	832	9.1	0.13
	AQ, 1h 1350°C, 1h 600°C		1002	0.8	
	AQ, 1h 1350°C, 2h 600°C		973	0.6	
			974	0.8	
	AQ, 1h 1350°C, 3h 600°C		931	0.8	
	AQ, 1h 1350°C, 4h 600°C	986	1142	1.1	0.12

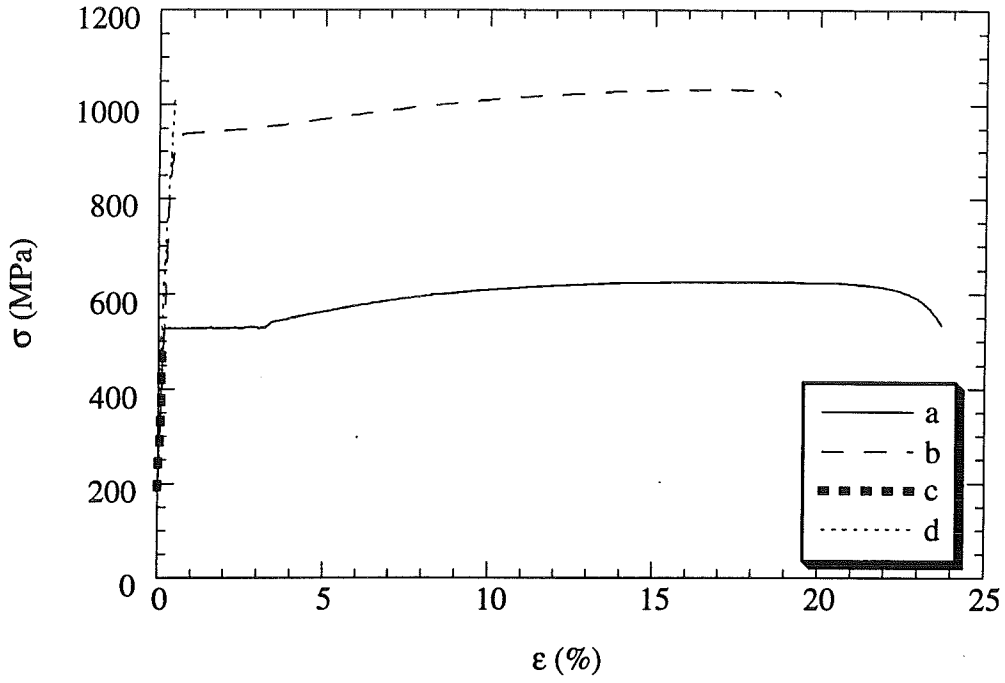

Figure 46. Stress-strain curves for the 44.5/37/17 alloy after: AQ (a), AQ and 3h 550°C (b), AQ and 1h 1400°C (c), and AQ, 1h 1400°C and 2h 600°C (d).

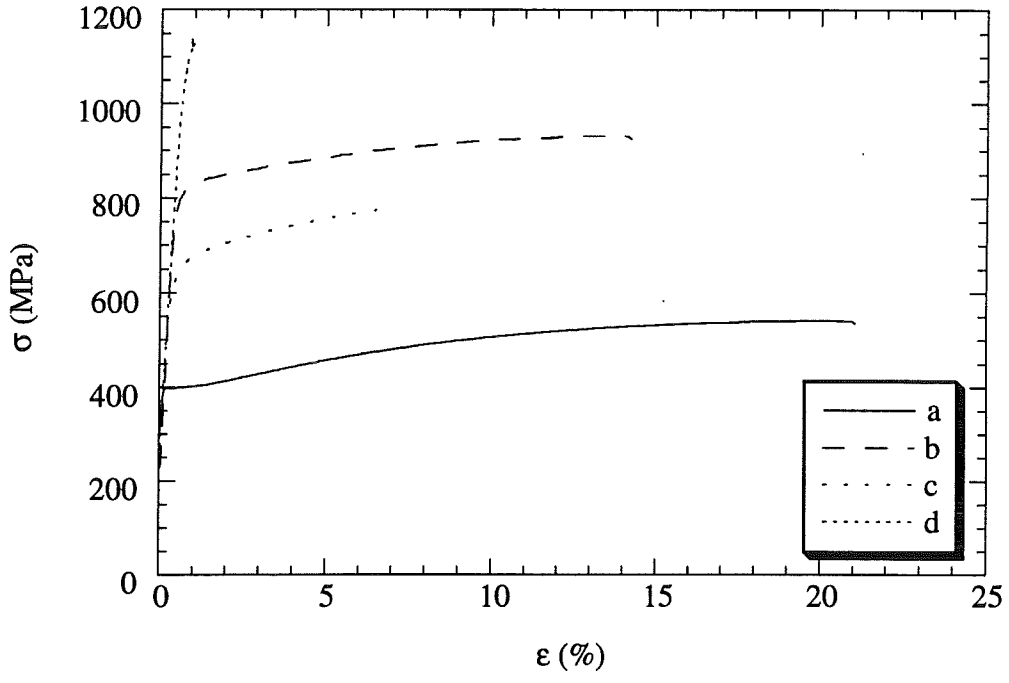

Figure 47. Stress-strain curves for the 54/27.5/17 alloy after: AQ (a), AQ and 3h 600°C (b), AQ and 1h 1350°C (c), and AQ, 1h 1350°C and 4h 600°C (d).

Figures 46 and 47 clearly illustrate the increase in yield stress and the strong decrease of the fracture strain for the alloy after homogenisation compared with the specimen after rolling and homogenisation at 1100°C. The subsequent ageing even enlarges these differences when compared with the after rolling and homogenisation at 1100°C and ageing specimen.
The tensile test specimens were embedded and prepared for microscopic investigation. The specimens after rolling and homogenisation at 1100°C and those after ageing, show considerable plastic deformation and tough fracture. The specimens which were homogenised and those after subsequent homogenisation and ageing, show little plastic deformation and brittle fracture. This brittle fracture proved to be of an intercrystalline type, as can be seen from Figure 48. Although, the specimen shown is one of the specimens which were precipitated after homogenisation, the same kind of fracture was found in the homogenised specimens. In Figure 48 it should be noted that some plastic deformation was present in the grains near the fracture, as can be seen from the slip (and cross-slip) lines.
The specimen which was the most brittle, is shown in Figure 49. This specimen shows clearly, that not only in and near the fracture the grain boundaries have been separated, but throughout the specimen cracks (the thick black lines) have formed in between grain boundaries.

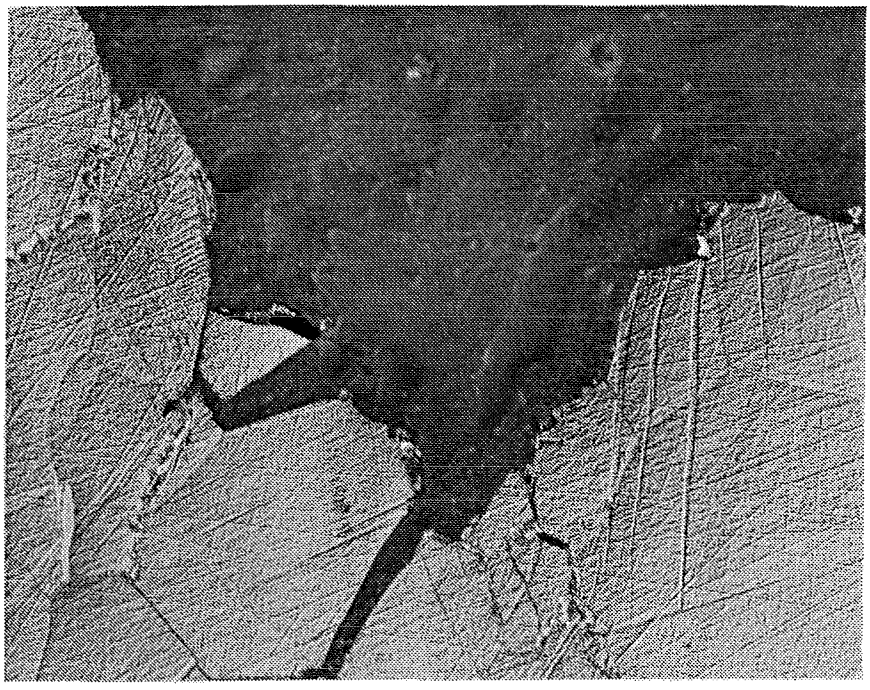

Figure 48. Microscopic photograph of the 54/27.5/17 alloy. Specimen AQ has been homogenised for 1 hour at 1350°C and has been precipitated for 4 hours at 600°C, 500x DIC.

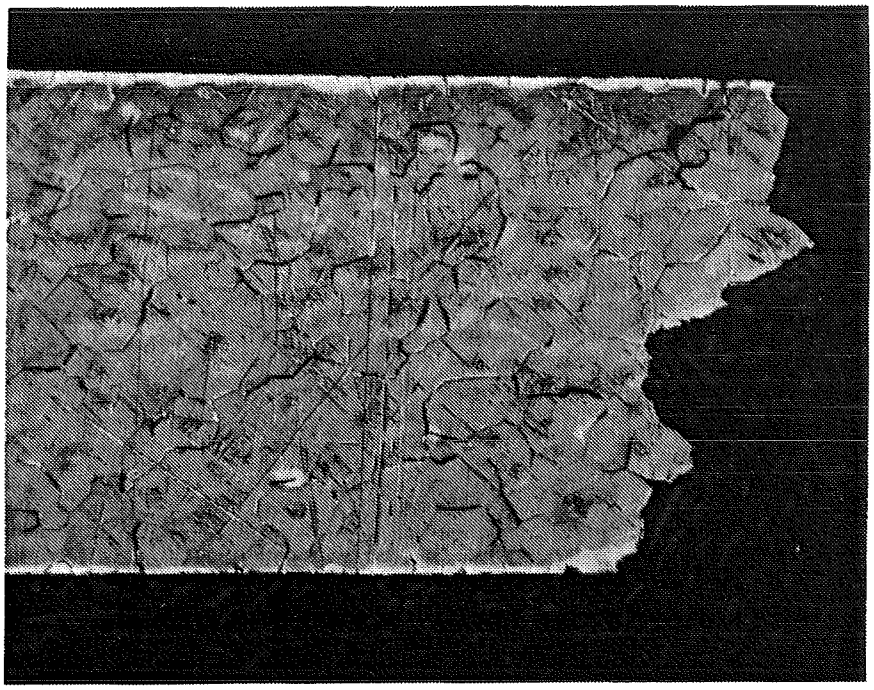

Figure 49. Microscopic photograph of the 44.5/37/17 alloy. Specimen AQ has been homogenised for 1 hour at 1400°C and has been precipitated for 2 hours at 600°C, 100x DIC.

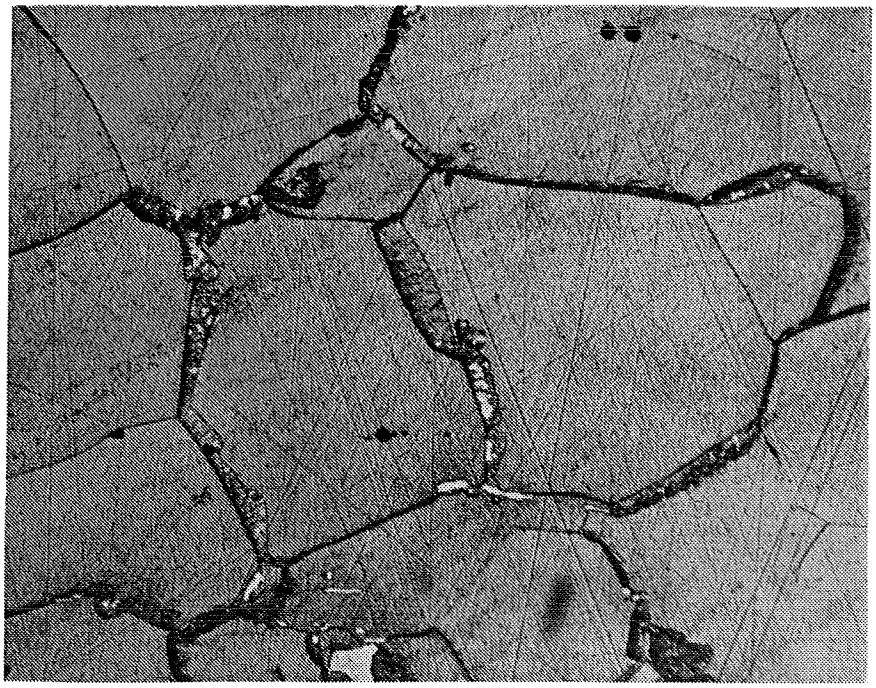

Figure 50. Microscopic photograph of the 54/27.5/17 alloy. Specimen AQ has been homogenised for 1 hour at 1350°C and has been precipitated for 4 hours at 600°C, 500x OI DIC.

In Figure 50, a 54/27.5/17 specimen (AQ, 1h 1350°C, 4h 600°C) is shown at the centre of the plate away from the fracture. From Figure 50 it is apparent that at least some of the precipitation was discontinuous, i.e. some second phase particles have precipitated on the grain boundaries and have grown. The two phases were microanalysed (EDAX) giving the chemical composition of the grain and second phase particle to be respectively AuPtPdRh 53.5/27.3/17.5/1.7 at. % and AuPtPdRh 23.8/66.6/5.1/4.5 at. % [21].

A homogenised state is shown in Figure 51, where the grain boundaries are apparent and inside the grains the sub boundaries can be seen. The grain growth due to homogenisation is apparent. It should be noted that the centre of the grain is more etched (deeper) than the material in the vicinity of the grain boundaries and that on the grain boundaries particles are present.

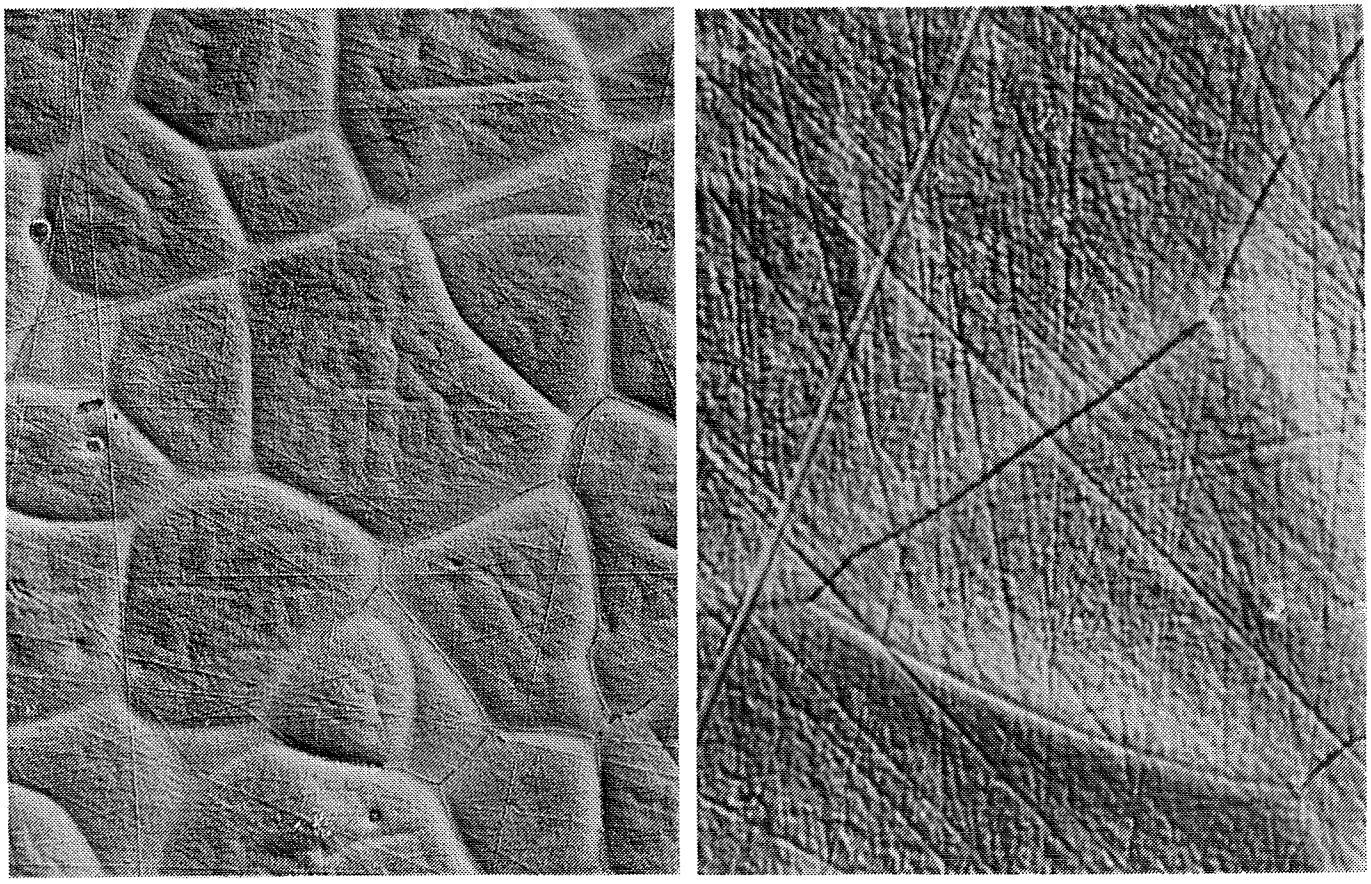

Figure 51. Microscopic photographs of the 44.5/37/17 alloy. Specimen AQ has been homogenised for 1 hour at 1400°C, left 500x DIC and right 2000x OI DIC.

5. Discussion

5.1. Introduction

Precipitation involves decomposition of a supersaturated phase by transport of, in origin, solute atoms [7,8]. It is generally supposed that the effect of precipitation on the mechanical properties can be maximised by starting the decomposition from a monophase condition of the alloy concerned (see also §1.1 and §2.3). In this chapter the results of the determinations of the temperatures limiting the monophase regions for the alloys studied will be discussed firstly. Homogenisation was followed by ageing. The processes occurring during ageing result in hardness changes and changes in mechanical properties. The variation in mechanical properties will be discussed from two points of view: the kinetics of the underlying metallurgical transformations and the comparison between the expected values for the mechanical properties and the ones predicted by the theory treated in chapter 2.

5.2. Homogenisation and phase boundaries

For the present discussion it is assumed that for the alloys studied no intermetallic compounds ~~form~~ have formed. This is justified, because as far as it is known, no intermetallic compounds can expected to be present for the compositions studied [3,4,5]. Hence, all alloys (excluding partial melting) are present only in a dual-phase or a monophase condition. The dual-phase condition concerns an Au-rich phase, the matrix, and a Pt-rich phase, the second phase.

The starting point for the homogenisation study is the expected values for the temperatures of solid solution as obtained from literature data (see §1.4). The expected values for the monophase regions for the 69/30 and the 59/40 alloy were obtained by neglecting the Rh-content of these alloys. From Table 4 it follows, that Rh dissolves mainly in the Pt-rich phase. Clearly, the Rh-addition enhances the stability to such an extent, that under conditions of practical interest, the 69/30 and the 59/40 alloy can not be brought in a monophase condition.

Pd shows large possibilities of solid solution in both the Au-rich and Pt-rich phases [3,4]. Hence, it can be expected that the presence of Pd brings down the boundary of the monophase temperature region. The presence of Pd is also expected to increase the solidus-temperature, again resulting in an enlargement of the monophase temperature region. Indeed, for the 54/27.5/17 and for the 44.5/37/17 alloys homogenisation was possible above temperatures of 1300°C and 1400°C, respectively. Assuming a parabolic miscibility gap for these alloys in the appropriate section at 17 at. % Pd of the

ternary AuPtPd system (implying ignorance of the Rh-addition), the fact that the homogenisation temperature for the 44.5/37/17 alloy is higher than for the 54/27.5/17 alloy denotes that the position of the 54/27.5/17 is at the Au-rich side of the miscibility gap top.

Table 9. Comparison of expected and experimental data on homogenisation.

Alloy	Expected monophase region	Experimental data	
		DTA	Light microscopy
69/30	940-1220°C	melting starts at 1220°C	up to 1250°C dual-phase 1300°C melting starts
59/40	1130-1260°C	endothermic effect above 1260°C melting starts at 1280°C	up to 1270°C dual-phase
54/27.5/17	above 1050°C	endothermic effect 1200-1280°C no melting up to 1350°C	up to 1270°C dual-phase 1300°C monophase
44.5/37/17	above 1125°C	no endothermic effect or melting up to 1350°C	1400°C monophase

The results of the homogenisation study were described in §4.3. In Table 9 these results are compared with the expectations. The expectations as given in Table 9 were obtained by neglecting the Rh-content, mainly present in the second phase. Clearly, the Rh-addition enhances the stability of this second phase to such an extent, that no monophase regions for the AuPtRh alloys (the 69/30 and the 59/40 alloys) are present. The Rh-addition in the AuPtPdRh alloys also enhances the stability of the Pt-rich phases: the lower temperature of the monophase region is higher than expected. However, the Pd-addition enlarges the monophase region: increasing the solidus line and decreasing the miscibility gap boundary compared to alloys without Pd. Effectively, this results in a monophase region from 1300°C and 1400°C onwards (see Table 5). Comparing the experimental results obtained from DTA and light microscopy, it is noticed that the results for the 54/27.5/17 alloy and for the 44.5/37/17 alloy show no contradiction, whereas for the 69/30 and 59/40 alloys some discrepancies do occur, especially the start of melting. Further examinations are necessary to clarify this point.

5.3. Microstructure after rolling, homogenisation and quenching

From the above section it becomes apparent that in many cases the alloys studied show after rolling, homogenisation and quenching a dual-phase microstructure. This microstructure is the starting point for subsequent heat-treatment. Hence, characterisation of this dual-phase condition is important.

5.3.1. Characterisation of the alloys after rolling, homogenisation and quenching

All the alloys studied in the as-received state did indeed show a dual-phase microstructure (see Figures 14-18). According to Figure 20 a strong relation exists between the Pt/Au ratio and the volume fraction of second-phase particles. Ignoring the Rh-content this goes without saying for the 69/30 and the 59/40 alloys. For the alloys with a constant Pd-content it is remarked that also in the section of 17 at. % Pd for the ternary AuPtPd system the Pt/Au ratio determines the lever point of the lever rule giving the volume fraction of second phase. Further, it is noticed that the observed volume fractions of the second phase are non-zero, whereas for the binary Au-Pt diagram application of the lever rule for the Pt/Au ratios yields a zero value for the homogenisation temperatures applied. This hints again at a stabilising effect of the second phase by the Rh-addition.
From Table 4 it is derived that Rh dissolves mainly in the second phase. Further it can be remarked that the content of non-Au atoms of the Pt-rich phase is constant within the experimental error. This suggests strongly that compositional variations for the alloys studied correspond to compositional variations of the matrix phase and to a variation of the volume fraction of the second phase (see also Table 10).

Table 10. Compositional variations of matrix and second-phase in terms of Au content and non-Au content, and average volume fraction second-phase (f), after rolling, homogenisation (at T_H), and quenching.

Alloy	Pt/Au ratio	T_H (°C)	f	Matrix composition (at. %)		Second-phase composition (at. %)	
				Au	non-Au	Au	non-Au
69/30	0.46	1100	0.082	72.6	27.4	12.8	87.2
54/27.5/17	0.52	1100	0.112	60.5	39.5	13.6	86.4
59/40	0.67	1050	0.147	67.7	32.3	15.0	85.0
44.5/37/17	0.81	1100	0.210	56.9	43.1	15.9	84.1

Figures 14-18 show microstructures of the alloys studied after rolling, homogenisation and quenching. In correspondence with Table 3, the visible amount of second-phase particles increases in the order of 69/30, 54/27.5/17, 59/40, 44.5/37/17 alloys. The second-phase particles are plate-shaped along the rolling direction (see Figures 14-18). This indicates that the second-phase particles were already present prior to the final homogenisation treatment. As homogenisation takes place before and after rolling at the same temperature (halfway the rolling there is a treatment of 30 minutes at 900°C), totalling the time of homogenisation at about 1h at 1100°C, it may be assumed that the volume fraction of second-phase particles after rolling, homogenisation and quenching approaches the equilibrium value (the applied ageing treatments for maximal hardness are in the order of hours of ageing at about 600°C; see §4.2).

The volume fraction of second-phase particles appeared to depend on the relative distance to the rolling plate surface (see Figure 19). The measured profiles are most pronounced for the 69/30 alloy, whereas the profiles for the remaining alloys are less pronounced. An explanation for these profiles may be found in one of the following effects, or a combination of these effects:

1. Crystal segregation on casting;
2. Rapid cooling at the surface and retarded cooling in the centre on casting, introducing grain size differences within the cast billet. The subsequent deformation proceeds heterogeneously; and
3. Inhomogeneous nucleation for precipitation during the heat treatments, due to differences in grain size and dislocation density.

The available experimental evidence does not allow for one specific explanation for the observed profiles.

The lower-grade alloys are somewhat more susceptible for local variations of second-phase-particles volume fraction, as for the lower grade alloys the supersaturation of the matrix phase on quenching is somewhat lower than for the higher-grade alloys. For the higher-grade alloys, precipitation of the second-phase particles proceeds easier than for the lower-grade alloys, resulting in a less pronounced profile.

The observed profiles for the volume fraction correspond fairly well to the hardness profiles (see Figures 13, 40 and 41). Again the profiles for the 69/30 alloy are most pronounced. Clearly, an increase of the volume fraction of second-phase particles is related with an increase of hardness (see §5.5).

A further increase of the homogenisation temperature will result in dissolution of second-phase particles and a larger contribution of solid solution hardening to the hardness value measured. In correspondence with the foregoing for the 69/30 alloy, a sharpening of the hardness profile may be expected, as is observed (see Figure 40). As for the high-grade alloy more alloying atoms can be dissolved, the hardness level to be

reached by the high-grade alloy will be higher than for the low grade alloy, as is observed (compare Figure 41 with Figure 40).

5.3.2. Hardness after rolling, homogenisation and quenching

As a first indication of the mechanical properties, the hardness of the alloys after rolling, homogenisation and quenching was measured. In Table 11 the measured values are brought together with microstructural data.
The measured hardness of the alloys is a weighted average of the hardness of the matrix and the contribution by the presence of the second-phase particles. It was already found that for a matrix of given composition, the increase of the volume fraction of second-phase particles resulted in a hardness increase (see Figures 13 and 19, in which the contribution of Pd to the solid solution hardening for the 54/27.5/17 alloy and the 44.5/37/17 alloy should be taken into account). Changing the balance between matrix and second phase has a great effect on the resulting hardness values, as is revealed by Table 11. This implies that for the case of the spinneret alloys investigated, solid solution hardening plays an important part in the measured values of hardness. The disappearance of second-phase particles, or even the decrease of their volume fraction, can result in a drastic hardness increase. Of course, the increase of homogenisation temperature finds limits in the solidus line. This was observed for the 69/30 alloy: after homogenisation at 1300°C partial melting had occurred (see Figure 34). Further, grain growth can be important, yielding at least a hardness decrease beyond a maximum (see the case for the 54/27.5/17 alloy in Figure 42).

Table 11. Hardness and average volume fraction second-phase (f) after rolling, homogenisation (at T_H for t_H hours) and quenching.

Alloy	T_H (°C)	t_H (h)	f	Microstructure Figure(s)	Hardness*1) (H_V)
69/30	950-1150	0.5	0.082	14, 15	130-150
	1200	0.5	(dual-phase)		170
	1100 + 1250	0.5 1	(dual-phase)	33	205
	1100 + 1300	0.5 1	(dual-phase)	34	140
59/40	1000-1050	0.5	0.147	16	140-145
	1100	0.5	(dual-phase)		175
54/27.5/17	950-1100	0.5	0.112	17	150-160
	1150	0.5	(dual-phase)		175
	1200	0.5	(dual-phase)		195
	1100 + 1250	0.5 1	(dual-phase)		310
	1100 + 1300	0.5 1	(monophase)	37	420
44.5/37/17	1000-1050	0.5	(dual-phase)		175
	1100	0.5	0.210	18	195
	1100 + 1400	0.5 1	(monophase)	39, 51*2)	415

*1) All hardness values in this study are obtained from embedded specimens (see §3.1). For homogenised and quenched specimens the embedding is an ageing treatment at 150°C resulting in a hardness increase. The highest hardness increase due to embedding will occur for cases with the largest supersaturation. This hardness increase is about 50 HV (see §4.4).

*2) Second-phase particles are seen at high magnification in Figure 51, apparently evolved from the light, depleted zone with a width of 5 μm. On the basis of an estimation of the diffusion length of Pt in Au at 1400°C $x = \sqrt{Dt}$ with $D=6.10^{-8}$ ($cm^2.s^{-1}$) [22], it is thought that these second-phase particles are precipitated as a result of inadequate quenching. These precipitates give rise to the alloys hardness.

5.3.3. Strength and strain at fracture after homogenisation and quenching

The hardness can be considered as an indication for strength (see Appendix C), but it contains no information about deformation possibilities. The latter is of utmost importance for the spinneret production and service [1]. Again, it will be interesting to relate the values for σ_y, σ_{UTS}, and ε_f with microstructural data. Therefore, Table 12 gathers the mechanical properties as a function of homogenisation treatment applied.

Table 12. Mechanical properties and average volume fraction second-phase (f) after rolling, homogenisation (at T_H for t_H hours), and quenching.

Alloy	T_H (°C)	t_H (h)	f	Microstructure Figure(s)	σ_y (MPa)	σ_{UTS} (MPa)	ε_f (%)
69/30	1100	0.5	0.082	14, 15	235	424	36.7
59/40	1050	0.5	0.147	16			
54/27.5/17	1100	0.5	0.112	17	354 387*1) 397*2)	530 545*1) 542*2)	22.0 23.1*1) 21.1*2)
	1100 + 1350	0.5 1	0		681*1) 618*2)	874*1) 805*2)	7.5*1) 8.2*2)
44.5/37/17	1100	0.5	0.210	18	470	625	23.7
	1100 + 1400	0.5 1	0	39, 51		623*3)	0.1*3)

*1) Average value from Table 8, for the 0.8 mm thickness specimens.
*2) Average value from Table 8, for the 0.6 mm thickness specimens.
*3) Average value from Table 8.

Comparison of the results of Table 12 with Table 11, yields that indeed the disappearance of the second-phase particles induces an increase in strength, see the case for the 54/27.5/17 alloy. For the 44.5/37/17 alloy this correspondence was not confirmed as the region of plastic deformation was not reached. It is thought that the presence of second-phase particles at the grain boundaries (see Figure 51) play an deteriorative role for the value of σ_{UTS}, as it is observed that the fracture proceeds via the grain boundaries.
The strength increase is however accompanied by a drastic reduction of ε_f, leaving virtually no deformation possibilities. The foregoing suggests, that the presence and

properties of the second-phase particles are essential for the occurring values of mechanical properties, such as ε_f. It is noted, that after homogenisation yielding a monophase condition, the strength of the 54/27.5/17 alloy is higher than the one of the 44.5/37/17 alloy (see for a further discussion of the relation between microstructure and mechanical properties §5.4.2).

5.4. The alloys during and after ageing

On the basis of the foregoing it can be said that the optimal strength, hardness, and strain at fracture will depend on a critical balance between homogenisation, influencing to a large extent the contribution of solid solution strengthening, and precipitation determining the contribution due to presence of second-phase particles.
For the alloy specimens that were dual phase after homogenisation and quenching, the light-microscopical appearance did not change on ageing: the alloys were dual phase at the start of ageing and remained it on ageing. This was evidently not the case with the specimens that were monophase after homogenisation and quenching. Then, ageing resulted in a dual-phase microstructure, as is observed in Figures 49 and 50. All phases present after homogenisation and quenching are in a supersaturated condition and ageing will involve precipitation as is indicated by the variation in hardness as a function of ageing treatment (see Figures 21-24, 25-28, and 43-45).

5.4.1. The hardness as a function of ageing treatment

5.4.1.1. After homogenisation at temperatures between 950-1200°C

Isochronical ageing (3 hours) yielded maximum hardnesses for ageing temperatures of 550°C and 600°C (the hardness effect due to embedding at 150°C will be of no importance for the hardness values after ageing as the embedding as an ageing treatment can be neglected in comparison with the ageing treatment applied) for the highest homogenisation temperatures applied. For the 69/30 alloy, the maximum hardness at 550°C for homogenisation temperatures of 1150°C and 1200°C did not differ significantly, equalling 320 Hv. For the 59/40 alloy, the maximum hardness at 500°C and 550°C was obtained after homogenisation at 1100°C. For the 54/27.5/17 alloy, maximum hardness occurred at 600°C, not differing significantly for homogenisation temperatures between 1100-1200°C. For the 44.5/37/17 alloy maximum hardness occurred at 550°C after homogenisation at 1100°C.
From the foregoing results it was concluded that the supersaturation obtained at 1100°C is sufficient to yield an important increase of hardness as compared to the AQ values of hardness (see Figures 21-24). To get a further insight in the kinetics of precipitation

processes occurring, isothermal ageing is studied after homogenisation at temperatures of 1050-1100°C and subsequent quenching. This choice is also based on the current production practice of spinnerets.

It appeared that ageing at 400°C did not significantly change the hardness as compared to AQ values (see Figure 25). Figures 26-28 provide information on the kinetics of precipitation during ageing at 500°C, 600°C, and 700°C. The following interpretative remarks can be made:

1. The largest hardness increase is observed for the 54/27.5/17 and for the 44.5/37/17 alloys, for ageing at 600°C. This is in correspondence with the findings of Figures 21-24.
2. The rate of hardness change is also highest for the 54/27.5/17 and for the 44.5/37/17 alloys and lowest for the 69/30 and 59/40 alloys. However, the times to reach maximal hardness correspond mutually fairly well for the alloys studied. These times are gathered in Table 13.

After homogenisation and quenching all the alloys were dual-phase. The composition of both phases (see Table 4) imply that both the matrix phase and the second-phase are supersaturated at ageing temperatures applied (see the appropriate phase-diagram sections in §1.4). Suppose that the concentration of the non-Au atoms for the matrix phase are given by $c_{m\ 0}^{n\ Au}$, $c_{m\ t}^{n\ Au}$, and $c_{m\ \infty}^{n\ Au}$, for respectively at the start of ageing, after a time t of ageing, and in equilibrium condition (t=∞). Analogously for the second phase can be written $c_{s\ 0}^{n\ Pt}$, $c_{s\ t}^{n\ Pt}$, and $c_{s\ \infty}^{n\ Pt}$.

Table 13. Ageing times (t_A at T_A°C) to reach maximal hardness (H_m) after homogenisation at 1050-1100°C (t_H time at T_H).

Alloy	T_H (°C)	t_H (h)	T_A (°C)	t_A (h)	H_m (Hv)
69/30	1100	0.5	600	1.5	250
			700	0.2	225
59/40	1050	0.5	500	5.5	340
			600	0.9	305
			700	0.3	210
54/27.5/17	1100	0.5	600	1.5	375
			700	0.7	330
44.5/37/17	1100	0.5	500	5	325
			600	1.5	360
			700	0.3	310

At the start of ageing the total amount of atoms to be precipitated is given by

$$c_{m\ 0}^{n\ Au} - c_{m\ \infty}^{n\ Au} + c_{s\ 0}^{n\ Pt} - c_{s\ \infty}^{n\ Pt} = c_{\infty}^{Prec} \tag{41}$$

The number of atoms precipitated after ageing time, t, is given by

$$c_{m\ 0}^{n\ Au} - c_{m\ t}^{n\ Au} + c_{s\ 0}^{n\ Pt} - c_{s\ t}^{n\ Pt} = c_{t}^{Prec} \tag{42}$$

Now the fraction transformed, X_t, can be defined as

$$X_t = \frac{c_t^{Prec}}{c_{\infty}^{Prec}} \tag{43}$$

Assuming that a constant value of X_t corresponds with the observed hardness maximum and that a function $F(X_t)$ is completely determined by the state variable $\beta = t \exp(-\frac{E_a}{k_B T})$, with E_a the activation energy, t the ageing time in seconds, T the ageing temperature in K, and $k_B = 1.3806.10^{-23}$ $(J.K^{-1})$ Boltzman's constant, then the slope of the straight line through the data points of ln t_m (with t_m as the time to reach maximum hardness) versus $\frac{1}{T}$ yields an apparent value for E_a. For the 59/40 and

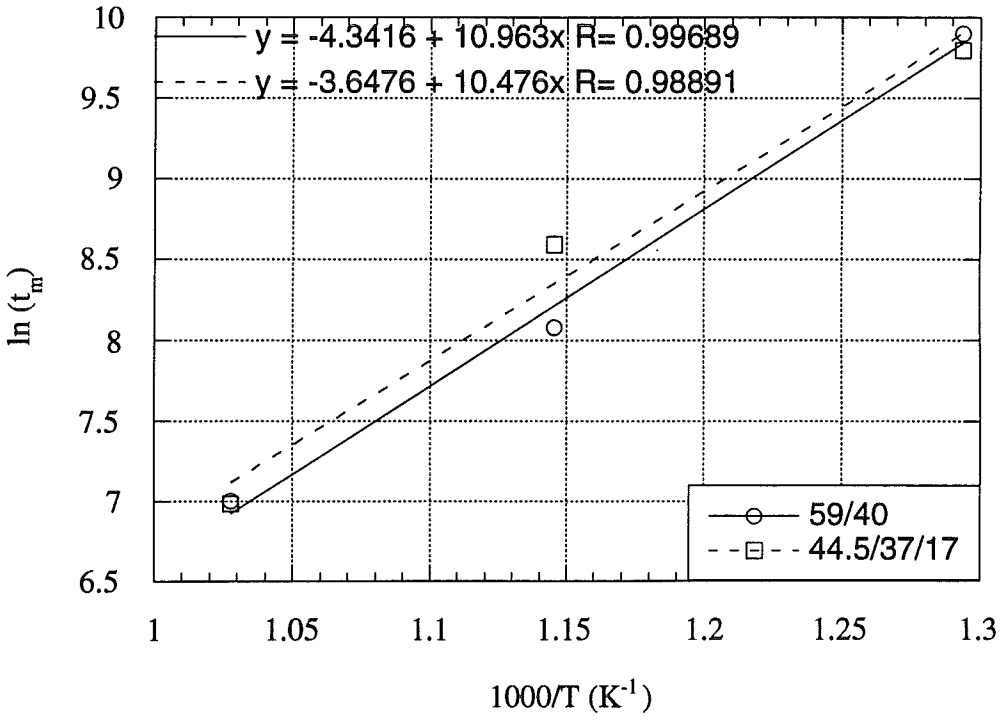

Figure 52. The logarithm of the time to reach maximal hardness, $\ln(t_m)$, as a function of the reciprocal ageing temperature, for ageing in the dual-phase condition.

for the 44.5/37/17 alloys this is performed in Figure 52.
The values (see Table 14) observed for the apparent E_a in these two cases correspond mutually. The apparent E_a is of the order of the activation energy for diffusion (E_d) in Au (see Table 15) at the ageing temperatures applied, but numerically E_a is found to be half the value of E_d. It is noted that two precipitation processes proceed at the same time: one in the matrix and one in the second phase. As in Figures 25-28, no signs of incubation times are observed, spinodal decomposition is thought the active precipitation process.

Table 14. Apparent activation energies (E_a=1000*slope*k_B) for precipitation from the dual phase.

Alloy	Slope	E_a (J)
59/40	10.963	$1.5.10^{-19}$
44.5/37/17	10.476	$1.4.10^{-19}$

Table 15. The activation energy for diffusion (E_d) in Au of Pd and Pt at the ageing temperatures applied [23].

Element	E_d (J)
Pd	$3.2.10^{-19}$
Pt	$3.3.10^{-19}$

5.4.1.2. After homogenisation and quenching from 1350°C and 1400°C
At these temperatures only the 54/27.5/17 and 44.5/37/17 alloys were monophase. From Figures 43-45 it becomes clear that ageing increases the hardness of these homogenised and quenched alloys. The hardness values for the 44.5/37/17 alloy are higher than for the 54/27.5/17 alloy. It is thought that the hardness changes observed result from precipitation from the supersaturated monophase matrix in these alloys. In Table 16 the times to reach maximum hardness are gathered. It is very striking that the kinetics of the precipitation in these alloys are the same.
Suppose that the matrix concentration of the non-Au atoms at the start of ageing is given by $c_{m\ 0}^{n\ Au}$, after a time t of ageing by $c_{m\ t}^{n\ Au}$, and that the equilibrium (t=∞) concentration is given by $c_{m\ \infty}^{n\ Au}$. Then the fraction transformed, X_t, can be defined as

Table 16. Ageing times (t_A at T_A°C) to reach maximal hardness (H_m) after homogenisation at 1350-1400°C (t_H time at T_H).

Alloy	T_H (°C)	t_H (h)	T_A (°C)	t_A (h)	H_m (Hv)
54/27.5/17	1350	1	500	16	460
			600	2	450
			700	0.25	430
44.5/37/17	1400	1	500	16	500
			600	2	515
			700	0.25	475

$$X_t = \frac{c_{m\,0}^{n\,Au} - c_{m\,t}^{n\,Au}}{c_{m\,0}^{n\,Au} - c_{m\,\infty}^{n\,Au}} \qquad (44)$$

With analogous reasoning as in the previous section an apparent value for E_a can be found from the slope of the straight line through the data points of ln t_m (with t_m as the time to reach maximum hardness) versus $\frac{1}{T}$. This is performed in Figure 53.

The values (see Table 17) observed for the apparent E_a in these two cases are equal. The apparent E_a is of the order of the activation energy for diffusion (E_d) in Au (see Table 15) at the ageing temperatures applied, but numerically E_a is found to be two-third of the value of E_d. It is noted that the precipitation partially takes place at the crystal boundaries (discontinuous precipitation, see Figure 50) giving diffusion-pipe shortcuts along the grain boundaries resulting in a lower apparent activation energy for diffusion. As in Figures 43-45, no signs of incubation times are observed, spinodal decomposition is, as expected, thought the active precipitation process.

Table 17. Apparent activation energies (E_a=1000*slope*k_B) for precipitation from the monophase condition.

Alloy	Slope	E_a (J)
54/27.5/17	15.572	$2.1.10^{-19}$
44.5/37/17	15.572	$2.1.10^{-19}$

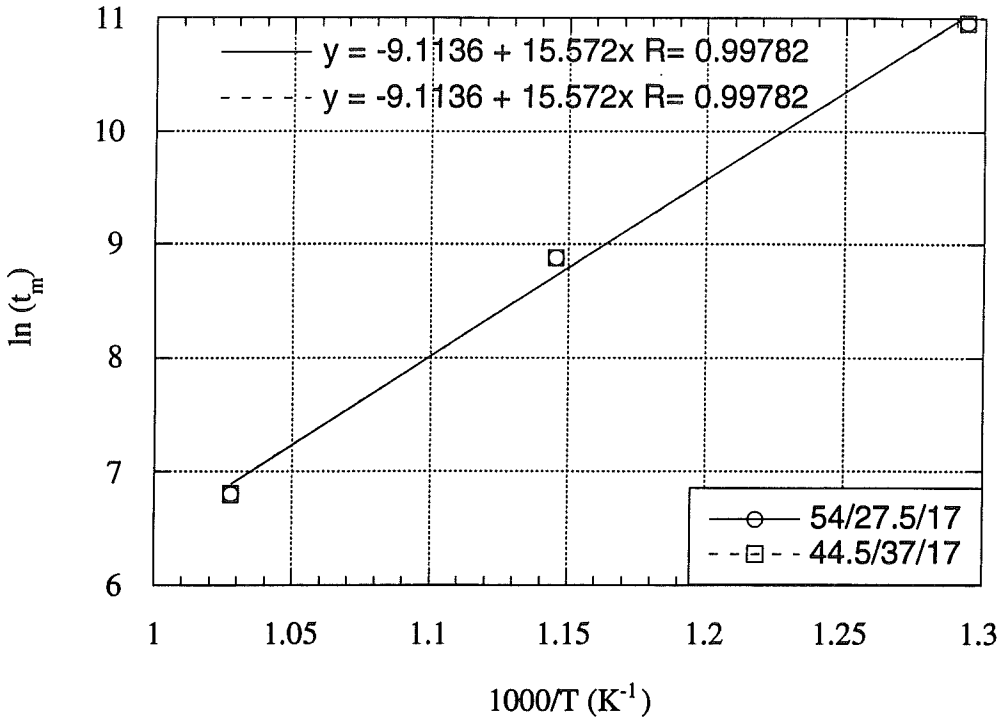

Figure 53. The logarithm of the time to reach maximal hardness, $\ln(t_m)$, as a function of the reciprocal ageing temperature, for ageing in the monophase condition.

5.4.1.3. Some remarks on the obtained values for the apparent activation energies for precipitation

The obtained values for the apparent activation energies for precipitation in the homogenised and quenched alloys are significantly lower than the corresponding value for diffusion in pure gold. Firstly, it is noted that the quenched alloys do show an increased vacancy concentration due to the presence of quenched-in vacancies. This presence can indeed lower the apparent activation energy (see [24]). Secondly, it is remarked that the monophase alloys did suffer from grain growth due to the increased temperatures of homogenisation as compared to the quenched dual-phase alloys, which were quenched from decreased homogenisation temperatures and which as a result of the presence of the second-phase particles did not show a large grain growth. Hence, the grain boundary concentration in the dual-phase alloys are inevitably larger than in the quenched monophase alloys. This might explain the difference in apparent activation energy for precipitation as observed between the two groups of alloys.

5.4.2. Strength and strain at fracture as a function of ageing treatment

In Table 18 the strength, strain at fracture and hardening coefficient are gathered as obtained from specimens that were dual phase on the start of ageing. In Table 19 the

Table 18. Strength, strain at fracture, and strain hardening coefficient as a function of ageing treatment (for t_A hours at T_A°C) after homogenisation at 1050-1100°C (for t_H hours at T_H°C).

Alloy	T_H (°C)	t_H (h)	T_A (°C)	t_A (h)	σ_y (MPa)	σ_{UTS} (MPa)	ε_f (%)	n
69/30	1100	0.5			235	424	36.7	
	1100	0.5	550	3	818	987	17.8	
59/40	1050	0.5	550	3	928	991	3.5*1)	
54/27.5/17	1100	0.5			354	530	22.0	
(Batch A)	1100	0.5	600	3	986	1193	9.5*1)	
54/27.5/17	1100	0.5			387	545	23.1	0.23
(Batch B 0.8 mm)	1100	0.5	600	3	867*1)	993*1)	13.4*2)	0.12*1)
54/27.5/17	1100	0.5			397	542	21.1	0.22
(Batch B 0.6 mm)	1100	0.5	600	3	798*1)	926*1)	13.4*2)	0.12*1)
44.5/37/17	1100	0.5			470	625	23.7	0.18
	1100	0.5	550	3	945*1)	1039*1)	19.8*2)	0.12*1)
	1100	0.5	600	3	1041	1109	2.1*1)	

*1) These low values for ε_f are most probably due to inadequate geometry of tensile test specimens (see §3.5 and Appendix C).
*2) Averaged value from Table 8.

strength, strain at fracture and hardening coefficient are gathered as obtained from specimens that were monophase on the start of ageing. From these Tables 18 and 19 it can be derived that the strain at fracture and the hardening coefficient, that holds a relation with the ratio between σ_y and σ_{UTS} for a given ε_f, are largest for the dual-phase homogenised and quenched specimens. The combination of a high strength and a high value for ε_f occurs for the 69/30 alloy after homogenisation at 1100°C followed by 3 hours of ageing at 550°C, and for the 44.5/37/17 alloy after homogenising at 1100°C followed by 3 hours of ageing at 550°C (see Table 18).
Complete homogenisation yields a decrease of the strain hardening coefficient from 0.20 to about 0.10, and of the strain at fracture from above 20% to well below 10% (compare the results for the 54/27.5/17 and 44.5/37/17 alloys of Table 18 with those of Table 19). However, a further decrease of n and ε_f occur for subsequent ageing, inducing a great increase in strength but also annihilation of the possibilities of plastic deformation (see Table 19). From the foregoing it can be concluded that the recently formed precipitates (after homogenisation at 1350-1400°C also precipitates are formed

Table 19. Strength, strain at fracture, and strain hardening coefficient as a function of ageing treatment (for t_A hours at T_A°C) after homogenisation at 1350-1400°C (for t_H hours at T_H°C).

Alloy	T_H (°C)	t_H (h)	T_A (°C)	t_A (h)	σ_y (MPa)	σ_{UTS} (MPa)	ε_f (%)	n
54/27.5/17	1350	1			681*1)	874*1)	7.5*1)	0.12*1)
(Batch B 0.8 mm)	1350	1	600	1	1050	1074	1.1	
	1350	1	600	2	1066	1103	1.2	
	1350	1	600	3	1070	1121	1.1	
	1350	1	600	4	1035	1145	1.4	0.14
54/27.5/17	1350	1			618*1)	805*1)	8.2*1)	0.13*1)
(Batch B 0.6 mm)	1350	1	600	1		1002	0.8	
	1350	1	600	2		974*1)	0.7*1)	
	1350	1	600	3		931	0.8	
	1350	1	600	4	986	1142	1.1	0.12
44.5/37/17	1400	1				623*1)	0.1*1)	
	1400	1	600	2	1014	1014	0.0	

*1) Averaged value from Table 8.

due to inadequate quenching), especially those formed at the grain boundaries, are the cause of the brittle fracture of the specimens concerned. That recently formed precipitates are responsible for the brittle fracture, is confirmed by Figures 48-51 where it is observed that crack formation is of intercrystalline nature and that at the crystal boundaries discontinuous precipitation is apparent.

From the foregoing it is concluded that for maintaining good possibilities of plastic deformation, the presence of discontinuous precipitation is not desired.

It is thought that the presence of second-phase can particles result in good possibilities of plastic deformation, both after homogenisation at 1100°C and after subsequent ageing.

After homogenisation at 1100°C, no discontinuous precipitation is observed (see Figures 14-18). Subsequent ageing will result in the formation of precipitates in both matrix and second-phase particles, and again no discontinuous precipitation is observed probably due to the low level of supersaturation. The precipitates give about equal rise to the strength of both matrix and second-phase particles, resulting in a strong alloy with high strain at fracture.

After homogenisation at 1400°C, precipitates are seen at the grain boundaries (see Figure 51). Subsequent ageing will result in the formation of new precipitates in the grain, and will also result in the growth of the discontinuous precipitates at the grain boundaries (see Figure 50). The precipitates in the grain give rise to the strength of the grain. As a result the grain will be much stronger than the large discontinuous precipitates (which are only strengthened by solid solution strengthening), covering large areas of the grain boundaries. When the specimen is strained, the difference in stress between the grain and the second-phase particles (the discontinuous precipitates) will cause the bond between the two phases to breakdown. This results in a very low strain at fracture and intercrystalline crack propagation as is observed (see Table 8 and Figures 46-49).
It is thought that complete homogenisation is not sensible, unless a way is found to prevent discontinuous precipitation. It is found that an advanced level of mechanical properties can be combined with an advanced level of possibilities of plastic deformation. The best combination is represented by the 44.5/37/17 alloy after homogenisation and quenching from 1100°C and 3 hours of ageing at 550°C (see Table 18).

5.5. Strengthening of spinneret alloys

5.5.1. Monophase alloys

In monophase alloys after complete homogenisation, only solid solution strengthening is of relevance. For a binary solid solution it was derived (see chapter 2) that the effective interaction force between dislocations and solute atoms can be written as

$$F_{max}^{eff} \approx Gb^2\sqrt{\delta^2+\eta^2\beta^2} \qquad (8)$$

with

$$\delta = \frac{1+\nu}{3(1-\nu)}\frac{d\ln a}{dc} = \frac{1+\nu}{3(1-\nu)}\frac{1}{a}\frac{da}{dc} \qquad (2)$$

where ν is the Poisson's ratio, a the lattice parameter of the solid solution, and c the solute concentration

$$\eta = \frac{d\ln G}{dc} = \frac{1}{G}\frac{dG}{dc} = \frac{2(G_s-G)}{(1+\alpha)G+(1-\alpha)G_s} \qquad (4)$$

where G is the shear modulus of the matrix, G_S the shear modulus of the solute, and α is given by

$$\alpha = \frac{\nu - \frac{1}{5}}{3(1-\nu)} \tag{5}$$

so for $\nu = 0.4$ α becomes 1/9,

and

$$\beta = \left[(1-\nu)^2 24\pi \frac{z}{b}\right]^{-1} \tag{7}$$

where z is the distance between the slip plane and the parallel plane through the solute atom, and $z \approx b$.

It is remarked that the value of β is rather independent of the nature of the dissolving element. This implies that in equation (8) only the values of δ and η depend on the nature of the solute atoms.
The critical or yield shear stress contribution due to solid solution strengthening can be written as

$$\tau_y^{ss} = \frac{z^{1/3}}{a^{4/3} b T^{1/3} 2(4I)^{1/3}} \left\{ c \left(F_{max}^{eff} \right)^2 \right\}^{2/3} \tag{41}$$

with I a pure number of the order of 1

$$I = \int_0^1 \frac{\partial(F / F_{max})}{\partial(y / z)} dF / F_{max} \tag{20}$$

In the following for I is arbitrarily taken I=0.2, which means that the contribution due to solid solution strengthening is enlarged by 70% as compared to the I=1 case.
It was shown (see §2.2.4) that equation (41) reduces to

$$\tau_y^{SS} = k^{SS} G c^{2/3} (\delta^2 + \beta^2 \eta^2)^{2/3} \tag{23}$$

where

$$k^{SS} = \left(\frac{3}{16\sqrt{I}}\right)^{2/3} \tag{24}$$

It is again noted that in equation (23) only δ and η depend on the nature of the solute atoms.

For a ternary solid solution the yield shear stress contribution due to solid solution strengthening can be written as

$$\tau_y^{ss} = \frac{z^{1/3}}{a^{4/3}bT^{1/3}2(4I)^{1/3}}\left\{c_1\left(F_{1,max}^{eff}\right)^2 + c_2\left(F_{2,max}^{eff}\right)^2\right\}^{2/3} \tag{42}$$

with

$$F_{1,max}^{eff} \approx Gb^2\sqrt{\delta_1^2 + \eta_1^2\beta^2} \tag{43}$$

and

$$F_{2,max}^{eff} \approx Gb^2\sqrt{\delta_2^2 + \eta_2^2\beta^2} \tag{44}$$

Assuming that the factor preceding the parentheses in equation (42) is independent of the nature of the solute atoms, than for the yield shear stress contribution due to solid solution strengthening in a ternary solid solution can be written

$$\tau_y^{SS} = k^{SS}G\left\{c_1(\delta_1^2 + \beta^2\eta_1^2) + c_2(\delta_2^2 + \beta^2\eta_2^2)\right\}^{2/3} \tag{45}$$

Analogously, for the yield shear stress contribution due to solid solution strengthening in a quaternary solid solution it is found

$$\tau_y^{SS} = k^{SS}G\left\{c_1(\delta_1^2 + \beta^2\eta_1^2) + c_2(\delta_2^2 + \beta^2\eta_2^2) + c_3(\delta_3^2 + \beta^2\eta_3^2)\right\}^{2/3} \tag{46}$$

In equations (45) and (46) the suffix with c, δ, and η denotes that the value for the respective alloying element is taken. In correspondence with section 2.2.2. β is about $\frac{1}{27}$. The necessary data ~~is~~ are taken from [25] and are gathered in Table 20.

From [3] it is known that for the alloying elements concerned

$$\frac{da}{dc} = a_{c=0} - a_{c=1} \tag{47}$$

Table 20. Parameters for Au, Pd, Pt and Rh pure metals [25].

Metal	a (Å)	ν	E (GPa)	σ_b (MPa)	G* (GPa)
Au	4.0786	0.42	81	125	28.5
Pd	3.8895	0.52	124	190	40.8
Pt	3.9224	0.36	173	140	63.6
Rh	3.8038	0.36	386	480	141.9

* *G was calculated using* $G = \frac{E}{2(\nu+1)}$ *[8].*

It is assumed that equation (47), obtained for the binary solution, is valid for the ternary and quaternary solutions as well. Using equation (47) with Table 20, the appropriate values for δ and η can be calculated for each alloying element in gold (see Table 21) and for each alloying element in platinum (see Table 22).

Table 21. δ, η, and F_{max}^{eff} for alloying elements in Au, with $b_{Au} = \frac{1}{2} a_{Au} \sqrt{3} = 3.5322$ (Å).

Element	δ	η	$\delta^2+\beta^2\eta^2$	F_{max}^{eff} (pN)
Pd	-0.03784	0.361	0.001611	5.73
Pt	-0.03125	0.795	0.001844	6.56
Rh	-0.05499	1.437	0.005855	20.84

Table 22. δ, η, and F_{max}^{eff} for alloying elements in Pt, with $b_{Pt} = \frac{1}{2} a_{Pt} \sqrt{3} = 3.3969$ (Å).

Element	δ	η	$\delta^2+\beta^2\eta^2$	F_{max}^{eff} (pN)
Au	0.02821	-0.731	0.001528	11.21
Pd	-0.00594	-0.427	0.000285	2.09
Rh	-0.02142	0.796	0.001327	9.74

When τ_y^{ss} from equations (45) and (46) is calculated, the normal yield stress can be calculated as (see §2.5 for the discussion of the proportion between the normal stress σ and the shear stress τ to be used)

$$\sigma_{y,Au}^{SS} = \sigma_y^{Au} + 2\tau_y^{SS} \qquad (48)$$

The 54/27.5/17 alloy and the 44.5/37/17 alloy were investigated in a monophase condition. The relevant data are gathered in Table 23.

Table 23. Relevant data for and calculation of the solid solution strengthening for monophase alloys. σ_{Au}=125 (MPa), G_{Au}=28.5 (GPa), and k^{SS}=0.560.

Alloy	Au	Pt	Pd	Rh	$\Sigma(c_i(\delta_i^2+\beta^2\eta_i^2))$	τ_y^{SS} (MPa)	σ_y^{SS} (MPa)
$(\delta^2+\beta^2\eta^2)*10^4$	0	18.44	16.11	58.55			
54/27.5/17	0.535	0.279	0.169	0.017			
$c_i(\delta^2+\beta^2\eta^2)*10^4$	0	5.15	2.72	1.00	8.87	147	420
44.5/37/17	0.45	0.364	0.169	0.017			
$c_i(\delta^2+\beta^2\eta^2)*10^4$	0	6.71	2.72	1.00	10.43	164	454

The measured and calculated values for σ_y^{SS} are gathered in Table 24. Obviously, a great discrepancy occurs between the measured and calculated values. It should be noted that the values attributed to the individual variables in equations (23), (24), (41), and (47) are based on literature data. Further, it was found that possible simultaneous variations in these values can have contradictory effects on the outcome of the calculations. The net result of possible variations in these values could not be taken into account as to explain the differences as observed. The homogenised specimens did show, some decomposition, as is shown by Figure 51, probably due to inadequate quenching. One is tempted to the conclusion that this decomposition should be taken into account to explain the differences observed in Table 24.

Table 24. Comparison between measured and calculated values for the yield strength of monophase alloys.

Alloy	Monophase strength measured	Monophase strength calculated
	σ_y^{SS}	σ_y^{SS}
54/27.5/17	649*1)	420
44.5/37/17	623*1)	454

*1) Averaged value from Table 8.

5.5.2. Dual-phase alloys

5.5.2.1. After homogenisation and quenching from 1050-1100°C

In the relevant cases two phases are simultaneously present: the Au-rich and the Pt-rich phases. For the solid solution hardening of both the Au-rich phase and the Pt-rich phase equations similar to equations (45) and (46) can be written, where for the shear modulus G is taken respectively G_{Au} and G_{Pt}. The total amount of second-phase particles is given by f. Now for a dual phase alloy with a fixed composition of second-phase particles, it can be written for the yield strength:

$$\sigma_y = (1-f)\left(\sigma_y^{Au} + 2\tau_y^{SS,Au}\right) + f\left(\sigma_y^{Pt} + 2\tau_y^{SS,Pt}\right) \qquad (49)$$

The relevant data for the alloys studied are gathered in Table 25, along with the calculated yield strength of the dual-phase alloys studied and the measured yield strength of the dual-phase alloys studied.

5.5.2.2. After ageing from a monophase condition

This case is very similar to the previous one, but an extra contribution should be accounted for: as the second-phase particles are finely dispersed in the matrix phase, there is a precipitation contribution. In chapter 2 it was derived that this contribution is

$$\tau_y^P \approx 1.949\frac{\gamma f^{1/3}}{b} \qquad (37)$$

with f the volume fraction of precipitates, $b=b_{Au}=\frac{1}{2}a_{Au}\sqrt{3} = 3.5322$ (Å), and γ the precipitate interfacial energy is taken $\gamma=0.1$ ($J.m^{-2}$).

This means that

$$\tau_y^P \approx 551.8f^{1/3} \qquad (50)$$

with τ_y^p in (MPa). Like equation (49) it is derived that

$$\sigma_y = (1-f)\left(\sigma_y^{Au} + 2\tau_y^{SS,Au}\right) + f\left(\sigma_y^{Pt} + 2\tau_y^{SS,Pt}\right) + 2\tau_y^P \qquad (51)$$

Table 25. Calculation of the yield strength for the alloys after homogenisation at 1050-1100°C (T_H). σ_{Au}=125 (MPa), G_{Au}=28.5 (GPa), σ_{Pt}=140 (MPa), G_{Pt}=63.6 (GPa),and k^{SS}=0.560.

Alloy	69/30	59/40	54/27.5/17	44.5/37/17
T_H	1100	1050	1100	1100
f	0.082	0.147	0.112	0.210
Matrix				
Au (at. fraction)	0.726	0.677	0.605	0.569
Pt (at. fraction)	0.271	0.321	0.228	0.255
Pd (at. fraction)	0	0	0.162	0.172
Rh (at. fraction)	0.003	0.002	0.005	0.004
$\Sigma(c_i(\delta_i^2+\beta^2\eta_i^2))$	$5.17.10^{-4}$	$6.04.10^{-4}$	$7.11.10^{-4}$	$7.71.10^{-4}$
$\tau_y^{SS\ Au}$ (MPa)	103	114	127	134
$\sigma_y^{SS\ Au}$ (MPa)	331	353	379	393
Second phase				
Au (at. fraction)	0.128	0.150	0.136	0.159
Pt (at. fraction)	0.809	0.811	0.680	0.672
Pd (at. fraction)	0	0	0.106	0.123
Rh (at. fraction)	0.063	0.039	0.078	0.046
$\Sigma(c_i(\delta_i^2+\beta^2\eta_i^2))$	$2.79.10^{-4}$	$2.81.10^{-4}$	$3.42.10^{-4}$	$3.39.10^{-4}$
$\tau_y^{SS\ Pt}$ (MPa)	152	153	174	173
$\sigma_y^{SS\ Pt}$ (MPa)	444	446	488	486
$\sigma_{y\ calculated}^{SS}$ (MPa)	340	367	391	413
$\sigma_{y\ measured}^{SS}$ (MPa)	235*1)	*2)	392*3)	470

*1) This low value for σ_y is most probably due to inadequate geometry of tensile test specimens (see §3.5 and Appendix C).

*2) Not measured.

*3) Averaged value from Table 8.

It is assumed that the compositions of both matrix and precipitate, are independent of ageing temperature, T_A, in the temperature interval concerned (see also §5.3). On the basis of the assessed phase-diagrams (see §1.4) and the findings of §4.1 the following assumptions are made regarding the compositions of the Au-rich and Pt-rich phases obtained after ageing:

1. For the Au-rich (equilibrium matrix) phase
   - Au balances the composition; for the ageing temperatures applied the compositions are independent of temperature.
   - No Rh is present.
   - The Pt-content is 0.15 (atomic fraction).
   - The Pd-content is the average Pd-content of the alloy.
2. For the Pt-rich (equilibrium second-phase) phase
   - Pt balances the composition; for the ageing temperatures applied the compositions are independent of temperature.
   - All Rh is present in the Pt-rich phase.
   - The Au-content is 0.10 (atomic fraction).
   - The Pd-content is the average Pd-content of the alloy.

As the Au-contents of the alloys studied are given, it follows from the above assumptions that the volume fraction, f, of second-phase particles after ageing at T_A is

$$f = \frac{c_{Au} + c_{Pd} - 0.85}{c_{Pd} - 0.75} \qquad (52)$$

with c_{Au} and c_{Pd} the alloys average content of Au and Pd respectively.
The relevant data for the alloys studied are gathered in Table 26, along with the calculated and measured yield strength of the precipitated monophase alloys studied.

Table 26. Calculation of the yield strength for the alloys after homogenisation at 1350-1400°C (T_H) and optimal ageing. σ_{Au}=125 (MPa), G_{Au}=28.5 (GPa), σ_{Pt}=140 (MPa), G_{Pt}=63.6 (GPa),and k^{SS}=0.560.

Alloy	54/27.5/17	44.5/37/17
T_H	1350	1400
Average		
Au (at. fraction)	0.535	0.450
Pt (at. fraction)	0.279	0.364
Pd (at. fraction)	0.169	0.169
Rh (at. fraction)	0.017	0.017
f	0.251	0.398
τ_y^P (MPa)	348	406
Matrix		
Au (at. fraction)	0.681	0.681
Pt (at. fraction)	0.15	0.15
Pd (at. fraction)	0.169	0.169
Rh (at. fraction)	0	0
$\Sigma(c_i(\delta_i^2+\beta^2\eta_i^2))$	$5.49.10^{-4}$	$5.49.10^{-4}$
$\tau_y^{SS\ Au}$ (MPa)	107	107
$\sigma_y^{SS\ Au}$ (MPa)	339	339
Second phase		
Au (at. fraction)	0.1	0.1
Pt (at. fraction)	0.663	0.688
Pd (at. fraction)	0.169	0.169
Rh (at. fraction)	0.068	0.043
$\Sigma(c_i(\delta_i^2+\beta^2\eta_i^2))$	$2.91.10^{-4}$	$2.58.10^{-4}$
$\tau_y^{SS\ Pt}$ (MPa)	156	144
$\sigma_y^{SS\ Pt}$ (MPa)	453	429
$\sigma_{y\ calculated}$ (MPa)	1064	1187
$\sigma_{y\ measured}$ (MPa)	1014*1)	1144*2)

*1) Highest value from Table 8: 2 hours of ageing at 600°C.

*2) Averaged value from Table 8: 4 hours of ageing at 600°C.

5.5.3. Quaternary-phase condition after ageing from the dual-phase condition

In this case there are two contributions due to precipitation. The first due to contribution in the matrix is

$$\tau_y^{P,Au} \approx 551.8 f_{Pt-rich/Matrix}^{1/3} \qquad (53)$$

with $f_{Pt\text{-}rich/Matrix}$ the volume fraction of Pt-rich precipitates in the matrix after ageing. The second contribution due to precipitation in the second phase, with $b=b_{Pt}=\frac{1}{2} a_{Pt} \sqrt{3}$ = 3.3969 (Å), is

$$\tau_y^{P,Pt} \approx 573.8 f_{Au-rich/SPh}^{1/3} \qquad (54)$$

with $\tau_y^{P\,Pt}$ in (MPa), and $f_{Au\text{-}rich/SPh}$ the volume fraction Au-rich precipitates in the second-phase particles after ageing. Like equation (51) it is derived that

$$\begin{aligned}\sigma_y = &\left\{(1-f_{Matrix/SPh})(1-f_{Pt-rich/Matrix})+f_{Matrix/SPh}f_{Au-rich/SPh}\right\}\left(\sigma_y^{Au}+2\tau_y^{SS,Au}\right)+\\ &\left\{(1-f_{Matrix/SPh})f_{Pt-rich/Matrix}+f_{Matrix/SPh}(1-f_{Au-rich/SPh})\right\}\left(\sigma_y^{Pt}+2\tau_y^{SS,Pt}\right)+\\ &(1-f_{Matrix/SPh})2\tau_y^{P,Au}+f_{Matrix/SPh}2\tau_y^{P,Pt}\end{aligned} \qquad (55)$$

with $f_{Matrix/SPh}$ the fraction of second-phase-particle volume to matrix volume.

When the composition of matrix and second phase at the start of ageing are taken as in Table 4, and for the compositions of the Au-rich and Pt-rich phases after ageing the same assumptions are made as in §5.5.2.2, then the yield stress after ageing from the dual-phase condition can be calculated.

As the Au-content of the phases studied are given in Table 4, it follows from the above assumptions that the volume fraction, f, of Pt-rich phase after ageing at T_A is

$$f = \frac{c_{Au}+c_{Pd}-0.85}{c_{Pd}-0.75} \qquad (56)$$

with c_{Au} and c_{Pd} the phases average content (prior to ageing) of Au and Pd respectively.

The relevant data are gathered in Table 27, along with the calculated yield strength of the precipitated dual-phase alloys studied and the measured yield strength of the precipitated dual-phase alloys studied.

Table 27. Calculation of the yield strength for the alloys after homogenisation at 1050-1100°C (T_H) and optimal ageing (for t_A at T_A). σ_{Au}=125 (MPa), G_{Au}=28.5 (GPa), σ_{Pt}=140 (MPa), G_{Pt}=63.6 (GPa),and k^{SS}=0.560.

Alloy	69/30	59/40	54/27.5/17	44.5/37/17
T_H	1100	1050	1100	1100
t_A	3h	3h	3h	3h
T_A	550	550	600	550
$f_{Matrix/Second-phase}$	0.082	0.147	0.112	0.210
Matrix (average)				
Au (at. fraction)	0.726	0.677	0.605	0.569
Pt (at. fraction)	0.271	0.321	0.228	0.255
Pd (at. fraction)	0	0	0.162	0.172
Rh (at. fraction)	0.003	0.002	0.005	0.004
$f_{Pt\text{-rich in Matrix}}$	0.165	0.231	0.141	0.189
$\tau_y^{P\,Au}$ in (MPa)	303	338	287	317
Second phase (average)				
Au (at. fraction)	0.128	0.150	0.136	0.159
Pt (at. fraction)	0.809	0.811	0.680	0.672
Pd (at. fraction)	0	0	0.106	0.123
Rh (at. fraction)	0.063	0.039	0.078	0.046
$f_{Au\text{-rich in SPh}}$	0.037	0.067	0.056	0.094
$\tau_y^{P\,Pt}$ (MPa)	192	233	219	261
Au-rich phase				
Au (at. fraction)	0.85	0.85	0.681	0.681
Pt (at. fraction)	0.15	0.15	0.15	0.15
Pd (at. fraction)	0	0	0.169	0.169
Rh (at. fraction)	0	0	0	0
$\Sigma(c_i(\delta_i^2+\beta^2\eta_i^2))$	$2.77.10^{-4}$	$2.77.10^{-4}$	$5.49.10^{-4}$	$5.49.10^{-4}$
$\tau_y^{SS\,Au}$ (MPa)	68	68	107	107
$\sigma_y^{SS\,Au}$ (MPa)	261	261	339	339
Pt-rich phase				
Au (at. fraction)	0.1	0.1	0.1	0.1
Pt (at. fraction)	0.861	0.870	0.657	0.681
Pd (at. fraction)	0	0	0.169	0.169
Rh (at. fraction)	0.039	0.030	0.074	0.050
$\Sigma(c_i(\delta_i^2+\beta^2\eta_i^2))$	$2.05.10^{-4}$	$1.93.10^{-4}$	$2.99.10^{-4}$	$2.67.10^{-4}$
$\tau_y^{SS\,Pt}$ (MPa)	124	119	159	148
$\sigma_y^{SS\,Pt}$ (MPa)	387	378	459	435
$\sigma_{y\,calculated}$ (MPa)	878	945	925	982
$\sigma_{y\,measured}$ (MPa)	818	928	832*1)	945*1)

*1) Averaged value from Table 8.

5.5.4. Comparison between calculated and measured values of yield strength

The strength of an alloy will, in general, be determined by the alloy's composition and its microstructure. The microstructure in turn is the result of the applied heat treatment. The most important parameter which is a function of composition and heat treatment, is the volume fraction of Pt-rich phase. In Figure 54, the yield stress is given as function of the volume fraction of the Pt-rich phase.

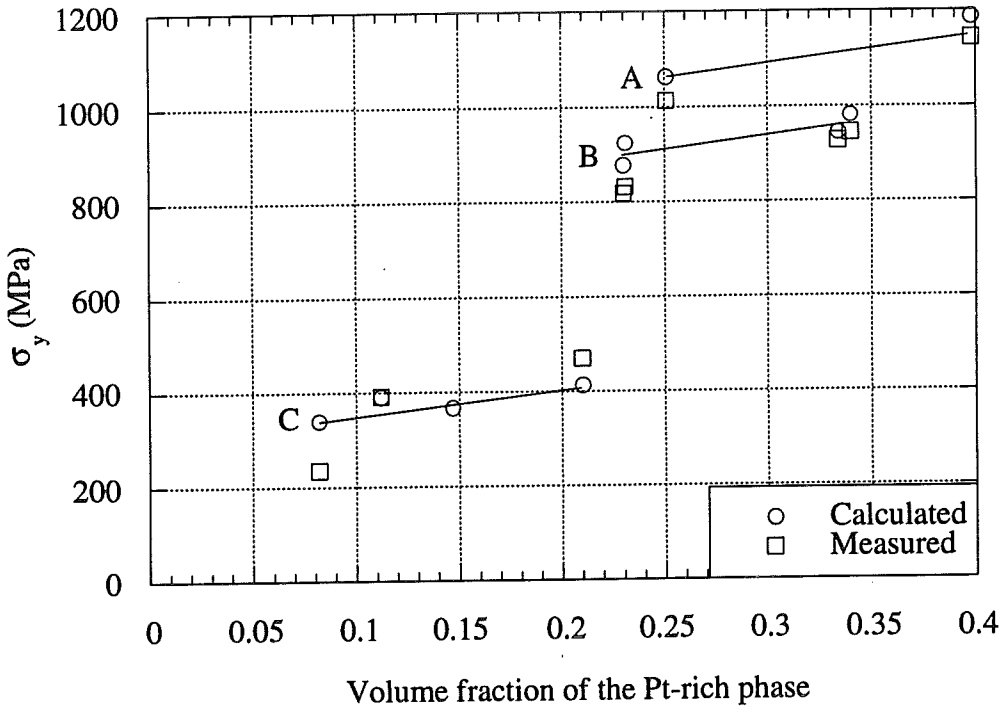

Figure 54. The yield stress as function of the volume fraction of the Pt-rich phase. Three lines are drawn corresponding to three conditions:

A. The monophase structure (after homogenisation at 1350-1400°C) after subsequent ageing.

B. The dual-phase structure after subsequent ageing.

C. The dual-phase structure after homogenisation and quenching from 1050-1100°C.

From Figure 54 it becomes clear that the calculated values of the yield stress correspond fairly well with the measured values of the yield stress. This is a confirmation of the theory as presented in chapter 2 and of the assumptions made in section §5.3.

It is obvious from Figure 54, that for a given condition (A,B or C) an increase of the volume fraction of the Pt-rich phase, does not have a great impact on the yield strength of the alloys concerned. However, as a result of the decomposition occurring in both the matrix and the second phase, a large increase of the volume fraction of the Pt-rich phases occurs having a large impact on the yield strength (condition C ⇒ B). The highest level of yield strength is observed for the condition A obtained by

decomposition from the monophase condition. For the condition A, again the increase of the volume fraction of the Pt-rich phase has a rather small impact.
Clearly, the strength increase related with the change in microstructure (presence and distribution of the phases resulting from decomposition) is of paramount importance for the strength level of the alloys. To illustrate this point, it is useful to distinguish between Pt-rich phase present prior to ageing and Pt-rich phase that was formed during ageing, as only the latter part contributes to the precipitation strengthening. In the dual-phase alloys there is also formation of Au-rich precipitates in the second phase. According to the theory of chapter 2 (see also equations (53) and (54)), the yield strength is a linear function of the third power root of the total amount of precipitate (f_{tot}), i.e. the summation of the volume fractions of the Au-rich precipitates in the Pt-rich phase and Pt-rich precipitate in the Au-rich phase. In Figure 55 the yield strength is given as a function of $f_{tot}^{1/3}$.

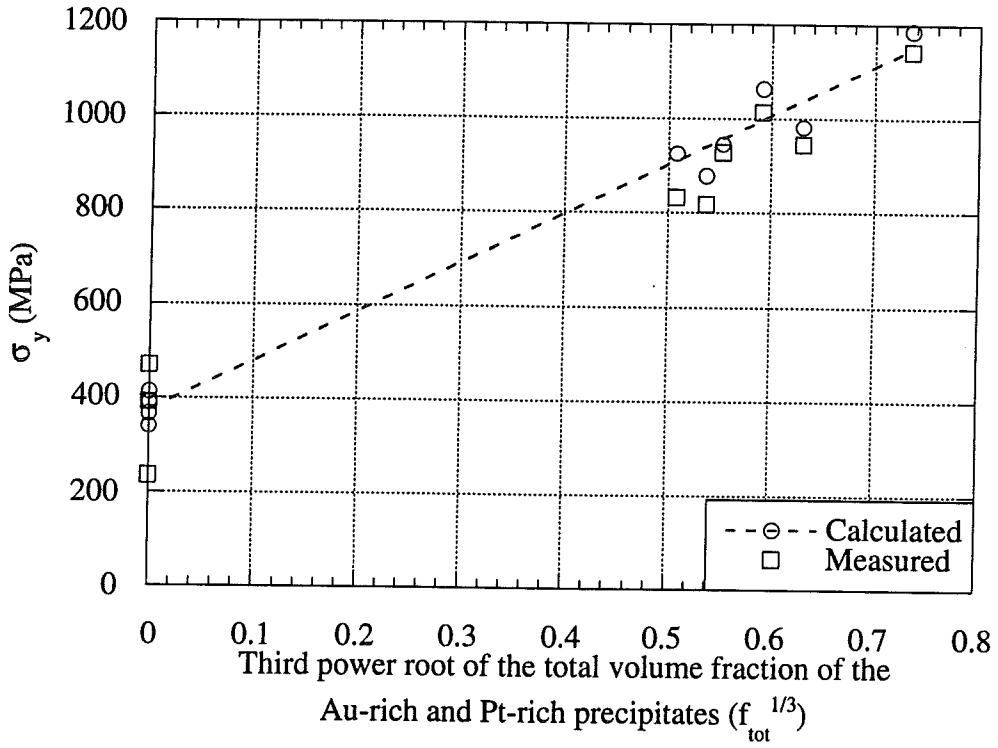

Figure 55. The yield stress as function of $f_{tot}^{1/3}$.

From Figure 55 it is obvious that a linear relation between the yield strength and $f^{1/3}$ exists. The dashed line in Figure 55 is obtained by a least-squares-fit to the calculated data points. The slope of this line is 1050 (MPa), which is in close agreement with the values following from equations (53) and (54). It is obvious that the new, dispersed phases, formed during decomposition, give rise to the alloy's strength. Furthermore, it is seen that the decomposition contribution to the yield strength is much more important than the solid solution contribution to the strength.

6. Conclusion

1. The Labusch theory for solid solution strengthening and the theory of precipitation strengthening provide a valuable tool for the development of alloys: the predictions based on the combined application of these theories correspond fairly well with the measurements.

2. The presence and distribution of the second-phase particles are of paramount importance for the mechanical properties: the presence of discontinuous precipitates on grain boundaries has to be avoided, whereas second-phase particles present in the original phases as a result of their decomposition provide the optimum combination of strength and strain at fracture.

3. The decomposed dual-phase condition shows the optimum combination of high strength and high strain at fracture (see Table 8).

4. The increase of the Pt-content implies an increase of the decomposition contribution to the strength (see Figure 55). Hence, the strength values obtained for the 44.5/37/17 alloy in the decomposed dual-phase condition are higher than for the 54/27.5/17 alloy, the difference being about 100 MPa.

5. Homogenisation, if possible, results in the highest strength possible (see Figure 54, condition A). Decomposition from the homogenised condition implies discontinuous precipitation yielding unacceptable low values for strain at fracture.

6. The apparent activation energy of decomposition from the dual-phase condition is $E_a=1.5.10^{-19}$ (J) and from the monophase condition $E_a=2.1.10^{-19}$ (J). Both values are smaller than, but in the order of, the activation energy for diffusion of Pt and Pd in Au, $E_d=3.3.10^{-19}$ (J).

7. The addition of Rh stabilises the Pt-rich phase. In the AuPtRh alloys the addition of 1 at. % Rh alters the miscibility gap to such an extent that the AuPtRh alloys investigated remain dual phase up to melting, but the Rh does not alter the solidus temperature significantly. For the AuPt 70/30 at. % alloy it was expected that melting starts at 1220°C. For the AuPtRh 69/30/1 at. % alloy was found (Figure 29) that melting started at 1220°C. Likewise the AuPt 60/40 at. % alloy starts melting at 1260°C and the AuPtRh 59/40/1 at. % alloy was found (Figure 30) to start melting at 1270°C.

8. The stability of the Pt-rich phase is decreased by the presence of Pd, partially dissolved in the Pt-rich phase. The Pd is found to increase the melting temperature of the alloy considerably, for the additions investigated. Both studied AuPtPdRh alloys were found to be homogenisable. The start of the monophase temperature regions were found to be for the 54/27.5/17 alloy between 1270-1300°C and for the 44.5/37/17 alloy between 1350-1400°C. These temperatures are much higher (±250-300°C) than was expected in §1.4 on basis of the AuPtPd phase diagram. Again small additions of Rh increase the starting temperatures of the monophase temperature regions drastically. Comparison of this starting temperature found for the 54/27.5/17 alloy with the one for the 44.5/37/17 alloy indicates that the increase of the amount of Pt stabilises the Pt-rich phase.

References

1. AKZO internal classified reports: CDMI 92006, Report no. 91.60.262, 91.60.165, 88.60.133, and RO 374.1415, Arnhem, 1965-1992.
2. A.W.M. van den Hondel, *Strengthening Mechanisms in gold-platinum alloys*, TU Delft, Delft, 1993.
3. T.B. Massalski ed., *Binary Alloy Phase Diagrams*, ASM, Metals Park, 1986.
4. *Ternary Gold Alloy Phase Diagrams*, The Institute of Metals, London, 1990.
5. G.P. Zhmurko, E.M. Sokolovskaya a.o., *Vestniki Mosk. Univ. Series 2 Chemia 26*, 1985, (3), 324-325.
6. H.E. Boyer, *Hardness Testing*, ASM International, Metals Park, 1987.
7. M.A. Meyers, K.K. Chawla, *Mechanical Metallurgy - principles and applications*, Prentice-Hall, New Jersey Engelwood Cliffs, 1984.
8. I. LeMay, *Principles of Mechanical Metallurgy*, Edward Arnold, London, 1981.
9. F.R.N. Nabarro ed., *Dislocations in Solids Vol. 4*, North-Holland Publishing Company, Amsterdam, 1979.
10. P. Haasen, *Physical Metallurgy*, Cambridge University Press, Cambridge, 1978.
11. D. Peckner ed., *The Strengthening of Metals*, Reinhold Publishing Corporation, New York, 1964.
12. R. Labusch, *Crystal Lattice Defects Vol. 1*, 1969, 1-16.
13. R. Labusch, *Physica Status Solidi 41*, 1970, 659-669.
14. R. Labusch, *Acta Metallurgica 20*, 1972, 917-927.
15. R. Labusch, *Nuclear Metallurgy Vol. 20*, 1976, 650-657.
16. G.E. Dieter, *Mechanical Metallurgy*, McGraw-Hill, New York, 1976 (2ed edition).
17. R.W. Cahn, P. Haasen, *Physical Metallurgy*, third edition, North-Holland Physics Publishing, Amsterdam, 1983.
18. E. Orowan, *Internal Stresses in Metals and Alloys*, Institute of Metals, London, 1948.
19. A. van den Beukel, *Fysica vaste stof II*, Delft University of Technology, Delft, 1978.
20. S.I. Andersen a.o., *Constitutive relations and their physical basis*, Riso National Laboratory: International symposium on metallurgy and materials science, Roskilde, 1987.
21. Elephant internal report: *Onderzoek naar het effect van warmte behandeling op de Vickers hardheid bij Au/Pt/Rh en Au/Pt/Pd/Rh legeringen*, Hoorn, 1994.
22. Th. H. de Keijser, *On structures developed by spinodal decomposition*, Delft University Press, Delft, 1977.
23. R.L. Fogelson a.o., *Phys. Met. Metall. Vol. 46*, 1979, 163-164.

24. P. van Mourik, *Ageing of liquid-quenched and solid-quenched aluminium based alloys; analysis of lattice-parameter variations*, Delft University Press, Delft, 1988.

25. T. Lyman ed., *Metals Handbook 8th Edition Vol. 1*, ASM, Metals Park, 1961.

26. J.P. Cahoon a.o., *Metallurgical Transactions Vol. 2*, 1971, 1979-1983.

Appendix A: Statistics

Introduction

This appendix is not intended to give a thorough survey of statistics, but to give a general insight in the used statistics especially concerning appendix b where the hardness measurements are given. The two most important problems involving the treatment of experimental data are first that for any statistical analysis of data some sort of probability model for those data has to be assumed as basis and second that the unknown parameters of that assumed probability distribution have to be estimated from a limited number of experiments.

General Theory

The experiments conducted for this investigation are not deterministic, which means that not *all* conditions that fully determine the outcome of the experiment are known, and therefore the experiments are said to be random. In contrary to discrete variables, with a countable (even infinite) number of possible outcomes, the hardness variable has a specimen space that is continuous, that is where all possible real values in a certain interval may occur. This greatly reduces the statistics involved to those which are applicable for continuous variables.
A set of outcomes in the specimen space is called an event and it is said that an event occurs if any of the outcomes which comprise it occurs when the experiment is performed. The probability of an event is the expectancy that the event will occur. The probability of an event A, say, is a number P(A) satisfying certain conditions. Let B be any other event which has no outcome in common with A, that is A and B are disjoint sets of points. The conditions that must be satisfied by the numbers P(A) and P(B) are:

$$P(A) \geq 0 \text{ and } P(B) \geq 0 \qquad (A1)$$

$$P(A \cup B) = P(A) + P(B) \qquad (A2)$$

$$P(S) = 1 \qquad (A3)$$

where $A \cup B$ represents the union of the two sets, the set of all points belonging to A or B, and S stands for the whole specimen space. Basically these axioms are all that are needed for the statistical treatment of the measurements.

The experiments can be assumed to be independent, which means for two events A and B the probability that both occur, $P(A \cap B)$, equals the product of the probability of A and that of B

$$P(A \cap B) = P(A) \,.\, P(B) \qquad (A4)$$

Thus for independent experiments, usually called replicates, the probabilities of the different outcomes in any one performance are unaffected by the other outcomes.
For a continuous specimen space the realisations of a random variable are in principle continuous but in practice one experiences discrete distributions, due to the fact that one always makes measurements to a finite number of decimal places. An idealised situation where measurements are carried out to an infinite number of decimal places, would give a continuous distribution, but would give a probability of 0 (almost impossible events) for any particular value. To convert the continuous distribution to a discrete distribution the variable is divide in classes with a class with of dx and a probability of $P(x<X\leq x+dx)$, the probability of the event comprising of all outcomes for which X falls in the interval (x,x+dx) {the usual convention of using capital letters for random variables and small letters for realisations is adopted}. It is a convenient approximation to assume that the observations are in fact drawn from a continuous distribution.
If a random variable X is continuous, then the probability density f(x) is such that the integral of f(x) over any interval A gives the probability that X belongs to A gives the probability that X belongs to A

$$P(A) = \int_A f(x)dx \qquad (A5)$$

The probability of the simple event that X belongs to the interval (x,x+dx) is f(x)dx.
The probability density f(x) is normalised by

$$\int_{-\infty}^{\infty} f(x)dx = 1 \qquad (A6)$$

The distribution function of a random variable X is defined to be

$$F(x) = P(X \leq x) = \int_{-\infty}^{x} f(y)dy \qquad (A7)$$

The distribution mean of X, represented by the Greek letter μ, is defined as

$$\mu = \int_0^1 x dF(x) \qquad (A8)$$

The distribution variance of X, the Greek letter σ^2, is defined by

$$\sigma^2 = \int_0^1 (x-\mu)^2 dF(x) \qquad (A9)$$

The square root of the distribution variance is the distribution standard deviation, σ. Both σ^2 and σ afford measures of the spread of the distribution about the mean, σ being in the same units as X itself.
When an experiment is replicated n times producing independent, identically-distributed, observations we can define the specimen mean, m, and the specimen variance, s^2 (or equally well the specimen standard deviation s), by the equations

$$m = \sum \frac{X_i}{n} \qquad \text{and} \qquad (A10)$$

$$s^2 = \frac{\sum (X_i - m)^2}{n-1} \qquad (A11)$$

The normal distribution

This is the most important and widely used distribution in statistics, both directly for the distribution of continuous random variables, and as an approximation to any distribution for large n (continuous and discrete).
X is said to be normally distributed with mean μ and variance σ^2 if it has the (Gauss) probability density

$$f(x) = \frac{1}{\sqrt{2\pi\sigma^2}} \exp\left\{\frac{-(x-\mu)^2}{2\sigma^2}\right\} \qquad -\infty < x < \infty \qquad (A12)$$

This density is symmetric about μ, bell-shaped and almost coincides with the axis outside $\pm 3\sigma$.
The normal distribution is assumed to be the model for the observations in appendix b. This can be justified by two reasons: the normal distribution is found in practical experience to be appropriate for many types of physical measurements and other types of data, and because of the central limit and related theorems a great many statistics

used in statistical inference are approximately normally distributed for large specimen sizes, whatever the original distribution of the data.

Estimation

The two important parameters that characterise a normal distribution, μ and σ, cannot be obtained from a limited specimen of data. All that can be done is to estimate them. The mean μ is estimated by the specimens mean m. This estimation can be exactly calculated to be correct with a significance level 1-α, but therefore the populations σ should be known. The standard deviation of the population σ can on the other hand be estimated by the specimens standard deviation s. Of course the accuracy of this estimation is influenced by the specimens size n, for which a compensation factor is available: the Student distribution t. This opens the possibility of intrinsic determination of the possible error in the specimens mean. The error is given by

$$R = t_{\alpha/2}(n-1)\frac{s}{\sqrt{n}} \qquad \text{(A13)}$$

where t is the student factor with (n-1) degrees of freedom which can be taken from Table A1.

Table A1. Right critical values of the Student distribution.

(n-1) α	*0.05*	*0.025*	*0.005*
1	6.314	12.706	63.657
2	2.920	4.303	9.925
3	2.353	3.182	5.841
4	2.132	2.776	4.604
5	2.015	2.571	4.032
6	1.943	2.447	3.707
7	1.895	2.365	3.499
8	1.860	2.306	3.355
9	1.833	2.262	3.250
10	1.812	2.228	3.169
11	1.796	2.201	3.106
15	1.753	2.131	2.947
20	1.725	2.086	2.845
30	1.697	2.042	2.750
∞	1.645	1.960	2.576

Test on means

After having found R it is necessary compare two means of two specimens with normal distributions but with unknown variances on difference, i.e. are the two means really different ? The answer can be found by considering the one-sided situation corresponding to the two hypotheses

$$H_0 : \mu_1 = \mu_2 \qquad \text{and} \tag{A14}$$

$$H_1 : \mu_1 > \mu_2 \tag{A15}$$

For this the random variable T can be used

$$T = \frac{m_1 - m_2}{\sqrt{\frac{s_1^2}{n_1} + \frac{s_2^2}{n_2}}} \tag{A16}$$

Under H_0, T is approximately distributed as Student's t with ν degrees of freedom, given by

$$\frac{1}{\nu} = \frac{1}{n_1 - 1}\left(\frac{\frac{s_1^2}{n_1}}{\frac{s_1^2}{n_1} + \frac{s_2^2}{n_2}}\right)^2 + \frac{1}{n_2 - 1}\left(\frac{\frac{s_2^2}{n_2}}{\frac{s_1^2}{n_1} + \frac{s_2^2}{n_2}}\right)^2 \tag{A17}$$

H_0 is rejected at the significance level 1-α if the realisation of T is greater than or equal to $t_\alpha(\nu)$. This means that when

$$m_1 - m_2 \geq R_1 + R_2 \tag{A18}$$

H_0 is rejected at a significace level of 1-α or more.

Further information

For further reading the next two books are suggested:

1. J.R. Green, D. Margerison, *Statistical Treatment of Experimental Data*, Elsevier, Amsterdam, 1978.
2. J. van Soest, *Elementaire Statistiek*, DUM, Delft, 1992.

v. d Hondel

Strength Optimisation of
Au-Pt-base alloys

Theorie sterkte berekening

— oplossingshardning - geldt voor verdunde legeringen

Evenwichts samenstellingen niet bekend

— Precipitatie harding - twijfelachtig is of precipitatie harding optreedt (geen aanwijzingen hiervoor worden gevonden)

Mogelijk (waarschijnlijk) sprookje ontmaskering

Sommeren van oplossingshardings en precipitatie harding zondermeer is niet erg betrouwbaar

(Sommeren fractionele sterkte onbetrouwbaar)

Formule 51 p 83 m.i. onjuist

$$\bar{\sigma}_y = \left(1-f\right)\left(\bar{\sigma}_y^{Au} + 2\bar{\epsilon}_y^{55Au} + 2\bar{\epsilon}_y^{P}\right) + f\left(\bar{\sigma}_y^{Pt} + 2\bar{\epsilon}_y^{55Pt}\right)$$

de vraag voor σ_y is of laatste factor er bij moet deze is (gedeeltelijk) al opgenomen in prec. hardings factor

Dit geldt ook voor vergelijking 3g p 27

Wanneer er een mengsel is van Matrix en Fyne harde precipitaten dan is de $\bar{\sigma}_y$ van de legering gelijk aan σ_y van de matrix de additie regel

$$\bar{\sigma}_y = (1-f)\bar{\sigma}_y^{m} + f\bar{\sigma}_y^{p}$$

gaat dan zeker niet op

oplossingsharding

parelastic interaction – afmetingsverschil
legeringsatoom – matrixatoom

dielastic interaction – verschil in glijdingsmodulus
opgelost atoom – matrix atoom

parelastic

$\delta = \frac{a - a_0}{a_0} = f(c)$ c = concentratie opgelost atoom

$\delta = \frac{1+\nu}{3(1-\nu)} \frac{d\ln a}{dc} = \frac{1+\nu}{3(1-\nu)} \frac{1}{a} \frac{da}{dc}$

Interactiekracht $F^b_{max} = \eta b^2 \delta$ (per eenheid van dislocatie lengte?)

dielastic $\eta = \frac{d\ln \eta}{dc} = \frac{1}{\eta} \frac{d\eta}{dc} = \frac{2(\eta_s - \eta)}{(1+\alpha)\eta + (1-\alpha)\eta_s}$

η = η matrix, η_s = η opgelost stof

$\alpha = \frac{\nu - \frac{1}{3}}{3(1-\nu)} \sim 1/\eta$ $(\nu = 0{,}4)$

$F_d^{max} = \eta b^2 B \eta$ $B = \frac{1}{(1-\nu)^2 2\pi\sigma \frac{z}{b}}$ $z \sim b$

$B \sim \frac{1}{2\eta}$

$F^{eff}_{max} = \eta b^2 \sqrt{\delta^2 - \eta^2 B^2}$

geldt voor 1 atoom per eenheid van dislocatie lengte

$f(r)$ verdelingsfunctie interacties met kracht $F = \eta$

schuifspanning τ

τ_c = kritische schuifspanning om dislocatie te verplaatsen

$\tau b = \int f(F) F (dF) = \int S(\eta) \eta \, d\eta$

$\sigma_\eta = \frac{1,0}{3} H_v (0,1)^n$

$\sigma_\eta = 2,1 \; H_V$ voor $n \simeq 0,2$

$\sigma_\eta = 2,5 \; H_V$ voor $n = 0,12$

$\frac{0,68 - 0,85}{-0,75} \quad \frac{0,17}{0,75} =$

Appendix B: Hardness Measurements

All micro hardness measurements are done with the Vickers method. The measurements were done on a Leitz Durimet. The applied load is 100 grams which equals 981,0 mN or is otherwise explicitly given. The measured impression diameter is given as d in µm and the accompanying Vickers hardness as HV. Using the given data the specimens mean, m, the specimens standard deviation, s, and the error in m with a significance level of 95%, R, are given.

After rolling

The hardness profile measurements concerning the initial state after rolling for all four alloys are given in Tables B1-B4. Table B5 contains the measurements of the surface hardness after rolling.

Table B1 Hardness profile after rolling for AuPtRh 69/30 with a plate thickness D=0,844 mm.

Position		Measurements											m	s	R
40µm	d	39.0	39.2	37.5	37.1	39.1	38.9	40.0	39.0	40.0	39.3	39.2	122.6	5.9	4.0
	HV	122	121	132	135	121	123	116	122	116	120	121			
140µm	d	37	36.9	37.4	36	37.9	37.4	36.8	36.7	36.7	39.4	38.4	133.4	6.6	4.4
	HV	135	136	133	143	129	133	137	138	138	119	126			
240µm	d	35.5	36.1	36.4	36.6	36.5	35.0	35.9	35.9	35.2	33.4	35.2	146.5	7.9	5.3
	HV	147	142	140	138	139	151	144	144	150	166	150			
340µm	d	32.9	35.3	33.7	34.9	35.1	34.1	35.2	34.2	34.9	36.1	34.7	154.7	7.8	5.2
	HV	171	149	163	152	151	159	150	159	152	142	154			
440µm	d	34.1	33.8	34.9	34.3	35.0	33.8	33.8	33.2	33.6	35.1	35.5	157.8	6.6	4.4
	HV	159	162	152	158	151	162	162	168	164	151	147			

Table B2 Hardness profile after rolling for AuPtPdRh 54/27.5/17 with a plate thickness D=0,845 mm.

Position		Measurements											m	s	R
40µm	d	35.4	33.0	33.0	33.6	33.2	33.5	33.0	34.0	34.6	33.7	32.5	164.5	7.9	5.3
	HV	148	170	170	164	168	165	170	160	155	163	176			
140µm	d	30.8	32.9	30.6	33.1	32.5	32.6	32.8	32.9	34.5	33.0	32.3	175.5	11.8	7.9
	HV	195	171	198	169	176	174	172	171	156	170	178			
240µm	d	28.8	31.5	32.2	44.2	31.0	32.5	32.5	33.4	31.4	31.1	32.9	177.0	31.3	21.0
	HV	224	187	179	94.9	193	176	176	166	188	192	171			
340µm	d	31.6	30.9	30.6	32.3	30.9	31.1	31.4	31.8	31.4	33.1	31.3	187.2	8.2	5.5
	HV	186	194	198	178	194	192	188	183	188	169	189			
440µm	d	33.1	30.9	30.9	30.1	31.1	30.9	31.2	32.1	32.4	31.6	32.2	187.3	10.2	6.9
	HV	169	194	194	205	192	194	190	180	177	186	179			

Table B3 Hardness profile after rolling for AuPtRh 59/40 with a plate thickness D=0,633 mm.

Position		Measurements											m	s	R
40µm	d	34.6	33.8	34.1	36.8	36.0	35.2	33.6	33.9	34.6	34.2	34.9	154.3	8.3	5.6
	HV	155	162	159	137	143	150	164	161	155	159	152			
120µm	d	33.0	32.6	33.3	32.0	32.3	32.4	33.3	34.0	33.4	33.1	33.4	170.5	6.3	4.2
	HV	170	174	167	181	178	177	167	160	166	169	166			
200µm	d	33.4	32.9	32.5	40.0	32.5	32.4	32.3	33.8	32.5	33.2	33.4	166.5	17.6	11.8
	HV	166	171	176	116	176	177	178	162	176	168	166			
260µm	d	33.6	32.6	32.0	33.8	34.3	34.3	32.4	33.3	33.8	31.8	31.5	170.3	10.5	7.1
	HV	164	174	181	162	158	158	177	167	162	183	187			
320µm	d	32.7	32.6	33.2	33.4	31.2	33.6	33.3	33.7	32.3	33.4	34.1	169.8	8.6	5.8
	HV	173	174	168	166	190	164	167	163	178	166	159			

Table B4 Hardness profile after rolling for AuPtPdRh 44.5/37/17 with a plate thickness D=0,620 mm.

Position		Measurements											m	s	R
40µm	d	33.8	32.5	32.5	32.1	32.3	31.6	32.1	32.1	33.1	32.1	33.1	176.0	6.8	4.6
	HV	162	176	176	180	178	186	180	180	169	180	169			
120µm	d	33.0	31.2	30.9	31.1	30.6	31.0	31.9	30.4	31.4	30.2	32.5	189.7	10.2	6.9
	HV	170	190	194	192	198	193	182	201	188	203	176			
200µm	d	31.2	30.8	30.4	30.2	30.8	31.5	30.7	30.5	30.9	30.8	31.7	194.2	5.5	3.7
	HV	190	195	201	203	195	187	192	199	194	195	185			
260µm	d	31.4	29.9	32.3	29.6	30.5	31.3	30.8	29.8	30.4	34.3	31.0	193.5	15.5	10.4
	HV	188	207	178	212	199	189	195	209	201	158	193			
320µm	d	31.0	30.6	30.9	30.9	28.7	29.2	30.8	30.6	30.7	30.4	30.3	201.3	10.3	6.9
	HV	193	198	194	194	225	217	195	198	197	201	202			

Table B5 Surface hardness after rolling for AuPtRh 69/30 and AuPtPdRh 54/27.5/17.

Alloy		Measurements											m	s	R
70 / 30	d	36.4	36.6	38.0	37.0	36.2	36.0	36.1	36.1	36.6	36.7	36.6	138.5	4.3	2.9
	HV	140	138	128	135	142	143	142	142	138	138	138			
60 / 30	d	33.6	35.0	35.5	34.8	33.9	33.8	33.3	34.0	34.9	32.0	34.4	159.5	9.4	6.3
	HV	164	151	147	153	161	162	167	160	152	181	157			

Ageing after rolling

AuPtRh 69/30

The hardness measurements after rolling and ageing at various temperatures are given in: Tables B6-B31 for ageing at 400°C, Tables B32-B38 at 600°C and Tables B39-B46 at 700°C. Tables B29-B31 were sequentially treated, i.e. a specimen that was precipitated at 400°C for 2 hours for example (B29) was again treated at 400°C for 2 hours, making up a total of 4 hours at 400°C. This sequential measuring was done in order to verify the fluctuation in the hardness which was observed.

Table B6 Hardness near surface and in centre after rolling and aging for 30 minutes at T=400°C for AuPtRh 69/30 with a plate thickness D=0,8365 mm.

Position		Measurements										m	s	R
40µm	d	36.6	37.0	36.9	36.6	37.2	36.5	36.9	36.0	36.2	36.7	36.6	137.9	2.7	1.8
	HV	138	135	136	138	134	139	136	143	142	138	138			
418µm	d	35.8	35.6	35.7	35.5	36.0	35.6	35.5	35.6	35.1	35.3	35.0	147.0	2.4	1.6
	HV	145	146	146	147	143	146	147	146	151	149	151			

Table B7 Hardness near surface and in centre after rolling and aging for 1 hour at T=400°C for AuPtRh 69/30 with a plate thickness D=0,849 mm.

Position		Measurements										m	s	R
40µm	d	39.3	37.8	37.4	37.2	37.2	37.2	37.4	36.4	36.8	36.4	38.1	133.0	5.7	3.8
	HV	120	130	133	134	134	134	133	140	137	140	128			
160µm	d	36.3	37.4	37.0	37.5	36.8	36.6	38.5	36.5	36.6	36.8	36.4	135.9	4.5	3.0
	HV	141	133	135	132	137	138	125	139	138	137	140			
285µm	d	36.8	36.5	36.2	35.9	35.6	35.0	35.4	35.5	35.2	35.6	36.7	144.4	4.8	3.2
	HV	137	139	142	144	146	151	148	147	150	146	138			
425µm	d	35.8	36.0	35.8	34.4	35.0	34.7	34.9	34.6	34.3	34.8	34.3	151.9	5.4	3.6
	HV	145	143	145	157	151	154	152	155	158	153	158			

Table B8 Hardness near surface and in centre after rolling and aging for 1.5 hours at T=400°C for AuPtRh 69/30 with a plate thickness D=0,8735 mm.

Position		Measurements						m	s	R
40µm	d	33.6	35.2	37.1	35.1	35.3	34.9	150.2	9.2	9.7
	HV	164	150	135	151	149	152			
437µm	d	34.5	34.3	35.0	34.0	34.2	34.5	156.7	3.2	3.4
	HV	156	158	151	160	159	156			

Table B9 Hardness near surface and in centre after rolling and aging for 2 hours at T=400°C for AuPtRh 69/30 with a plate thickness D=0,813 mm.

Position		Measurements						m	s	R
40µm	d	36.5	35.6	35.7	36.8	35.1	35.0	145.0	5.9	6.2
	HV	139	146	146	137	151	151			
407µm	d	32.4	32.0	37.2	32.5	32.6	33.3	168.2	17.4	18.3
	HV	177	181	134	176	174	167			

Table B10 Hardness near surface and in centre after rolling and aging for 2.5 hours at T=400°C for AuPtRh 69/30 with a plate thickness D=0,800 mm.

Position		Measurements						m	s	R
40µm	d	32.1	32.8	32.3	32.4	32.5	32.5	176.5	2.7	2.8
	HV	180	172	178	177	176	176			
400µm	d	29.8	30.0	30.0	29.9	30.7	30.2	204.7	4.2	4.4
	HV	209	206	206	207	197	203			

Table B11 Hardness near surface and in centre after rolling and aging for 3 hours at T=400°C for AuPtRh 69/30 with a plate thickness D=0,800 mm.

Position		Measurements						m	s	R
40µm	d	34.4	34.0	34.2	33.9	40.0	35.0	150.7	17.4	18.3
	HV	157	160	159	161	116	151			
160µm	d	34.7	35.2	34.3	35.3	35.9	36.1	149.5	6.0	6.3
	HV	154	150	158	149	144	142			
280µm	d	35.1	34.3	34.8	35.3	35.0	35.0	152.2	3.1	3.3
	HV	151	158	153	149	151	151			
400µm	d	33.2	34.9	35.3	33.7	33.7	35.6	156.8	9.0	9.4
	HV	168	152	149	163	163	146			

Table B12 Hardness near surface and in centre after rolling and aging for 3.5 hours at T=400°C for AuPtRh 69/30 with a plate thickness D=0,837 mm.

Position		Measurements						m	s	R
40µm	d	33.1	34.6	32.4	33.2	32.9	33.2	168.0	7.2	7.6
	HV	169	155	177	168	171	168			
418µm	d	36.1	36.7	35.8	35.6	35.7	35.6	143.8	3.3	3.5
	HV	142	138	145	146	146	146			

Table B13 Hardness near surface and in centre after rolling and aging for 4 hours at T=400°C for AuPtRh 69/30 with a plate thickness D=0,845 mm.

Position		Measurements						m	s	R
40µm	d	38.0	36.8	37.2	37.0	38.5	37.7	131.5	4.6	4.8
	HV	128	137	134	135	125	130			
423µm	d	35.8	35.2	35.3	35.6	34.0	34.6	150.8	5.7	6.0
	HV	145	150	149	146	160	155			

Table B14 Hardness near surface and in centre after rolling and aging for 5 hours at T=400°C for AuPtRh 69/30 with a plate thickness D=0,8425 mm.

Position		Measurements						m	s	R
40µm	d	37.0	36.9	36.2	35.9	37.8	37.0	137.0	5.1	5.4
	HV	135	136	142	144	130	135			
421µm	d	34.3	33.8	33.1	33.9	33.4	33.5	163.5	3.9	4.1
	HV	158	162	169	161	166	165			

Table B15 Hardness near surface and in centre after rolling and aging for 6.083 hours at T=400°C for AuPtRh 69/30 with a plate thickness D=0,831 mm.

Position		Measurements						m	s	R
40µm	d	36.5	36.0	36.3	35.3	36.3	36.8	141.7	4.1	4.3
	HV	139	143	141	149	141	137			
160µm	d	37.7	36.5	36.9	41.3	36.8	36.8	131.3	11.4	12.0
	HV	130	139	136	109	137	137			
280µm	d	34.4	34.7	40.0	35.8	34.4	34.3	147.8	16.3	17.1
	HV	157	154	116	145	157	158			
416µm	d	34.8	40.0	34.9	34.6	33.9	33.6	150.2	17.4	18.3
	HV	153	116	152	155	161	164			

Table B16 Hardness near surface and in centre after rolling and aging for 7 hours at T=400°C for AuPtRh 69/30 with a plate thickness D=0,655 mm.

Position		Measurements						m	s	R
40µm	d	34.3	33.6	34.0	33.5	33.5	33.8	162.3	2.9	3.0
	HV	158	164	160	165	165	162			
328µm	d	31.9	32.4	32.2	31.7	30.9	31.0	185.3	6.7	7.0
	HV	182	178	180	185	194	193			

Table B17 Hardness near surface and in centre after rolling and aging for 8 hours at T=400°C for AuPtRh 69/30 with a plate thickness D=0,781 mm.

Position		Measurements						m	s	R
40µm	d	36.2	36.4	36.7	36.4	40.0	37.2	135.0	9.7	10.2
	HV	142	140	138	140	116	134			
160µm	d	35.4	34.5	34.2	33.1	34.4	33.8	158.5	6.9	7.2
	HV	148	156	159	169	157	162			
280µm	d	34.5	34.8	34.8	32.9	33.3	33.3	161.2	8.1	8.5
	HV	156	153	153	171	167	167			
391µm	d	34.5	34.3	33.1	32.8	32.9	33.4	165.3	6.8	7.1
	HV	156	158	169	172	171	166			

Table B18 Hardness near surface and in centre after rolling and aging for 10 hours at T=400°C for AuPtRh 69/30 with a plate thickness D=0,830 mm.

Position		Measurements						m	s	R
40µm	d	34.8	34.2	34.5	33.8	34.6	34.4	157.0	3.2	3.4
	HV	153	159	156	162	155	157			
415µm	d	36.0	35.7	36.0	35.5	35.4	33.7	148.3	7.5	7.9
	HV	143	146	143	147	148	163			

Table B19 Hardness near surface and in centre after rolling and aging for 12 hours at T=400°C for AuPtRh 69/30 with a plate thickness D=0,800 mm.

Position		Measurements						m	s	R
40µm	d	37.2	36.6	36.7	36.9	36.0	36.1	138.5	3.4	3.6
	HV	134	138	138	136	143	142			
400µm	d	34.0	33.9	34.7	34.4	34.8	35.3	155.7	4.5	4.7
	HV	160	161	154	157	153	149			

Table B20 Hardness near surface and in centre after rolling and aging for 14 hours at T=400°C for AuPtRh 69/30 with a plate thickness D=0,814 mm.

Position		Measurements						m	s	R
40µm	d	32.5	33.1	34.3	33.8	34.8	33.6	163.7	8.1	8.5
	HV	176	169	158	162	153	164			
407µm	d	33.1	34.6	33.5	33.7	34.4	34.8	160.3	6.3	6.6
	HV	169	155	165	163	157	153			

Table B21 Hardness near surface and in centre after rolling and aging for 16.25 hours at T=400°C for AuPtRh 69/30 with a plate thickness D=0,800 mm.

Position		Measurements						m	s	R
40µm	d	34.1	34.3	35.6	35.1	35.1	34.7	153.2	4.9	5.1
	HV	159	158	146	151	151	154			
160µm	d	34.8	34.5	36.5	33.5	34.3	33.7	155.7	9.3	9.8
	HV	153	156	139	165	158	163			
280µm	d	33.2	32.7	33.4	32.5	34.0	33.5	168.0	5.8	6.1
	HV	168	173	166	176	160	165			
400µm	d	31.8	32.9	31.8	31.9	33.0	32.2	178.0	6.0	6.3
	HV	183	171	183	182	170	179			

Table B22 Hardness near surface and in centre after rolling and aging for 18 hours at T=400°C for AuPtRh 69/30 with a plate thickness D=0,800 mm.

Position		Measurements						m	s	R
40µm	d	36.3	36.6	37.6	38.3	38.3	38.4	131.3	6.7	7.0
	HV	141	138	131	126	126	126			
400µm	d	34.8	35.9	35.2	34.8	35.4	35.0	149.8	3.4	3.6
	HV	153	144	150	153	148	151			

Table B23 Hardness near surface and in centre after rolling and aging for 20 hours at T=400°C for AuPtRh 69/30 with a plate thickness D=0,8135 mm.

Position		Measurements												m	s	R
40µm	d	29.5	29.6	30.0	30.2	30.2	29.5	30.4	30.3	29.8	28.9	30.4	31.3	206.2	8.4	5.3
	HV	213	212	206	203	203	213	201	202	209	222	201	189			
407µm	d	33.4	34.0	32.3	33.4	32.5	32.8	33.6	33.3	33.6	33.5	33.7	34.1	166.7	5.9	3.7
	HV	166	160	178	166	176	172	164	167	164	165	163	159			

Table B24 Hardness near surface and in centre after rolling and aging for 22 hours at T=400°C for AuPtRh 69/30 with a plate thickness D=0,800 mm.

Position		Measurements						m	s	R
40µm	d	34.6	33.4	32.3	32.7	33.9	34.2	165.3	8.8	9.2
	HV	155	166	178	173	161	159			
400µm	d	33.8	33.9	34.3	34.3	34.5	34.3	158.8	2.2	2.3
	HV	162	161	158	158	156	158			

Table B25 Hardness near surface and in centre after rolling and aging for 24 hours at T=400°C for AuPtRh 69/30 with a plate thickness D=0,800 mm.

Position		Measurements						m	s	R
40µm	d	34.9	32.8	34.8	33.6	35.1	33.9	158.8	8.3	8.7
	HV	152	172	153	164	151	161			
160µm	d	33.8	32.8	32.3	31.9	32.7	32.8	173.2	6.8	7.1
	HV	162	172	178	182	173	172			
280µm	d	32.8	32.3	32.0	32.4	32.3	32.1	177.7	3.1	3.3
	HV	172	178	181	177	178	180			
400µm	d	31.4	30.4	32.1	31.1	30.8	30.4	192.8	8.1	8.5
	HV	188	201	180	192	195	201			

Table B26 Hardness near surface and in centre after rolling and aging for 26 hours at T=400°C for AuPtRh 69/30 with a plate thickness D=0,8525 mm.

Position		Measurements										m	s	R
40µm	d	37.5	37.9	37.2	37.4	37.3	36.9	36.8	37.7	36.7	37.0	36.5	134.2	3.2	2.1
	HV	132	129	134	133	133	136	137	130	138	135	139			
426µm	d	35.0	34.3	34.9	34.6	35.8	35.3	34.5	36.2	34.5	35.3	35.2	151.2	4.9	3.3
	HV	151	158	152	155	145	149	156	142	156	149	150			

Table B27 Hardness near surface and in centre after rolling and aging for 28 hours at T=400°C for AuPtRh 69/30 with a plate thickness D=0,793 mm.

Position		Measurements						m	s	R
40µm	d	35.1	34.3	34.6	35.4	34.4	34.6	154.0	3.8	4.0
	HV	151	158	155	148	157	155			
397µm	d	34.9	34.6	34.0	34.0	34.8	33.5	157.5	5.0	5.2
	HV	152	155	160	160	153	165			

Table B28 Hardness near surface and in centre after rolling and aging for 46 hours at T=400°C for AuPtRh 69/30 with a plate thickness D=0,845 mm.

Position		Measurements						m	s	R
40µm	d	36.4	37.2	36.8	36.9	36.8	37.4	136.2	2.5	2.6
	HV	140	134	137	136	137	133			
420µm	d	34.8	35.3	35.9	35.0	36.7	35.3	147.3	5.5	5.8
	HV	153	149	144	151	138	149			

Table B29 Hardness near surface and in centre after rolling and aging for 2+2 hours at T=400°C for AuPtRh 69/30 with a plate thickness D=0,745 mm.

Position		Measurements						m	s	R
40µm	d	32.3	33.2	33.9	34.7	34.1	34.0	163.3	8.5	8.9
	HV	178	168	161	154	159	160			
373µm	d	35.9	34.8	34.8	34.3	35.1	34.8	152.0	4.6	4.8
	HV	144	153	153	158	151	153			

Table B30 Hardness near surface and in centre after rolling and aging for 7+1 hours at T=400°C for AuPtRh 69/30 with a plate thickness D=0,848 mm.

Position		Measurements						m	s	R
40µm	d	36.0	35.6	35.9	36.8	34.9	36.8	143.2	5.7	6.0
	HV	143	146	144	137	152	137			
424µm	d	35.8	35.2	34.6	35.5	35.3	35.3	149.2	3.4	3.6
	HV	145	150	155	147	149	149			

Table B31 Hardness near surface and in centre after rolling and aging for 16.25+1.75 hours at T=400°C for AuPtRh 69/30 with a plate thickness D=0,838 mm.

Position		Measurements						m	s	R
40µm	d	33.3	32.6	33.5	33.7	33.5	33.3	166.8	3.8	4.0
	HV	167	174	165	163	165	167			
419µm	d	34.6	34.7	34.7	34.5	35.7	35.1	152.7	3.7	3.9
	HV	155	154	154	156	146	151			

Table B32 Hardness near surface and in centre after rolling and aging for 30 minutes at T=600°C for AuPtRh 69/30 with a plate thickness D=0,8665 mm.

Position		Measurements						m	s	R
40µm	d	29.0	29.0	29.3	28.6	29.6	31.0	215.0	11.9	12.5
	HV	221	221	216	227	212	193			
433µm	d	29.8	30.0	30.9	31.6	31.6	30.8	196.0	9.7	10.2
	HV	209	206	194	186	186	195			

Table B33 Hardness near surface and in centre after rolling and aging for 1 hour at T=600°C for AuPtRh 69/30 with a plate thickness D=0,800 mm.

Position		Measurements						m	s	R
40µm	d	27.5	28.2	27.7	27.6	27.5	29.0	238.2	9.5	10.0
	HV	245	233	242	243	245	221			
400µm	d	27.4	27.2	27.6	27.0	26.8	27.1	251.0	5.3	5.6
	HV	247	251	243	254	258	253			

Table B34 Hardness near surface and in centre after rolling and aging for 1.5 hours at T=600°C for AuPtRh 69/30 with a plate thickness D=0,838 mm.

Position		Measurements						m	s	R
40µm	d	29.1	28.5	28.6	29.2	30.1	28.3	221.3	9.8	10.3
	HV	219	228	227	217	205	232			
419µm	d	27.3	27.1	27.0	27.5	27.2	27.2	250.5	3.2	3.4
	HV	249	253	254	245	251	251			

Table B35 Hardness near surface and in centre after rolling and aging for 2 hours at T=600°C for AuPtRh 69/30 with a plate thickness D=0,820 mm.

Position		Measurements						m	s	R
40µm	d	28.3	28.0	28.1	28.0	28.5	28.1	234.0	3.5	3.7
	HV	232	237	235	237	228	235			
410µm	d	27.0	27.0	26.7	27.6	27.5	27.0	251.7	6.4	6.7
	HV	254	254	260	243	245	254			

Table B36 Hardness near surface and in centre after rolling and aging for 2.583 hours at T=600°C for AuPtRh 69/30 with a plate thickness D=0,824 mm.

Position		Measurements						m	s	R
40µm	d	31.0	28.6	28.9	29.7	30.4	30.7	208.3	13.8	14.5
	HV	193	227	222	210	201	197			
412µm	d	28.5	29.3	29.5	28.3	28.1	28.9	224.3	8.8	9.2
	HV	228	216	213	232	235	222			

Table B37 Hardness near surface and in centre after rolling and aging for 3 hours at T=600°C for AuPtRh 69/30 with a plate thickness D=0,857 mm.

Position		Measurements						m	s	R
40µm	d	28.2	29.5	29.9	29.5	29.9	29.9	213.3	10.1	10.6
	HV	233	213	207	213	207	207			
429µm	d	29.3	29.0	28.5	30.9	29.3	28.7	216.7	12.1	12.7
	HV	216	221	228	194	216	225			

Table B38 Hardness near surface and in centre after rolling and aging for 4 hours at T=600°C for AuPtRh 69/30 with a plate thickness D=0,838 mm.

Position		Measurements						m	s	R
40µm	d	31.1	30.2	30.9	30.4	30.9	31.0	196.2	4.6	4.8
	HV	192	203	194	201	194	193			
419µm	d	31.5	29.9	30.2	31.5	30.4	30.8	196.7	8.4	8.8
	HV	187	207	203	187	201	195			

Table B39 Hardness near surface and in centre after rolling and aging for 10 minutes at T=700°C for AuPtRh 69/30 with a plate thickness D=0,842 mm.

Position		Measurements						m	s	R
40µm	d	30.8	32.7	30.2	31.6	31.0	32.5	187.7	11.6	12.2
	HV	195	173	203	186	193	176			
421µm	d	27.7	28.5	28.7	29.6	29.0	28.2	226.8	10.3	10.8
	HV	242	228	225	212	221	233			

Table B40 Hardness near surface and in centre after rolling and aging for 30 minutes at T=700°C for AuPtRh 69/30 with a plate thickness D=0,860 mm.

Position		Measurements						m	s	R
40µm	d	31.4	30.0	31.4	30.2	29.7	30.9	198.2	9.5	10.0
	HV	188	206	188	203	210	194			
430µm	d	29.7	29.3	29.8	28.4	29.6	29.2	215.7	7.7	8.1
	HV	210	216	209	230	212	217			

Table B41 Hardness near surface and in centre after rolling and aging for 45 minutes at T=700°C for AuPtRh 69/30 with a plate thickness D=0,865 mm.

Position		Measurements						m	s	R
40µm	d	33.5	32.0	32.0	32.4	31.1	31.7	180.2	9.0	9.4
	HV	165	181	181	177	192	185			
432µm	d	32.4	31.4	31.3	32.1	31.6	31.5	184.5	4.8	5.0
	HV	177	188	189	180	186	187			

Table B42 Hardness near surface and in centre after rolling and aging for 1 hour at T=700°C for AuPtRh 69/30 with a plate thickness D=0,825 mm.

Position		Measurements						m	s	R
40µm	d	31.7	32.2	32.9	32.6	33.1	33.1	174.5	6.4	6.7
	HV	185	179	171	174	169	169			
410µm	d	30.6	30.2	31.0	30.7	30.7	30.3	198.3	3.7	3.9
	HV	198	203	193	197	197	202			

Table B43 Hardness near surface and in centre after rolling and aging for 1.5 hours at T=700°C for AuPtRh 69/30 with a plate thickness D=0,856 mm.

Position		Measurements						m	s	R
40µm	d	33.9	33.7	34.1	33.9	34.2	35.4	158.5	5.4	5.7
	HV	161	163	159	161	159	148			
428µm	d	32.3	32.8	32.5	32.6	31.5	31.6	178.8	6.3	6.6
	HV	178	172	176	174	187	186			

Table B44 Hardness near surface and in centre after rolling and aging for 2 hours at T=700°C for AuPtRh 69/30 with a plate thickness D=0,789 mm.

Position		Measurements						m	s	R
40µm	d	32.9	34.3	33.8	33.6	34.1	34.0	162.3	4.8	5.0
	HV	171	158	162	164	159	160			
395µm	d	32.6	32.7	31.8	31.8	33.2	32.6	175.8	6.0	6.3
	HV	174	173	183	183	168	174			

Table B45 Hardness near surface and in centre after rolling and aging for 2.5 hours at T=700°C for AuPtRh 69/30 with a plate thickness D=0,817 mm.

Position		Measurements						m	s	R
40µm	d	32.8	33.2	33.1	33.3	34.0	33.6	166.7	4.2	4.4
	HV	172	168	169	167	160	164			
409µm	d	32.2	31.7	32.2	33.0	32.6	33.0	176.2	5.9	6.2
	HV	179	185	179	170	174	170			

Table B46 Hardness near surface and in centre after rolling and aging for 3 hours at T=700°C for AuPtRh 69/30 with a plate thickness D=0,890 mm.

Position		Measurements						m	s	R
40µm	d	33.9	32.7	34.0	34.8	34.7	34.1	160.0	7.2	7.6
	HV	161	173	160	153	154	159			
445µm	d	32.1	33.0	32.5	33.3	32.3	32.8	173.8	5.0	5.2
	HV	180	170	176	167	178	172			

AuPtPdRh 54/27.5/17

The hardness measurements after rolling and ageing at various temperatures are given in: Tables B47-B72 for ageing at 400°C, Tables B73-B79 at 600°C and Tables B80-B87 at 700°C. Tables B70-B72 were sequentially treated, i.e. a specimen that was precipitated at 400°C for 2 hours for example (B72) was again treated at 400°C for 2 hours, making up a total of 4 hours at 400°C. This sequential measuring was done in order to verify the fluctuation in the hardness which was observed.

Table B47 Hardness near surface and in centre after rolling and aging for 30 minutes at T=400°C for AuPtPdRh 54/27.5/17 with a plate thickness D=0,7935 mm.

Position		Measurements										m	s	R
40µm	d	33.7	32.8	32.7	32.5	31.5	31.3	30.2	31.1	31.2	36.2	31.5	179.5	16.8	11.3
	HV	163	172	173	176	187	189	203	192	190	142	187			
397µm	d	30.9	30.6	30.8	30.9	30.5	30.8	30.2	30.0	31.0	30.4	31.3	197.0	4.9	3.3
	HV	194	198	195	194	199	195	203	206	193	201	189			

Table B48 Hardness near surface and in centre after rolling and aging for 1 hour at T=400°C for AuPtPdRh 54/27.5/17 with a plate thickness D=0,886 mm.

Position		Measurements											m	s	R
40µm	d	32.6	32.4	33.6	32.4	32.1	33.4	34.3	33.4	33.2	33.4	32.9	169.7	6.7	4.5
	HV	174	177	164	177	180	166	158	166	168	166	171			
180µm	d	31.6	32.0	32.0	31.1	31.7	32.3	31.1	32.2	32.2	32.0	31.7	183.5	4.9	3.3
	HV	186	181	181	192	185	178	192	179	179	181	185			
320µm	d	30.7	31.3	30.3	31.2	30.3	30.9	30.6	30.6	30.9	34.3	31.6	191.6	12.3	8.3
	HV	197	189	202	190	202	194	198	198	194	158	186			
443µm	d	30.7	30.7	31.1	30.6	30.8	30.9	31.0	30.1	30.3	30.3	30.4	197.8	4.2	2.8
	HV	197	197	192	198	195	194	193	205	202	202	201			

Table B49 Hardness near surface and in centre after rolling and aging for 1.5 hours at T=400°C for AuPtPdRh 54/27.5/17 with a plate thickness D=0,900 mm.

Position		Measurements						m	s	R
40µm	d	32.5	35.9	32.7	32.8	32.6	33.0	168.2	12.0	12.6
	HV	176	144	173	172	174	170			
450µm	d	29.9	30.0	30.2	30.1	29.9	29.8	206.2	2.0	2.1
	HV	207	206	203	205	207	209			

Table B50 Hardness near surface and in centre after rolling and aging for 2 hours at T=400°C for AuPtPdRh 54/27.5/17 with a plate thickness D=0,790 mm.

Position		Measurements						m	s	R
40µm	d	30.8	30.8	30.1	30.2	29.5	30.0	202.8	6.9	7.2
	HV	195	195	205	203	213	206			
395µm	d	29.4	29.1	29.3	29.2	29.1	28.9	218.0	2.5	2.6
	HV	215	219	216	217	219	222			

Table B51 Surface hardness after rolling and aging for 2.5 hours at T=400°C for AuPtPdRh 54/27.5/17.

Position		Measurements						m	s	R
surface	d	31.0	30.8	30.8	30.9	30.8	30.7	194.8	1.3	1.4
	HV	193	195	195	194	195	197			

Table B52 Hardness near surface and in centre after rolling and aging for 3 hours at T=400°C for AuPtPdRh 54/27.5/17 with a plate thickness D=0,800 mm.

Position		Measurements						m	s	R
40µm	d	32.7	32.3	31.7	31.8	31.6	31.8	181.3	4.9	5.1
	HV	173	178	185	183	186	183			
160µm	d	30.0	30.4	31.0	31.0	31.6	30.8	195.7	7.0	7.3
	HV	206	201	193	193	186	195			
280µm	d	30.7	29.9	30.8	29.8	29.6	29.5	205.5	7.7	8.1
	HV	197	207	195	209	212	213			
400µm	d	29.6	30.1	29.9	29.5	29.8	30.7	207.2	5.8	6.1
	HV	212	205	207	213	209	197			

Table B53 Hardness near surface and in centre after rolling and aging for 3.5 hours at T=400°C for AuPtPdRh 54/27.5/17 with a plate thickness D=0,820 mm.

Position		Measurements						m	s	R
40µm	d	32.9	32.2	34.3	32.7	32.5	33.8	169.8	8.2	8.6
	HV	171	179	158	173	176	162			
410µm	d	30.4	30.0	30.5	29.8	29.7	30.8	203.3	6.0	6.3
	HV	201	206	199	209	210	195			

Table B54 Hardness near surface and in centre after rolling and aging for 4 hours at T=400°C for AuPtPdRh 54/27.5/17 with a plate thickness D=0,800 mm.

Position		Measurements						m	s	R
40µm	d	32.3	32.1	31.8	32.3	31.6		181.0	3.5	4.3
	HV	178	180	183	178	186				
400µm	d	30.7	30.3	30.6	30.3	30.6	30.0	200.5	3.4	3.6
	HV	197	202	198	202	198	206			

Table B55 Surface hardness after rolling and aging for 5 hours at T=400°C for AuPtPdRh 54/27.5/17.

Position		Measurements						m	s	R
surface	d	30.0	29.3	29.4	29.5	29.8	28.7	214.0	6.6	6.9
	HV	206	216	215	213	209	225			

Table B56 Hardness near surface and in centre after rolling and aging for 6.083 hours at T=400°C for AuPtPdRh 54/27.5/17 with a plate thickness D=0,8625 mm.

Position		Measurements						m	s	R
40µm	d	31.3	31.8	30.8	31.3	32.0	32.1	186.2	5.8	6.1
	HV	189	183	195	189	181	180			
160µm	d	28.9	30.1	29.8	29.4	30.5	30.3	208.7	8.6	9.0
	HV	222	205	209	215	199	202			
280µm	d	28.7	29.3	28.4	29.1	28.9	29.1	221.8	5.0	5.2
	HV	225	216	230	219	222	219			
431µm	d	28.3	28.4	28.9	29.3	29.6	29.3	221.3	8.2	8.6
	HV	232	230	222	216	212	216			

Table B57 Hardness near surface and in centre after rolling and aging for 7 hours at T=400°C for AuPtPdRh 54/27.5/17 with a plate thickness D=0,7875 mm.

Position		Measurements						m	s	R
40µm	d	30.6	29.8	29.6	30.0	29.7	29.1	209.0	6.9	7.2
	HV	198	209	212	206	210	219			
394µm	d	27.1	27.1	27.2	26.3	26.5	26.9	257.5	6.9	7.2
	HV	253	253	251	268	264	256			

Table B58 Hardness near surface and in centre after rolling and aging for 8 hours at T=400°C for AuPtPdRh 54/27.5/17 with a plate thickness D=0,800 mm (the edge was located on 0,808 mm).

Position		Measurements						m	s	R
40µm	d	31.5	31.3	32.0	32.2	32.4	33.1	180.3	7.2	7.6
	HV	187	189	181	179	177	169			
160µm	d	29.4	29.8	29.3	30.4	30.6	30.6	206.2	8.3	8.7
	HV	215	209	216	201	198	198			
280µm	d	30.8	31.1	30.9	31.2	30.8	30.0	195.3	5.6	5.9
	HV	195	192	194	190	195	206			
400µm	d	30.0	31.5	31.4	31.3	30.9	30.9	193.0	7.0	7.3
	HV	206	187	188	189	194	194			
520µm	d	30.8	31.2	30.3	30.5	31.0	31.8	193.7	6.7	7.0
	HV	195	190	202	199	193	183			
640µm	d	31.0	31.4	30.6	30.7	31.2	30.7	193.8	4.2	4.4
	HV	193	188	198	197	190	197			
760µm	d	33.4	33.4	33.2	34.1	33.0	34.3	164.5	4.9	5.1
	HV	166	166	168	159	170	158			

Table B59 Hardness near surface and in centre after rolling and aging for 10 hours at T=400°C for AuPtPdRh 54/27.5/17 with a plate thickness D=0,781 mm.

Position		Measurements						m	s	R
40µm	d	30.9	31.2	31.9	33.7	32.3	32.5	180.5	11.0	11.5
	HV	194	190	182	163	178	176			
390µm	d	28.8	29.2	29.2	28.9	28.9	29.5	219.2	4.2	4.4
	HV	224	217	217	222	222	213			

Table B60 Hardness near surface and in centre after rolling and aging for 12 hours at T=400°C for AuPtPdRh 54/27.5/17 with a plate thickness D=0,784 mm.

Position		Measurements						m	s	R
40µm	d	31.5	31.4	31.5	31.7	31.5	31.3	187.2	1.3	1.4
	HV	187	188	187	185	187	189			
392µm	d	29.2	29.2	29.7	29.8	29.8	29.3	213.0	4.0	4.2
	HV	217	217	210	209	209	216			

Table B61 Hardness near surface and in centre after rolling and aging for 14 hours at T=400°C for AuPtPdRh 54/27.5/17 with a plate thickness D=0,7825 mm.

Position		Measurements						m	s	R
40µm	d	29.3	29.7	29.0	29.1	29.3	28.3	219.0	7.4	7.8
	HV	216	210	221	219	216	232			
391µm	d	27.9	27.9	28.5	28.4	28.7	28.2	232.0	5.3	5.6
	HV	238	238	228	230	225	233			

Table B62 Hardness near surface and in centre after rolling and aging for 16.25 hours at T=400°C for AuPtPdRh 54/27.5/17 with a plate thickness D=0,8175 mm.

Position		Measurements						m	s	R
40µm	d	26.8	28.3	27.2	27.5	27.0	27.1	248.8	9.3	9.8
	HV	258	232	251	245	254	253			
160µm	d	26.8	27.2	27.9	27.6	32.8	27.4	234.8	31.5	33.1
	HV	258	251	238	243	172	247			
280µm	d	27.8	28.1	27.8	27.3	26.6	28.1	243.5	10.4	10.9
	HV	240	235	240	249	262	235			
409µm	d	28.4	28.3	28.6	28.1	28.0	28.2	232.3	3.6	3.8
	HV	230	232	227	235	237	233			

Table B63 Hardness near surface and in centre after rolling and aging for 18 hours at T=400°C for AuPtPdRh 54/27.5/17 with a plate thickness D=0,800 mm.

Position		Measurements						m	s	R
40µm	d	31.9	32.0	31.9	32.1	32.6	32.1	179.8	3.0	3.1
	HV	182	181	182	180	174	180			
400µm	d	29.2	29.5	29.1	28.6	29.1	29.9	217.0	6.7	7.0
	HV	217	213	219	227	219	207			

Table B64 Hardness near surface and in centre after rolling and aging for 20 hours at T=400°C for AuPtPdRh 54/27.5/17 with a plate thickness D=0,8615 mm.

Position		Measurements						m	s	R
40µm	d	30.7	30.4	30.6	30.8	31.1	30.8	196.3	3.1	3.3
	HV	197	201	198	195	192	195			
431µm	d	27.8	27.0	28.7	27.6	28.6	28.6	236.0	11.6	12.2
	HV	240	254	225	243	227	227			

Table B65 Hardness near surface and in centre after rolling and aging for 22 hours at T=400°C for AuPtPdRh 54/27.5/17 with a plate thickness D=0,785 mm.

Position		Measurements						m	s	R
40µm	d	29.4	29.8	29.7	29.7	29.1	29.5	212.7	3.8	4.0
	HV	215	209	210	210	219	213			
393µm	d	28.0	28.8	28.6	28.0	28.4	28.4	230.8	5.3	5.6
	HV	237	224	227	237	230	230			

Table B66 Hardness near surface and in centre after rolling and aging for 24 hours at T=400°C for AuPtPdRh 54/27.5/17 with a plate thickness D=0,800 mm.

Position		Measurements						m	s	R
40µm	d	29.3	28.7	29.3	29.6	29.0	29.2	217.8	4.5	4.7
	HV	216	225	216	212	221	217			
160µm	d	26.4	26.9	27.2	26.6	26.8	27.2	257.3	6.0	6.3
	HV	266	256	251	262	258	251			
280µm	d	27.3	27.8	27.8	27.4	27.9	27.1	244.5	6.0	6.3
	HV	249	240	240	247	238	253			
400µm	d	27.8	27.6	27.0	28.1	26.9	28.0	244.2	8.8	9.2
	HV	240	243	254	235	256	237			

Table B67 Hardness near surface and in centre after rolling and aging for 26 hours at T=400°C for AuPtPdRh 54/27.5/17 with a plate thickness D=0,800 mm.

Position		Measurements										m	s	R
40µm	d	34.5	33.0	32.6	32.9	33.6	32.8	32.3	31.5	32.3	32.2	31.3	174.4	9.5	6.4
	HV	156	170	174	171	164	172	178	187	178	179	189			
400µm	d	29.0	28.3	28.5	29.1	28.6	29.0	30.5	29.0	28.3	28.8	28.7	222.6	9.0	6.0
	HV	221	232	228	219	227	221	199	221	232	224	225			

Table B68 Hardness near surface and in centre after rolling and aging for 28 hours at T=400°C for AuPtPdRh 54/27.5/17 with a plate thickness D=0,793 mm.

Position		Measurements						m	s	R
40µm	d	29.5	29.9	30.4	30.9	30.6	31.0	201.0	7.8	8.2
	HV	213	207	201	194	198	193			
397µm	d	29.9	30.3	30.4	30.6	30.0	29.9	203.5	3.7	3.9
	HV	207	202	201	198	206	207			

Table B69 Hardness near surface and in centre after rolling and aging for 46 hours at T=400°C for AuPtPdRh 54/27.5/17 with a plate thickness D=0,8135 mm.

Position		Measurements						m	s	R
40µm	d	32.8	32.8	32.5	33.0	33.5	32.5	171.8	4.1	4.3
	HV	172	172	176	170	165	176			
407µm	d	29.1	29.6	29.8	29.0	29.6	29.5	214.3	4.6	4.8
	HV	219	212	209	221	212	213			

Table B70 Hardness near surface and in centre after rolling and aging for 2+2 hours at T=400°C for AuPtPdRh 54/27.5/17 with a plate thickness D=0,672 mm.

Position		Measurements						m	s	R
40µm	d	28.9	28.9	28.9	29.0	28.3	28.2	225.3	5.6	5.9
	HV	222	222	222	221	232	233			
336µm	d	30.5	29.8	30.7	30.4	30.2	30.5	201.3	4.3	4.5
	HV	199	209	197	201	203	199			

Table B71 Hardness near surface and in centre after rolling and aging for 7+1 hours at T=400°C for AuPtPdRh 54/27.5/17 with a plate thickness D=0,822 mm.

Position		Measurements						m	s	R
40µm	d	30.9	30.2	30.1	30.7	31.3	32.1	194.7	9.3	9.8
	HV	194	203	205	197	189	180			
411µm	d	29.4	29.6	29.5	29.5	29.5	29.3	213.7	1.5	1.6
	HV	215	212	213	213	213	216			

Table B72 Hardness near surface and in centre after rolling and aging for 16.25+1.75 hours at T=400°C for AuPtPdRh 54/27.5/17 with a plate thickness D=0,770 mm.

Position		Measurements						m	s	R
40µm	d	28.9	29.9	30.1	30.0	29.7	29.6	210.3	6.3	6.6
	HV	222	207	205	206	210	212			
385µm	d	28.5	28.4	28.5	28.3	27.9	28.6	230.5	4.1	4.3
	HV	228	230	228	232	238	227			

Table B73 Hardness near surface and in centre after rolling and aging for 30 minutes at T=600°C for AuPtPdRh 54/27.5/17 with a plate thickness D=0,7825 mm.

Position		Measurements						m	s	R
40µm	d	26.4	26.3	25.9	26.4	26.5	26.0	269.0	4.9	5.1
	HV	266	268	276	266	264	274			
391µm	d	24.0	23.6	23.7	24.4	23.7	24.9	320.8	13.3	14.0
	HV	322	333	330	311	330	299			

Table B74 Hardness near surface and in centre after rolling and aging for 1 hour at T=600°C for AuPtPdRh 54/27.5/17 with a plate thickness D=0,824 mm.

Position		Measurements						m	s	R
40µm	d	24.4	24.6	23.8	24.3	24.5	24.5	312.7	7.5	7.9
	HV	311	306	327	314	309	309			
412µm	d	23.3	23.8	23.0	22.6	23.0	23.2	346.5	12.0	12.6
	HV	342	327	351	363	351	345			

Table B75 Hardness near surface and in centre after rolling and aging for 1.5 hours at T=600°C for AuPtPdRh 54/27.5/17 with a plate thickness D=0,791 mm.

Position		Measurements						m	s	R
40µm	d	24.2	24.5	24.3	23.6	24.5	24.7	314.3	10.2	10.7
	HV	317	309	314	333	309	304			
396µm	d	22.1	22.6	21.8	22.2	21.9	22.6	379.8	9.6	10.1
	HV	380	383	390	376	387	363			

Table B76 Hardness near surface and in centre after rolling and aging for 2 hours at T=600°C for AuPtPdRh 54/27.5/17 with a plate thickness D=0,815 mm.

Position		Measurements						m	s	R
40µm	d	23.7	24.0	23.7	24.4	24.3	24.1	321.0	7.9	8.3
	HV	330	322	330	311	314	319			
407µm	d	23.0	21.9	21.9	21.7	22.3	21.9	379.8	15.7	16.5
	HV	351	387	387	394	373	387			

Table B77 Hardness near surface and in centre after rolling and aging for 2.583 hours at T=600°C for AuPtPdRh 54/27.5/17 with a plate thickness D=0,792 mm.

Position		Measurements						m	s	R
40µm	d	24.3	24.5	23.9	24.8	23.8	24.2	315.7	9.5	10.0
	HV	314	309	325	302	327	317			
396µm	d	23.1	22.1	22.5	23.0	22.8	22.7	360.3	11.6	12.2
	HV	348	380	366	351	357	360			

Table B78 Hardness near surface and in centre after rolling and aging for 3 hours at T=600°C for AuPtPdRh 54/27.5/17 with a plate thickness D=0,793 mm.

Position		Measurements						m	s	R
40µm	d	25.4	25.0	24.4	24.0	25.0	24.3	304.7	13.1	13.7
	HV	287	297	311	322	297	314			
397µm	d	22.8	22.9	22.6	22.2	22.1	22.4	366.7	10.4	10.9
	HV	357	354	363	376	380	370			

Table B79 Hardness near surface and in centre after rolling and aging for 4 hours at T=600°C for AuPtPdRh 54/27.5/17 with a plate thickness D=0,800 mm.

Position		Measurements						m	s	R
40µm	d	25.5	24.5	25.6	24.8	25.5	25.1	293.0	10.6	11.1
	HV	285	309	283	302	285	294			
400µm	d	23.0	23.5	22.4	23.2	23.0	23.3	349.2	11.7	12.3
	HV	351	336	370	345	351	342			

Table B80 Hardness near surface and in centre after rolling and aging for 10 minutes at T=700°C for AuPtPdRh 54/27.5/17 with a plate thickness D=0,800 mm.

Position		Measurements						m	s	R
40µm	d	25.5	24.4	25.2	25.3	24.9	24.7	296.8	9.7	10.2
	HV	285	311	292	290	299	304			
400µm	d	25.0	24.2	24.1	23.7	24.1	23.8	318.2	11.6	12.2
	HV	297	317	319	330	319	327			

Table B81 Hardness near surface and in centre after rolling and aging for 30 minutes at T=700°C for AuPtPdRh 54/27.5/17 with a plate thickness D=0,782 mm.

Position		Measurements						m	s	R
40µm	d	26.4	26.0	26.0	26.7	26.0	26.0	270.3	6.0	6.3
	HV	266	274	274	260	274	274			
391µm	d	25.3	24.3	24.2	23.5	23.9	23.9	317.8	15.6	16.4
	HV	290	314	317	336	325	325			

Table B82 Hardness near surface and in centre after rolling and aging for 45 minutes at T=700°C for AuPtPdRh 54/27.5/17 with a plate thickness D=0,872 mm.

Position		Measurements						m	s	R
40µm	d	25.9	26.7	26.7	26.6	26.0	27.7	262.3	12.2	12.8
	HV	276	260	260	262	274	242			
436µm	d	26.6	25.0	24.8	24.3	25.0	24.8	295.7	17.6	18.5
	HV	262	297	302	314	297	302			

Table B83 Hardness near surface and in centre after rolling and aging for 1 hour at T=700°C for AuPtPdRh 54/27.5/17 with a plate thickness D=0,800 mm.

Position		Measurements						m	s	R
40µm	d	25.5	25.4	26.0	26.1	26.1	26.8	274.7	10.5	11.0
	HV	285	287	274	272	272	258			
400µm	d	23.5	23.4	23.7	23.4	23.3	22.9	340.0	8.0	8.4
	HV	336	339	330	339	342	354			

Table B84 Hardness near surface and in centre after rolling and aging for 1.5 hours at T=700°C for AuPtPdRh 54/27.5/17 with a plate thickness D=0,800 mm.

Position		Measurements						m	s	R
40µm	d	27.1	28.0	28.4	28.7	28.3	27.7	236.5	10.0	10.5
	HV	253	237	230	225	232	242			
400µm	d	25.3	25.4	24.9	25.9	25.3	25.1	289.3	7.7	8.1
	HV	290	287	299	276	290	294			

Table B85 Hardness near surface and in centre after rolling and aging for 2 hours at T=700°C for AuPtPdRh 54/27.5/17 with a plate thickness D=0,800 mm.

Position		Measurements						m	s	R
40µm	d	26.6	27.1	28.2	27.8	26.7	28.2	246.8	13.2	13.9
	HV	262	253	233	240	260	233			
400µm	d	25.3	24.6	24.8	25.0	25.6	25.2	295.0	8.4	8.8
	HV	290	306	302	297	283	292			

Table B86 Hardness near surface and in centre after rolling and aging for 2.5 hours at T=700°C for AuPtPdRh 54/27.5/17 with a plate thickness D=0,774 mm.

Position		Measurements						m	s	R
40µm	d	29.3	29.5	29.7	29.3	29.6	30.0	212.2	3.8	4.0
	HV	216	213	210	216	212	206			
387µm	d	27.3	26.4	27.5	26.9	27.0	27.5	252.5	8.0	8.4
	HV	249	266	245	256	254	245			

Table B87 Hardness near surface and in centre after rolling and aging for 3 hours at T=700°C for AuPtPdRh 54/27.5/17 with a plate thickness D=0,816 mm.

Position		Measurements						m	s	R
40µm	d	31.8	29.3	29.4	29.2	33.7	30.8	198.2	22.1	23.2
	HV	183	216	215	217	163	195			
408µm	d	28.0	28.3	28.2	26.6	26.7	27.2	245.8	13.6	14.3
	HV	237	232	233	262	260	251			

AuPtRh 59/40

The hardness measurements after rolling and ageing at various temperatures are given in: Table B88 for ageing at 500°C, Table B89 at 600°C and Table B90 at 700°C.

Table B88 Hardness in the centre after rolling and aging for various times at T=500°C for AuPtRh 59/40.

Time		Measurements						m	s	R
1h	d	27.5	27.5	27.4	27.6	27.6	29.0	240.7	9.8	10.3
	HV	245	245	247	243	243	221			
2h	d	26.4	25.8	25.9	26.0	26.3	25.9	273.2	5.1	5.4
	HV	266	279	276	274	268	276			
3h	d	24.2	24.6	24.2	24.5	24.0	24.2	314.7	6.0	6.3
	HV	317	306	317	309	322	317			
3.5h	d	24.7	24.0	24.1	24.7	24.8	24.5	310.0	8.5	8.9
	HV	304	322	319	304	302	309			
4h	d	23.7	24.1	23.6	23.7	23.9	23.7	327.8	5.0	5.2
	HV	330	319	333	330	325	330			
5h	d	24.2	23.6	24.0	24.6	23.8	24.2	320.3	9.3	9.8
	HV	317	333	322	306	327	317			
6h	d	23.9	24.4	24.5	23.6	24.2	24.2	318.7	9.0	9.4
	HV	325	311	309	333	317	317			
7h	d	23.7	23.4	23.2	23.2	23.0	22.9	344.0	8.6	9.0
	HV	330	339	345	345	351	354			

Table B89 Hardness in the centre after rolling and aging for various times at T=600°C for AuPtRh 59/40.

Times		Measurements						m	s	R
0.916h	d	24.3	24.0	24.0	24.9	25.4	25.3	305.7	15.8	16.6
	HV	314	322	322	299	287	290			
1h	d	25.2	25.4	25.1	25.3	25.4	25.5	289.2	3.4	3.6
	HV	292	287	294	290	287	285			
1.5h	d	26.6	26.5	26.4	26.0	26.0	26.0	269.0	5.6	5.9
	HV	262	264	266	274	274	274			
2h	d	26.7	26.3	25.3	25.7	26.8	27.9	265.8	18.4	19.3
	HV	260	268	290	281	258	238			
2.5h	d	27.9	26.5	27.4	26.5	27.5	27.0	252.0	10.6	11.1
	HV	238	264	247	264	245	254			
3h	d	28.8	26.8	28.0	27.6	28.5	27.7	238.7	12.1	12.7
	HV	224	258	237	243	228	242			
3.5h	d	28.7	29.1	29.0	29.1	28.5	28.7	222.8	3.7	3.9
	HV	225	219	221	219	228	225			

Table B90 Hardness in the centre after rolling and aging for various times at T=700°C for AuPtRh 59/40.

Time		Measurements						m	s	R
20'	d	29.0	29.5	29.8	29.4	30.3	28.8	214.0	8.0	8.4
	HV	221	213	209	215	202	224			
40'	d	31.0	29.6	30.4	30.5	30.6	30.2	201.0	6.4	6.7
	HV	193	212	201	199	198	203			
1h	d	30.8	31.4	31.0	31.1	31.2	31.1	191.7	2.4	2.5
	HV	195	188	193	192	190	192			
1.5h	d	33.0	32.8	32.5	32.6	32.8	32.9	172.5	2.2	2.3
	HV	170	172	176	174	172	171			
2h	d	33.0	33.0	32.4	32.5	32.6	32.4	174.0	3.3	3.5
	HV	170	170	177	176	174	177			
3h	d	30.5	31.4	30.9	31.1	31.7	30.8	192.2	5.0	5.2
	HV	199	188	194	192	185	195			

AuPtPdRh 44.5/37/17

The hardness measurements after rolling and ageing at various temperatures are given in: Table B91 for ageing at 500°C, Table B92 at 600°C and Table B93 at 700°C.

Table B91 Hardness in the centre after rolling and aging for various times at T=500°C for AuPtPdRh 44.5/37/17.

Time		Measurements						m	s	R
1h	d	26.0	27.5	26.5	27.0	27.1	27.1	257.2	10.2	10.7
	HV	274	245	264	254	253	253			
2h	d	26.4	26.5	26.0	26.4	26.1	25.7	270.5	6.4	6.7
	HV	266	264	274	266	272	281			
3h	d	25.3	25.2	25.5	24.8	25.0	25.3	292.7	6.0	6.3
	HV	290	292	285	302	297	290			
3.5h	d	24.4	24.1	24.8	24.7	25.0	25.3	303.8	10.2	10.7
	HV	311	319	302	304	297	290			
4h	d	24.3	24.9	24.8	24.4	24.4	24.5	307.7	5.9	6.2
	HV	314	299	302	311	311	309			
5h	d	23.6	23.9	24.0	24.0	23.8	24.2	324.3	5.4	5.7
	HV	333	325	322	322	327	317			
6h	d	24.3	24.6	24.4	24.3	24.2	24.6	311.3	4.5	4.7
	HV	314	306	311	314	317	306			
7h	d	23.7	24.5	24.1	23.9	24.3	24.0	319.8	7.6	8.0
	HV	330	309	319	325	314	322			

Table B92 Hardness in the centre after rolling and aging for various times at T=600°C for AuPtPdRh 44.5/37/17.

Times		Measurements						m	s	R
0.916h	d	22.7	22.5	23.4	23.6	23.9	24.3	339.5	20.1	21.1
	HV	360	366	339	333	325	314			
1h	d	23.6	22.9	23.1	23.1	23.3	24.0	341.2	11.8	12.4
	HV	333	354	348	348	342	322			
1.5h	d	22.4	22.4	22.9	23.1	23.1	22.9	357.3	10.2	10.7
	HV	370	370	354	348	348	354			
2h	d	22.7	23.6	23.0	23.5	23.0	23.7	343.5	12.1	12.7
	HV	360	333	351	336	351	330			
2.5h	d	22.9	23.2	22.5	23.3	23.0	22.4	354.7	11.2	11.8
	HV	354	345	366	342	351	370			
3h	d	23.2	23.5	23.1	23.1	23.5	23.3	342.5	5.5	5.8
	HV	345	336	348	348	336	342			
3.5h	d	23.5	24.1	23.9	23.5	23.0	23.0	336.3	13.1	13.7
	HV	336	319	325	336	351	351			

Table B93 Hardness in the centre after rolling and aging for various times at T=700°C for AuPtPdRh 44.5/37/17.

Time		Measurements						m	s	R
20'	d	24.3	24.9	25.0	24.5	24.6	24.0	307.8	9.4	9.9
	HV	314	299	297	309	306	322			
40'	d	26.3	26.5	25.0	26.5	27.8	26.5	266.2	18.2	19.1
	HV	268	264	297	264	240	264			
1h	d	26.6	27.8	27.9	27.0	26.6	27.0	251.7	10.5	11.0
	HV	262	240	238	254	262	254			
1.5h	d	26.4	27.1	26.3	26.9	26.0	27.1	261.7	8.9	9.3
	HV	266	253	268	256	274	253			
2h	d	28.7	28.6	30.3	28.4	29.0	28.0	223.7	11.9	12.5
	HV	225	227	202	230	221	237			
3h	d	28.9	26.5	26.5	25.6	26.0	25.8	264.3	22.1	23.2
	HV	222	264	264	283	274	279			

Homogenisation

The AuPtRh 69/30 and AuPtPdRh 54/27.5/17 alloys were heat treated at various temperatures and various times. The measured hardness profiles for AuPtRh 69/30 are given in Tables B94-B98 and those for AuPtPdRh 54/27.5/17 are given in Tables B99-B104.

Table B94 Hardness profile after rolling and 1 hour temperature treatment at T=1150°C for AuPtRh 69/30 with a plate thickness D=0,836 mm.

Position		Measurements											m	s	R
40µm	d	44.0	41.4	40.0	40.0	40.0	40.0	40.0	40.8	40.0	37.1	39.1	115.2	9.4	6.3
	HV	95.8	108	116	116	116	116	116	111	116	135	121			
418µm	d	35.7	36.4	36.8	34.9	36.2	35.1	35.4	35.1	34.8	34.7	35.6	147.3	5.6	3.8
	HV	146	140	137	152	142	151	148	151	153	154	146			

Table B95 Hardness profile after rolling and 90 hour temperature treatment at T=1150°C for AuPtRh 69/30 with a plate thickness D=0,938 mm.

Position		Measurements											m	s	R
40µm	d	40.6	39.3	38.5	38.0	38.6	38.9	37.8	38.0	38.2	37.7	38.5	124.7	5.2	3.5
	HV	112	120	125	128	124	123	130	128	127	130	125			
160µm	d	36.6	36.6	36.5	35.7	35.8	36.1	36.8	36.1	38.0	36.0	35.7	140.4	5.2	3.5
	HV	138	138	139	146	145	142	137	142	128	143	146			
300µm	d	35.3	35.5	35.7	36.1	35.4	36.3	35.2	35.5	34.8	34.9	34.5	148.3	4.5	3.0
	HV	149	147	146	142	148	141	150	147	153	152	156			
469µm	d	36.1	35.8	35.5	35.8	35.9	36.1	35.9	35.3	35.4	36.1	35.7	144.9	2.4	1.6
	HV	142	145	147	145	144	142	144	149	148	142	146			

Table B96 Hardness profile after rolling and 1 hour temperature treatment at T=1200°C for AuPtRh 69/30 with a plate thickness D=0,857 mm.

Position		Measurements											m	s	R
60µm	d	35.8	35.9	34.9	36.1	35.2	35.7	36.0	35.5	35.3	35.4	41.0	143.3	11.4	7.7
	HV	145	144	152	142	150	146	143	147	149	148	110			
180µm	d	34.8	34.7	35.2	34.8	35.1	35.8	34.4	34.3	34.3	35.5	34.8	152.6	4.2	2.8
	HV	153	154	150	153	151	145	157	158	158	147	153			
300µm	d	33.7	33.7	33.6	32.3	33.4	33.2	33.6	33.8	32.8	33.7	33.6	166.1	4.9	3.3
	HV	163	163	164	178	166	168	164	162	172	163	164			
429µm	d	32.9	32.8	32.4	34.4	32.5	32.4	32.6	32.5	32.0	32.0	33.3	173.5	6.9	4.6
	HV	171	172	177	157	176	177	174	176	181	181	167			

Table B97 Hardness profile after rolling and 1 hour temperature treatment at T=1250°C for AuPtRh 69/30 with a plate thickness D=0,820 mm.

Position		Measurements											m	s	R
40µm	d	37.8	38.8	37.2	35.5	36.2	33.6	34.7	32.0	32.0	33.0	33.6	153.6	20.1	13.5
	HV	130	123	134	147	142	164	154	181	181	170	164			
160µm	d	36.9	34.6	35.0	34.2	31.9	33.9	33.7	36.3	33.0	29.8	30.6	165.9	22.6	15.2
	HV	136	155	151	159	182	161	163	141	170	209	198			
280µm	d	31.9	29.4	29.4	29.4	32.8	31.0	29.4	29.9	30.0	30.5	30.9	201.2	14.7	9.9
	HV	182	215	215	215	172	193	215	207	206	199	194			
410µm	d	30.3	31.2	29.9	29.0	29.2	30.2	29.7	30.2	29.8	30.8	31.4	204.1	10.3	6.9
	HV	202	190	207	221	217	203	210	203	209	195	188			

Table B98 Surface hardness after rolling and 1 hour temperature treatment at T=1300°C for AuPtRh 69/30.

Position		Measurements											m	s	R
surface	d	34.5	38.1	38.6	36.8	35.8	35.1	42.1	33.1	39.6	39.5	33.5	137.9	20.9	14.0
	HV	156	128	124	137	145	151	105	169	118	119	165			

Table B99 Hardness profile after rolling and 1 hour temperature treatment at T=1150°C for AuPtPdRh 54/27.5/17 with a plate thickness D=0,7885 mm.

Position		Measurements											m	s	R
40µm	d	34.6	35.7	32.2	32.3	31.4	33.3	33.3	33.5	34.3	33.3	31.6	168.7	13.1	8.8
	HV	155	146	179	178	188	167	167	165	158	167	186			
394µm	d	33.3	31.8	30.8	32.4	30.4	30.8	30.7	31.4	31.7	31.5	31.6	187.4	9.7	6.5
	HV	167	183	195	177	201	195	197	188	185	187	186			

Table B100 Hardness profile after rolling and 90 hour temperature treatment at T=1150°C for AuPtPdRh 54/27.5/17 with a plate thickness D=0,7795 mm.

Position		Measurements											m	s	R
40µm	d	36.8	35.4	40.0	35.1	34.7	34.3	33.8	34.2	34.8	33.9	34.5	150.5	13.4	9.0
	HV	137	148	116	151	154	158	162	159	153	161	156			
160µm	d	33.0	34.9	33.7	32.6	34.2	33.0	33.7	32.8	32.9	34.3	33.4	165.3	6.9	4.6
	HV	170	152	163	174	159	170	163	172	171	158	166			
280µm	d	32.6	34.5	33.0	33.0	32.5	32.8	35.0	33.8	34.5	34.9	34.1	163.5	9.2	6.2
	HV	174	156	170	170	176	172	151	162	156	152	159			
389µm	d	34.8	34.8	34.0	34.3	33.4	32.7	33.6	33.7	33.3	34.3	33.0	162.3	6.5	4.4
	HV	153	153	160	158	166	173	164	163	167	158	170			

Table B101 Hardness profile after rolling and 1 hour temperature treatment at T=1200°C for AuPtPdRh 54/27.5/17 with a plate thickness D=0,782 mm.

Position		Measurements											m	s	R
40µm	d	31.4	31.0	30.4	30.3	33.6	30.9	33.0	30.6	32.0	30.0	29.5	191.8	15.0	10.1
	HV	188	193	201	202	164	194	170	198	181	206	213			
160µm	d	28.7	30.1	29.5	29.7	30.1	29.8	29.3	29.9	30.1	29.0	29.4	211.9	6.8	4.6
	HV	225	205	213	210	205	209	216	207	205	221	215			
280µm	d	30.0	29.3	29.8	30.0	29.7	28.7	30.4	29.2	30.3	32.1	28.9	208.5	12.3	8.3
	HV	206	216	209	206	210	225	201	217	202	180	222			
391µm	d	29.0	29.5	28.4	29.6	30.6	27.4	28.4	28.7	30.6	30.1	29.3	217.7	14.9	10.0
	HV	221	213	230	212	198	247	230	225	198	205	216			

Table B102 Hardness profile after rolling and 1 hour temperature treatment at T=1250°C for AuPtPdRh 54/27.5/17 with a plate thickness D=0,7585 mm.

Position		Measurements											m	s	R
40µm	d	25.3	26.0	26.7	25.4	25.0	25.0	26.2	25.5	25.9	25.6	25.6	282.0	11.3	7.6
	HV	290	274	260	287	297	297	270	285	276	283	283			
160µm	d	24.8	24.1	24.5	24.6	24.9	25.5	24.9	24.6	23.4	25.3	24.1	306.6	15.0	10.1
	HV	302	319	309	306	299	285	299	306	339	290	319			
280µm	d	24.4	24.4	24.7	24.5	24.7	23.9	24.4	24.4	24.0	23.9	24.2	313.6	7.6	5.1
	HV	311	311	304	309	304	325	311	311	322	325	317			
380µm	d	24.6	23.9	23.9	24.8	24.9	23.4	25.1	24.3	26.4	24.2	23.8	310.4	20.1	13.5
	HV	306	325	325	302	299	339	294	314	266	317	327			

Table B103 Hardness profile after rolling and 1 hour temperature treatment at T=1300°C for AuPtPdRh 54/27.5/17 with a plate thickness D=0,8125 mm.

Position		Measurements											m	s	R
40µm	d	23.3	22.3	22.4	22.9	21.9	22.7	22.3	23.4	21.9	22.4	22.0	367.1	16.7	11.2
	HV	342	373	370	354	387	360	373	339	387	370	383			
160µm	d	21.1	20.4	23.9	20.9	21.1	20.8	21.3	21.0	21.0	21.3	21.0	412.5	30.7	20.6
	HV	417	446	325	425	417	429	409	420	420	409	420			
280µm	d	20.8	20.3	21.2	21.6	21.1	21.5	21.6	21.3	22.0	20.4	21.0	414.7	20.8	14.0
	HV	429	450	413	397	417	401	397	409	383	446	420			
400µm	d	20.7	20.7	20.8	20.8	20.6	20.9	21.4	21.4	22.1	20.9	21.0	420.1	17.0	11.4
	HV	433	433	429	429	437	425	405	405	380	425	420			

Table B104 Hardness in the centre after rolling and 1 hour temperature treatment at T=1300°C for AuPtPdRh 54/27.5/17 with a F=4,903 N = 500 grams.

Position		Measurements								m	s	R
center	d	50.0	49.8	48.6	47.4	47.4	48.4	49	48.4	392.8	15.6	13.0
	HV	371	374	393	413	413	396	386	396			

After these measurements a complete homogeneous specimen was not yet obtained. DTA-determinations of all four alloys were conducted with a high temperature DSC in the 1100-1350°C range. The results of this (see chapter 3) indicated that the 69/30 alloy was not homogenisable and the 54/27.5/17 alloy was. There were some doubts whether the 59/40 alloy could be homogenised, if it could be done it would be at about 1270°C. The 44.5/37/17 was likely to be homogenisable but in any case the temperature had to be above 1350°C. The specimens were heat treated: the 54/27.5/17 and 59/40 at 1270°C and measurement are given in Table B105-B107 and the 54/27.5/17 also at 1350°C in Table B108 and the 44.5/37/17 at 1400°C in Table B109.

Table B105 Hardness profile after rolling and 2 hour temperature treatment at T=1270°C for AuPtRh 59/40 with a plate thickness D=0,589 mm.

Position		Measurements						m	s	R
40µm	d	24.4	23.4	24.4	24.2	24.6	24.7	314.7	12.8	13.4
	HV	311	339	311	317	306	304			
120µm	d	23.9	23.3	22.7	23.7	23.8	23.9	334.8	13.9	14.6
	HV	325	342	360	330	327	325			
200µm	d	23.8	23.6	23.6	23.8	25.1	23.6	324.5	15.2	16.0
	HV	327	333	333	327	294	333			
295µm	d	24.5	23.4	23.9	24.5	22.4	24.3	327.7	23.7	24.9
	HV	309	339	325	309	370	314			

Table B106 Hardness profile after rolling and 2 hour temperature treatment at T=1270°C for AuPtPdRh 54/27.5/17 with a plate thickness D=0,800 mm.

Position		Measurements						m	s	R
40µm	d	25.4	24.6	25.2	25.5	25.2	24.9	293.5	7.8	8.2
	HV	287	306	292	285	292	299			
160µm	d	23.9	24.7	24.0	24.2	24.1	25.0	314.0	11.0	11.5
	HV	325	304	322	317	319	297			
280µm	d	24.8	24.0	24.2	24.4	24.2	24.1	314.7	7.2	7.6
	HV	302	322	317	311	317	319			
400µm	d	24.5	23.3	23.4	23.8	23.9	23.7	328.7	11.7	12.3
	HV	309	342	339	327	325	330			

Table B107 Hardness in the centre after rolling and 4 hour temperature treatment at T=1270°C for AuPtRh 59/40 and AuPtPdRh 54/27.5/17 with a F=4,903 N = 500 grams.

Position		Measurements						m	s	R
60 / 30	d	60.0	60.0	60.0	61.0	60.0	60.0	256.5	3.7	3.9
	HV	258	258	258	249	258	258			
60 / 40	d	57.0	55.5	56.5	57.0	58.0	58.5	284.7	10.6	11.1
	HV	285	301	290	285	276	271			

Table B108 Hardness in the centre after rolling and 1 hour temperature treatment at T=1350°C for AuPtPdRh 54/27.5/17 with a plate thickness D=0,850 mm.

Position		Measurements						m	s	R
center	d	21.2	23.0	23.2	22.0	22.4	22.3	372.5	24.4	25.6
	HV	413	351	345	383	370	373			

Table B109 Hardness in the centre after rolling and 1 hour temperature treatment at T=1400°C for AuPtPdRh 44.5/37/17 with plate thickness D and remarks: the first contained large holes after etching, the second contained crack-like patterns after etching and the last had a second heat treatment of 1 hour at 1425°C.

Alloy		Measurements						m	s	R	D	Remark
50 / 40	d	22.0	21.5	22.2	21.7	21.2	21.9	392.3	13.3	14.0	0.676mm	"Holes"
	HV	383	401	376	394	413	387					
50 / 40	d	20.0	20.0	20.0	20.0	22.0	21.0	443.2	34.3	36.0	0.568mm	"Cracks"
	HV	464	464	464	464	383	420					
50 / 40	d	21.5	20.8	21.0	20.0	21.0	23.0	414.2	37.2	39.0	0.618mm	
	HV	401	429	420	464	420	351					
50 / 40	d	22.4	22.0	22.0	21.9	23.0	22.1	375.7	13.4	14.1	0.554mm	1425°C / 1h
	HV	370	383	383	387	351	380					

Ageing after homogenisation

AuPtPdRh 54/27.5/17

The hardness measurements after rolling, homogenisation and ageing at various temperatures are given in: Table B110 for ageing at 500°C, Table B111 at 600°C and Table B112 at 700°C.

Table B110 Hardness in the centre after rolling, homogenisation and aging for various times at T=500°C for AuPtPdRh 54/27.5/17.

Time		Measurements						m	s	R
1h	d	22.8	22.9	22.8	22.5	22.4	23.0	359.2	7.3	8.4
	HV	357	354	357	366	370	351			
2h	d	21.5	21.0	21.6	21.3	21.0	20.9	412.0	11.4	13.1
	HV	401	420	397	409	420	425			
3h	d	21.1	20.6	21.2	20.5	20.8	20.5	429.7	12.2	14.1
	HV	417	437	413	441	429	441			
4h	d	20.0	20.1	20.2	20.0	20.9	21.0	442.8	30.3	34.8
	HV	464	459	454	464	429	387			
8h	d	20.3	20.7	20.3	20.3	20.5	20.0	448.0	10.4	10.9
	HV	450	433	450	450	441	464			
16h	d	19.8	20.0	20.0	20.1	20.0	20.6	460.2	12.2	12.8
	HV	473	464	464	459	464	437			
23h	d	20.5	20.4	20.0	21.0	20.3	20.0	447.5	16.4	18.9
	HV	441	446	464	420	450	464			

Table B111 Hardness in the centre after rolling, homogenisation and aging for various times at T=600°C for AuPtPdRh 54/27.5/17.

Time		Measurements						m	s	R
1h	d	20.0	20.0	20.9	20.0	20.6	23.0	434.2	44.0	46.2
	HV	464	464	425	464	437	351			
2h	d	20.0	20.9	20.0	20.0	20.0	20.2	455.8	15.6	16.4
	HV	464	425	464	464	464	454			
3h	d	20.3	20.6	21.0	21.0	22.0	21.5	418.5	24.1	25.3
	HV	450	437	420	420	383	401			
4h	d	20.0	20.0	20.0	20.0	19.7	20.9	459.8	18.0	18.9
	HV	464	464	464	464	478	425			

Table B112 Hardness in the centre after rolling, homogenisation and aging for various times at T=700°C for AuPtPdRh 54/27.5/17.

Time		Measurements						m	s	R
15'	d	21.1	21.0	20.3	20.7	21.5	20.5	427.0	17.8	18.7
	HV	417	420	450	433	401	441			
30'	d	21.0	20.8	21.0	20.9	20.7	20.9	425.3	5.1	5.4
	HV	420	429	420	425	433	425			
45'	d	20.8	21.0	21.0	21.2	21.7	21.2	414.8	11.8	12.4
	HV	429	420	420	413	394	413			
1h	d	21.9	21.9	21.8	21.4	21.8	21.6	392.7	7.1	7.5
	HV	387	387	390	405	390	397			
1.5h	d	21.3	21.7	21.1	22.9	21.0	21.4	399.8	24.3	25.5
	HV	409	394	417	354	420	405			

The hardness measurements after homogenisation are rather high and the effect of ageing is not as large as had been expected. Therefore the question if precipitation was really suppressed after homogenisation needed to be investigated. This was done by quenching in water and cooling in liquid nitrogen (-196°C). The hardness was measured as a function of time at which the specimen was at room temperature and the results are given in Table B113. After homogenisation the specimen was kept at room temperature for 16 days and measured: Table B114. Furthermore one specimen was homogenised, quenched, cooled in liquid nitrogen and the surface hardness of this specimen was measured just before and after the embedding during which the specimen remains for 10 minutes at 150°C. The results are given in Table B115.

Table B113 Hardness at the surface after rolling and homogenisation. After waterquench the alloy was kept in liquid nitrogen (-196°C) for a short period of time. The ageing was investigated at room temperature for AuPtPdRh 54/27.5/17.

	Measurements										m	s	R
t(s)	0	105	150	200	260	305	370	420	480	520			
d	24.0	23.0	25.3	24.0	25.5	24.0	23.8	24.0	23.0	23.3			
HV	322	350	290	322	285	322	327	322	350	342			
t(m)		20	37	45	46	47.5	52	53	54				
d		24.0	25.2	21.5	23.5	21.8	24.0	22.5	22.0		335.8	33.1	15.6
HV		322	292	401	336	390	322	366	383				

Table B114 Hardness at the surface after rolling and homogenisation. The AuPtPdRh 54/27.5/17 was kept at room temperature for 16 days.

	Measurements										m	s	R
d	26.0	22.6	24.4	24.0	22.6	23.2	22.9	23.3	24.3	23.2	23.4	333.8	26.6	17.9
HV	274	363	311	322	363	345	354	342	314	345	339			

Table B115 Hardness at the surface after rolling and homogenisation. The AuPtPdRh 54/27.5/17 was kept at -196°C in liquid nitrogen for the short period between waterquench and the measurements just before and after embedding (10 minutes at T=150°C).

embedding		Measurements						m	s	R
before	d	24.5	24.5	23.3	24.0	24.7	21.5	331.2	36.9	38.7
	HV	309	309	342	322	304	401			
after	d	22.2	21.9	21.6	22.1	21.9	21.9	385.7	7.2	7.6
	HV	376	387	397	380	387	387			

AuPtPdRh 44.5/37/17

The hardness measurements after rolling, homogenisation and ageing at various temperatures are given in: Table B116 for ageing at 500°C, Table B117 at 600°C and Table B118 at 700°C.

Table B116 Hardness in the centre after rolling, homogenisation and aging for various times at T=500°C for AuPtPdRh 44.5/37/17.

Time		Measurements						m	s	R
1h	d	20.0	19.4	19.6	19.5	19.6	19.6	482.3	9.8	11.3
	HV	464	493	483	488	483	483			
2h	d	19.5	19.4	19.4	20.0	20.0	20.0	477.7	15.1	17.3
	HV	488	493	493	464	464	464			
3h	d	19.8	20.0	19.6	20.0	20.0	20.0	468.7	7.9	9.1
	HV	473	464	483	464	464	464			
4h	d	20.0	20.0	20.0	20.6	20.9	19.4	457.8	23.9	27.5
	HV	464	464	464	437	425	493			
8h	d	19.6	19.7	19.7	19.6	19.8	19.2	483.0	10.5	11.0
	HV	483	478	478	483	473	503			
16h	d	19.0	19.2	19.3	19.3	19.5	19.3	499.8	8.5	8.9
	HV	514	503	498	498	488	498			
23h	d	19.1	19.3	19.5	19.6	19.8	19.7	488.0	13.0	15.0
	HV	508	498	488	483	473	478			

Table B117 Hardness in the centre after rolling, homogenisation and aging for various times at T=600°C for AuPtPdRh 44.5/37/17.

Time		Measurements						m	s	R
1h	d	19.3	19.5	19.0	18.9	19.5	19.7	497.5	16.1	16.9
	HV	498	488	514	519	488	478			
2h	d	19.1	18.9	18.8	19.3	19.2	19.1	510.2	10.1	10.6
	HV	508	519	525	498	503	508			
3h	d	20.0	18.9	20.0	20.0	19.3	18.7	489.8	30.1	31.6
	HV	464	519	464	464	498	530			
4h	d	20.0	20.0	20.0	20.0	20.0	20.6	459.5	11.0	11.5
	HV	464	464	464	464	464	437			

Table B118 Hardness in the centre after rolling, homogenisation and aging for various times at T=700°C for AuPtPdRh 44.5/37/17.

Time		Measurements						m	s	R
15'	d	20.0	19.4	19.5	20.9	19.5	19.3	476.0	27.6	29.0
	HV	464	493	488	425	488	498			
30'	d	19.6	20.0	20.0	20.7	20.0	20.0	462.0	16.1	16.9
	HV	483	464	464	433	464	464			
45'	d	20.0	20.7	19.9	20.0	21.1	20.0	451.7	21.3	22.4
	HV	464	433	468	464	417	464			
1h	d	20.7	21.5	20.6	21.3	20.9	20.5	424.3	16.1	16.9
	HV	433	401	437	409	425	441			
1.5h	d	20.7	20.0	19.5	20.6	20.0	20.0	458.3	20.4	21.4
	HV	433	464	488	437	464	464			

Appendix C: Relation between yield stress and Vickers hardness

The relation between yield stress, σ_y, and Vickers hardness, H_V, is given by [26]

$$\sigma_y = \frac{10}{3} H_v (0.1)^n \qquad \text{(C1)}$$

where the yield stress is in MPa and n is the strain hardening coefficient. From Table 9 chapter 4 it can be concluded that after rolling, homogenisation at 1050-1100°C and quenching the strain hardening coefficient $n \approx 0.2$, meaning that $\sigma_y = 2.1\ H_V$, and in the other cases $n \approx 0.12$, meaning that $\sigma_y = 2.5\ H_V$.

The results from chapter 4 and the results of Table 9 (averaged if more data are available), and the ratio $\frac{\sigma_y}{H_V}$ are given in Table C1. The hardness of the 54/27.5/17 alloy in a monophase condition (after AQ+1h 1350°C/H_2O), is corrected for the partial precipitation occurring during embedding by subtracting 50 Hv (see §4.4) from the measured value. As for the results of the tensile tests as gathered in Table 7, no information regarding the strain hardening coefficient and the specimen geometry are available, these values are excluded from Table C1.

From Table C1 it can be concluded that equation (C1) holds satisfactory for results obtained from specimens confirming Figure 11..

Table C1. The relation between yield stress, strain hardening coefficient and Vickers hardness.

Alloy	Structure	σ_y (MPa)	n	H_V	$\frac{\sigma_y}{H_V}$	$\frac{10}{3}(0.1)^n$
54/27.5/17	AQ	392	0.23	187	2.1	2.0
	AQ, 3h 600°C	832	0.12	380	2.2	2.5
	AQ, 1h 1350°C	649	0.12	323	2.0	2.5
	AQ, 1h 1350°C, 4h 600°C	1035	0.13	456	2.3	2.5
44.5/37/17	AQ	470	0.18	201	2.3	2.2
	AQ, 3h 550°C	945	0.12	343	2.8	2.5
	AQ, 1h 1400°C, 2h 600°C	1014		510	2.0	